

STRUCTURAL AND TEXTURAL CHANGES DURING THERMO-MECHANICAL PROCESSING OF BORON-DOPED $\text{Ni}_{76}\text{Al}_{24}$

by

SANDIP GHOSH CHOWDHURY

TH
MME/1915/D
CH696



DEPARTMENT OF MATERIALS AND METALLURGICAL ENGINEERING

INDIAN INSTITUTE OF TECHNOLOGY KANPUR

MAY 1995

STRUCTURAL AND TEXTURAL CHANGES DURING
THERMO-MECHANICAL PROCESSING OF
BORON-DOPED $\text{Ni}_{76}\text{Al}_{24}$

A Thesis Submitted
in Partial fulfilment of the Requirements
for the Degree of
DOCTOR OF PHILOSOPHY

by
SANDIP GHOSH CHOWDHURY

to the
DEPARTMENT OF MATERIALS AND METALLURGICAL
ENGINEERING
INDIAN INSTITUTE OF TECHNOLOGY, KANPUR
MAY, 1995

27 JUN 1996

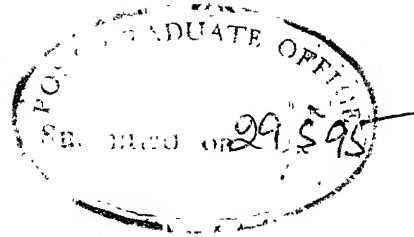
CENTRAL LIBRARY

I. I. T. KANPUR

121704
A.

MME-1995-D-CHO-STR

121704
A121704



CERTIFICATE

It is certified that the work contained in the thesis entitled 'Structural and Textural Changes During Thermo-mechanical Processing of Boron-doped $\text{Ni}_{76}\text{Al}_{24}$ by Sandip Ghosh Chowdhury, has been carried out under our supervision, and that this work has not been submitted elsewhere for a degree.


(Prof. R.K. Ray)


(Prof. A.K. Jena)

Department of Materials and Metallurgical Engineering
Indian Institute of Technology
Kanpur

ACKNOWLEDGEMENTS

The author gratefully acknowledges the immense help and valuable guidance of his supervisors, Professor R.K.Ray and Professor A.K.Jena, throughout the course of present work.

He would also like to express his sincere gratitude to Prof.G.Gottstein, Director, Institut für Allgemeine Metallkunde und Metallphysik, RWTH, Aachen, Germany, for providing a piece of $\text{Ni}_{76}\text{Al}_{24}(\text{B})$ and also for the provision of laboratory facilities for Pole figure and ODF measurements on a number of samples.

Help of various kinds rendered by Mr.B.N.Ghosh and Mr.P.N.Dey of N.M.L. Jamshedpur and by Dr.R.R.Nagarajan, Dr.M.N.Mungole, Mr.Basudeb Bhattacharya, Mr.K.P.Mukherjee, Mr.Vrijendra Kumar, Mr.H.C.Srivastava, Mr.S.C.Barthwal, Mr.Umashankar, Mr.V.K.Jain and Mr.G.S.Thapa is gratefully acknowledged.

He would also like to express his sincere thanks to his friends Santanu Bhattacharya, Tapan Khan, Paritosh Chowdhury and P.K.Giri for their help in the experimental work. Thanks are also due to T.K.Roy, G.G.Roy, N.K.Nath M.Sujata, S.Suwas, K.S.Rao, I.N.Kar, T.Som, J.Mukherjee, Arun Saha, Arna Gupta and Srabani Banerjee for their help on many occasions.

Last, not but the least, the author is sincerely indebted to his parent for their inspiration till date in completing the work.

Sandip Ghosh Chowdhury

CONTENTS

	page
Acknowledgements	iii
List of figures	vii
List of tables	xii
Abstract	xiii
Chapter I : Introduction	1
Chapter II : Literature Review	5
2.1. : Structure of the γ' phase, Ni_3Al	5
2.1.1. Unit Cell	5
2.1.2. Ordering behaviour	5
2.2. : Planer Faults	10
2.3. : Deformation	19
2.3.1. Yield Stress Anomaly	20
2.3.2. Ductility	22
2.3.3. Deformation Texture	27
2.4. : Diffusion	3
2.5. : Recrystallization	3
2.6. : Scope of the Present Investigation	4
Chapter III : Experimental Procedure	4
3.1. : Alloy Preparation	4
3.2. : Cold Rolling	4
3.3. : Annealing	4
3.4. : X-ray Diffraction	4
3.5. : Texture Representation and Determination	4
3.6. : Optical and Scanning Electron Microscopy	4

- 3.7. : Transmission Electron Microscopy
- 3.8. : Microhardness and Resistivity
- 3.9. : Differential Scanning Calorimetry

Chapter IV : Cold Rolling Characteristics

- 4.1. : Microstructure
- 4.2. : Texture
 - 4.2.1. Development of Texture
 - 4.2.2. Texture Transition
- 4.3. : Structural Changes
 - 4.3.1. Order Parameter
 - 4.3.2. Crystal Structure
 - 4.3.3. Strain Parameter
 - 4.3.4. Microhardness and Resistivity
- 4.4. : Correlation of Structure with Textural Transition

Chapter V : Annealing Characteristics

- 5.1. : Recovery
 - 5.1.1. Order Parameter
 - 5.1.2. Strain Parameter
 - 5.1.3. Microhardness
 - 5.1.4. Microstructure
 - 5.1.5. Energetics
 - 5.1.5.1. Analysis of DSC Data
 - 5.1.5.2. Identification of Peaks
 - 5.1.5.3. Kinetics
- 5.2. : Recrystallization
 - 5.2.1. Kinetics
 - 5.2.2. Development of Texture
- 5.3. : Evolution of Texture and Structure during Annealing

Chapter VI : Summary and Conclusion

1

References

1

LIST OF FIGURES

	page
Fig.2.1 : Unit cell of Ni_3Al (L1_2 structure).	6
Fig.2.2 : XRD intensity profiles for (a) (111), (200) and (220) reflections; (b) (100) and (110) reflections [12].	8
Fig.2.3 : Structural relationship between L1_2 and DO_{22} structures [13].	9
Fig.2.4 : Reordering of mechanically disordered Ni_3Al filings on the basis of (100) and (200) reflections [16].	9
Fig.2.5 : XRD pattern of Ni_3Al powders with milling time [17].	11
Fig.2.6 : Variation of LRO parameter as a function of milling time on the basis of (110) and (200) reflections [18].	12
Fig.2.7 : APBs in L1_2 structure: (a) (010) plane; (b) $1/2[\bar{1}01]$ dislocation on (111) plane, producing APB; (c) two $1/2[\bar{1}01]$ dislocations on (111) plane with APB between them.	12
Fig.2.8 : Four types of faults in A_3B alloy with L1_2 structure: large, medium and small circles represent atoms in upper, middle and lower (111) planes, respectively; open circle : A atoms, close circle : B atoms.	14
Fig.2.9 : APB coupled dissociation in Ni_3Al [14].	17
Fig.2.10: SISF coupled dissociation in Ni_3Al [14].	17
Fig.2.11: APB coupled dissociation in $\text{Ni-24at.\%Al-1at.\%B}$ [33].	18
Fig.2.12: Temperature dependence of flow stress of Ni_3Al alloy [11]	21
Fig.2.13: Dynamic breakaway model utilized by cross-slip pinning model [37].	21
Fig.2.14: (a) Effect of boron concentration, (b) effect of aluminium concentration on the ductility of Ni_3Al [2].	24
Fig.2.15: Standard {111} pole figures of (a) Copper and (b) Brass.	28

Fig.2.16: ODF of 90% cold rolled boron-doped Ni_3Al [70].

Fig.2.17: ODF of 92% cold rolled boron-doped Ni_3Al [20].

Fig.2.18: TEM micrograph of the longitudinal section of 70% cold rolled boron-doped Ni_3Al [20].

Fig.2.19: Temperature dependence of D_{Ni}^* in pure Ni_3Al [74].

Fig.2.20: Recrystallization volume fraction vs annealing time for 90% cold rolled Cu_3Au [69].

Fig.2.21: Schematic Arrhenius plot of migration rates for grain boundaries in the ordered and disordered states [69].

Fig.2.22: Long term hardening kinetics at 480°C of different Ni_3Fe alloys [84].

Fig.2.23: Short term hardening kinetics at 525°C in Ni_3Fe [84].

Fig.2.24: Time for 50% recrystallized volume fraction of 50% cold rolled $(\text{Co}_{78}\text{Fe}_{22})_3\text{V}$ annealed above and below T_c [87].

Fig.2.25: Reduction of hardness in Ni_3Al during annealing at various temperatures. '↑' denote starting of recrystallization [19].

Fig.2.26: ODF of boron-doped Ni_3Al after annealing at:
(a) 1 hr at 650°C ; (b) 2 hrs at 700°C [70].

Fig.2.27: ODF of $\text{Ni}_3\text{Al(B)}$ after annealing for 30 min. at 750°C [90].

Fig.3.1 : Three dimensional Euler space showing locations of ideal orientations.

Fig.3.2 : Schematic presentation of the FCC rolling texture in the first subspace of three dimensional Euler angle space [97].

Fig.4.1 : Optical micrograph of homogenized boron-doped $\text{Ni}_{76}\text{Al}_{24}$ alloy

Fig.4.2 : Effect of cold rolling on crack nucleation and propagation in the present alloy.

Fig.4.3 : Optical micrograph of longitudinal section after 25% cold rolling (RD parallel to the markers).

Fig.4.4 : Optical micrographs of longitudinal sections of (a) 45%, (b) 65% and (c) 85% cold rolled $\text{Ni}_{76}\text{Al}_{24}(\text{B})$ alloy (markers parallel to RD).

Fig.4.5 : TEM micrograph showing straight dislocation on the rolling plane section of 45% cold rolled $\text{Ni}_{76}\text{Al}_{24}(\text{B})$ (Markers parallel to RD).

Fig.4.6 : TEM micrographs of the rolling plane sections of (a) 45%, (b) 65% and (c) 85% cold rolled $\text{Ni}_{76}\text{Al}_{24}(\text{B})$ (Markers parallel to RD).

Fig.4.7 : TEM micrograph showing twins in 85% cold rolled boron-doped $\text{Ni}_{76}\text{Al}_{24}$ (Markers parallel to RD).

Fig.4.8 : (111) pole figures of (a) 25%, (b) 45%, (c) 65% and (d) 85% cold rolled $\text{Ni}_{76}\text{Al}_{24}(\text{B})$.

Fig.4.9 : ODFs of (a) 25%, (b) 45%, (c) 65% and (d) 85% cold rolled $\text{Ni}_{76}\text{Al}_{24}(\text{B})$ at constant ϕ_2 sections.

Fig.4.10 : Plot of $f(g)$ vs ϕ_1 along $\phi = 45^\circ$ and $\phi_2 = 0^\circ$ for $\text{Ni}_{76}\text{Al}_{24}(\text{B})$.

Fig.4.11 : Plot of $f(g)$ vs ϕ_2 for $\text{Ni}_{76}\text{Al}_{24}(\text{B})$.

Fig.4.12 : Plot of ϕ_1/ϕ vs ϕ_2 for $\text{Ni}_{76}\text{Al}_{24}(\text{B})$.

Fig.4.13 : Plot of $f(g)$ vs ϕ along $\phi_1 = 90^\circ$ and $\phi_2 = 45^\circ$ for $\text{Ni}_{76}\text{Al}_{24}(\text{B})$.

Fig.4.14 : Plot of $f(g)$ vs ϕ_2 for Ni.

Fig.4.15 : Plot of $f(g)$ vs ϕ_2 for Ni-40Co alloy.

Fig.4.16 : XRD pattern for $\text{Ni}_{76}\text{Al}_{24}(\text{B})$ with various degrees of cold rolling.

Fig.4.17 : XRD line intensities with various degrees of cold rolling
(a) (100) and (200) reflections; and
(b) (110) and (220) reflections.

Fig.4.18 : Variation of order parameter (S) with cold rolling.

Fig.4.19 : Variation of S with cold rolling in Cu_3Au [105].

Fig.4.20 : XRD pattern of powders from 85% cold rolled $\text{Ni}_{76}\text{Al}_{24}(\text{B})$.

Fig.4.21 : (a) SAD pattern of 45% cold rolled $\text{Ni}_{76}\text{Al}_{24}$ (B);

(b) Analysis of the above pattern.

Fig.4.22 : Variation of strain parameter with cold rolling.

Fig.4.23 : Variation of hardness with cold rolling in $\text{Ni}_{76}\text{Al}_{24}$ (B).

Fig.4.24 : Variation of resistivity with cold rolling in $\text{Ni}_{76}\text{Al}_{24}$ (B).

Fig.4.25 : Schematic representation of the course of texture evolution in the present $\text{Ni}_{76}\text{Al}_{24}$ (B).

Fig.5.1 : Effect of isochronal annealing on S of cold rolled samples: (a) (100)/(200); (b)(110)/(220) reflections.

Fig.5.2 : Variation of S with time at 525° and 625°C.

Fig.5.3 : Variation of S with time at 850°C.

Fig.5.4 : XRD line profiles for annealed samples.

Fig.5.5 : Variation of strain parameter with isochronal annealing temperature.

Fig.5.6 : Variation of Strain Parameter with time in the temperature range of 250° - 350°C.

Fig.5.7 : Variation of hardness during isothermal annealing.

Fig.5.8 : Variation of hardness with isochronal annealing temperature.

Fig.5.9 : Short range hardness maxima at 525° and 625°C.

Fig.5.10 : Sub-boundary formation during annealing at 300°C.

Fig.5.11 : Deformed microstructure retained after annealing at 300°C.

Fig.5.12 : Stripe-like features emanating from the grain boundaries.

Fig.5.13 : High density of stripe-like L1_2 domains near the grain boundaries after annealing at 500°C.

Fig.5.14 : Criss-cross arrangements of L1_2 structured domains after annealing at 500°C.

Fig.5.15 : (a) Formation of twins after annealing at 500°C, (b) SAD pattern of that area and (c) its analysis.

- Fig.5.16 : Formation of subgrain from a cold rolled matrix after annealing at 700°C.
- Fig.5.17 : Competitive growth of subgrains after annealing at 700°C.
- Fig.5.18 : Formation of group of subgrains after annealing at 700°C.
- Fig.5.19 : (a) Partly recrystallized area after annealing at 800°C and (b) its SAD pattern and analysis.
- Fig.5.20 : Full recrystallization after annealing at 925°C.
- Fig.5.21 : DSC thermograms of 85% cold rolled $\text{Ni}_{76}\text{Al}_{24}$ (B) alloy.
- Fig.5.22 : Peak A at different heating rates.
- Fig.5.23 : (a) Micrograph at the beginning of the peak A; (b) Micrograph after the peak A.
- Fig.5.24 : Microstructure after heating to 900°C.
- Fig.5.25 : Variation of volume fraction vs T corresponding to peak A.
- Fig.5.26 : Determination of activation energy by integral technique.
- Fig.5.27 : Variation of volume fraction recrystallized with time at various temperatures in $\text{Ni}_{76}\text{Al}_{24}$ (B).
- Fig.5.28 : Johnson-Mehl plot for the determination of n and k.
- Fig.5.29 : Variation of n with temperature.
- Fig.5.30 : Determination of activation energy by constant fraction technique.
- Fig.5.31 : Determination of activation energy by rate constant technique.
- Fig.5.32 : Texture after annealing at 850°C for 17 hr.
- Fig.5.33 : Texture after annealing at 950°C for 1 hr.
- Fig.5.34 : Texture after annealing at 950°C for 48 hrs.
- Fig.5.35 : Texture after annealing at 1025°C for 1 hr.
- Fig.5.36 : Development of texture at 850°C : (a) 1 hr, (b) 5 hrs, (c) 11 hrs and (d) 24 hrs.

LIST OF TABLES

Table 2.1 : Fault energies of $\text{Ni}_3\text{Al(B)}$.

Table 2.2 : Activation energies for diffusion of Ni and Al in Ni_3Al .

Table 2.3 : Comparison of the parameters of the recrystallization kinetics reported in the literature.

Table 4.1 : Peak positions and relative intensities for the 85% cold rolled specimen and powders made from that.

Table 4.2 : Comparison of theoretical relative intensities for L1_2 and disordered FCC structure.

Table 4.3 : Theoretical intensities and the peak positions for DO_{22} structure.

Table 4.4 : Comparison of the experimentally observed intensities with the theoretical intensities of the DO_{22} structure.

Table 5.1 : Characteristics and total heat effects of Peak A at different heating rates.

Table 5.2 : Values of avrami exponent, n , as a function of temperature and volume fraction.

Table 5.3 : Values of activation energies as a function of temperature and volume fraction.

ABSTRACT

The high temperature structural materials which have been commercially exploited for the last few decades are primarily superalloys based on Ni, Co and Fe. As the application temperatures are very close to the melting temperatures of these alloys, a severe limitation is imposed on further development of these materials. Recent research has demonstrated that intermetallics may eventually prove to be better than the superalloys. Ordered intermetallics, especially Ni and Ti based aluminides have been widely hailed as the potential new generation materials for high temperature applications. These intermetallics having long range ordered structures possess many desirable properties like high melting temperature, low density and significant elevated temperature strength. In ordered alloys various atomic species tend to occupy specific sublattice sites and produce superlattice structures. Long range order implies stronger bonding, generally makes diffusion slower and consequently, leads to better creep resistance. Intermetallics, such as aluminides, are highly oxidation and corrosion resistant because of their ability to form continuous adherent surface oxide films. The tendency to form covalent bonds between the constituent atoms of intermetallic compounds leads to high cohesive strength of these materials. Complex crystal structures of aluminides are associated with relatively large burgers vectors resulting in higher peierls stresses and a shortage of operative slip systems. The deformation of ordered intermetallics necessitates the movement of superlattice dislocations associated with antiphase boundaries, the energy of which depends on the plane on which the boundary exists.

The best known example of intermetallic materials is Ni_3Al which is the

main strengthening constituent of Ni-base superalloys. The yield strength of this material increases with increase in temperature upto 600°C. Such variation of strength with temperature differs from that of conventional metals and alloys. However, the major drawback of this intermetallic compound is its low ductility and brittle intergranular fracture behaviour in the polycrystalline state. Trace additions of boron have proved effective in ductilizing this alloy. The substantial room temperature ductility of boron-doped Ni_3Al makes it a material suitable for processing by conventional routes i.e. cold forming by rolling followed by annealing. Such thermomechanical treatments (TMT) produce changes in microstructure and crystallographic texture which ultimately affect the mechanical properties. Very little research has been carried out on these and related aspects. To bridge this gap in the existing literature, the present study has been undertaken to investigate the changes in microstructural and textural characteristics during cold deformation by rolling and subsequent annealing in boron-doped Ni_3Al .

The alloy used in the present study was an off-stoichiometric one having the nominal composition Ni-24Al-0.24B (at.%). The alloy was arc melted and cold forged (30%) followed by homogenization annealing at 1050°C for 25 minutes. The initial grain size was 25-30 μm . Thorough examination of the alloy using optical and scanning electron microscopes (with EDAX facility) showed that the alloy was a single phase material with uniform composition. X-ray diffraction results also confirmed the single phase L1_2 structure with $a = 3.569\text{\AA}$. Homogenized samples of 4.5mm thickness were rolled at room temperature for different degrees of reduction ranging from 25% to 90%. Cold rolling was carried out in a two high laboratory rolling mill having 150mm diameter rolls. After cold rolling the samples were prepared for optical microscopy and transmission electron microscopy (TEM). X-ray diffraction

technique was used to measure the variation of the order parameter (S) with cold work. Two pairs of reflections, $(100)/(200)$ and $(110)/(220)$, were used to estimate the S value. The strain parameter was measured as B_r/B_o , where B_r was the half intensity line breadth of the cold rolled alloy and B_o was that of the initial homogeneous alloy. Microhardness measurements were taken in a Vicker's hardness tester using load of 25 gms. Resistivity of the samples was measured by the four probe method for sheet specimens. Crystallographic texture was determined by plotting pole figures as well as by determining three dimensional orientation distribution functions (ODF).

X-ray diffraction studies showed that local atomic configuration could be changed by cold work. The order parameter (S) calculated from $(100)/(200)$ pair of reflections gradually decreased with increasing cold work and became zero after 65% cold deformation. By contrast, the order parameter measured from the $(110)/(220)$ pair initially decreased upto 65% deformation and then attained a nearly constant value of 0.4 until about 90% deformation. X-ray diffraction studies indicated that the original $L1_2$ structure of $Ni_3Al(B)$ alloy transformed to the DO_{22} structure after 65% cold rolling. The strain parameter dropped suddenly after 45% cold work and then again increased with further cold deformation.

Optical microscopy of the cold rolled samples showed the presence of shear bands in the longitudinal section starting after 65% deformation. The frequency of the shear bands increased with the progress of rolling upto 85%. TEM studies carried out on the rolling plane sections showed a cellular substructure with more or less straight dislocation lines in case of 45% deformed specimen. The selected area diffraction (SAD) pattern showed double spots in several areas in the microstructure. These spots were due to superimposition of DO_{22} structure on the spots of $L1_2$ structure. After 65% deformation, microbands appeared with small orientation changes between

neighbouring bands and the density of dislocations increased considerably. However, the microstructure of the 85% deformed samples showed large scale twinning, numerous microbands and a high density of dislocations.

The hardness values showed unusual softening after 45% cold rolling. The resistivity decreased with cold work upto 45% reduction and then became constant till 85% cold work.

The alloy $\text{Ni}_3\text{Al(B)}$ has an ordered FCC structure having stacking fault energy similar to that of pure nickel. However, the textural evolution during deformation in these two materials were found to be quite different. The texture was quite similar (copper or pure metal type) in the two cases upto 45% cold rolling; however, with increasing rolling reduction, the texture of $\text{Ni}_3\text{Al(B)}$ changed to the alloy or α -brass type while pure nickel retained the copper type texture. The brass (B_s) textural component, which is very stable in the case of highly deformed FCC metals and alloys, appears to be less stable in $\text{Ni}_3\text{Al(B)}$ and changes into the rotated Goss, $\{110\}\langle 110\rangle$, after heavy deformation.

The X-ray diffraction pattern and the splitting of the fundamental spots confirm the transformation of the initial L1_2 structure to DO_{22} . The sudden drop of stain parameter and hardness are also consistent with the transformation. Due to this structural transformation, the deformation mode changes from slipping to twinning. During slip deformation, Ni_3Al having high stacking fault energy develops copper type texture. However, with change in the deformation mode, the copper type texture changes to the α -brass type due to the heavy incidence of twinning.

Annealing treatments were given to 85% cold rolled samples. Isochronal annealing for 1 hour showed that major changes in the order parameter and strain parameter took place within the temperature range of $300^\circ - 500^\circ\text{C}$.

Isothermal annealing was carried out on 85% cold rolled samples in the

temperature range of 250° - 350°C . The decrease in half intensity breadth at the initial stages of annealing indicated recovery. TEM study showed deformation twins in some regions and straight dislocations in other areas. However no reverse transformation to L_{12} structure was detected by SAD or X-ray diffraction.

Isothermal annealing at 500°C showed increase in hardness and increase in order parameter. The transformation to L_{12} at this stage was also detected by TEM. The restoration of the L_{12} structure from the DO_{22} can be divided into two stages - stage I at low temperature (200° - 400°C) where the kinetics is fast and stage II at high temperature (600° - 900°C) where the kinetics is slow.

DSC experiments showed that recrystallization was preceded by structural transformation. The amount of energy associated with that transformation was 11.5 kJ/mol. Since a part of the total stored energy was spent on the transformation, the driving force for recrystallization became less and this led to sluggish recrystallization behaviour.

Isothermal annealing of 85% cold rolled samples between 800° - 950°C at intervals of 25°C showed that the recrystallization phenomena followed the Avrami equation. As recrystallization is a diffusion controlled phenomenon, the rate of recrystallization was found to increase with temperature. The values of 'n' of the Avrami equation decreased with increase in temperature upto 950°C (2.2 to 0.71) when the volume fraction recrystallized was low (60%); however, after 60% transformation, 'n' was constant at all temperatures. The activation energy varied with volume fraction upto 900°C ; above that temperature it became constant and this value is higher (more than twice) than the value at lower temperatures. The activation energy values are comparable with the activation energy for lattice diffusion of Ni in Ni_3Al .

The textural investigation carried out during isothermal annealing at

850°C showed that initially {025}<100> and {102}<201> orientations developed. However, after full recrystallization, the components became {025}<100> and {011}<100>. The last one is a retained rolling texture component. The texture after full recrystallization is very weak with a maximum intensity of about 1.5 times that of random, in comparison to the deformed texture ($f_{\max} = 5.0$). The texture after 48 hours of annealing at 950°C consists of {011}<100>; whereas the components present after 1 hour at 1025°C are {011}<100> and {025}<100>.

On the basis of the present investigation, it can be concluded that the boron-doped $\text{Ni}_{76}\text{Al}_{24}$ alloy undergoes structural transformation from L1_2 to DO_{22} during cold rolling. Due to this transformation, the deformation mode changes from slipping (in L1_2) to twinning (in DO_{22}) and the cold rolling texture shows a transition from the copper-type to the alloy-type. The texture is basically copper-type after low degree of deformation (45%), but it changes to the alloy-type after heavy deformation (85%). The brass (B_s) component of the deformation texture, which is found to be quite stable in deformed FCC metals and alloys, gets converted to the rotated Goss component after heavy deformation in the present alloy. This appears to be characteristic deformation texture component of $\text{Ni}_3\text{Al(B)}$.

The alloy transforms back to the original L1_2 structure during annealing. The annealing process consists of three phenomena : recovery, reverse structural transformation from DO_{22} to L1_2 and recrystallization. As a part of the energy is consumed by structural transformation, driving force for recrystallization becomes less and this leads to sluggish recrystallization kinetics. The structural transformation from DO_{22} to L1_2 appears to involve a multiplicity of variants as well as the formation of a high density of twins in the product phase. This will lead to large scale fragmentation of the grains. As a result, a weak 'transformation' texture is

produced from a sharp deformation texture even during the pre-recrystallization stage. When recrystallization occurs, a high nucleation rate coupled with a substantially low growth rate, ensures that this weak texture is retained even after complete recrystallization. The nearly random recrystallization texture in this alloy will have the effect of making it isotropic in its mechanical behaviour, which may be of considerable advantage during high temperature application.

CHAPTER I

INTRODUCTION

The ever increasing thrust for energy conservation in the recent times has forced engineers to design jet engines with high fuel efficiency. However, structural materials required for advanced jet engines and other high performance aerospace applications must have high temperature capabilities for improved performance. These materials must also have requisite ductility and toughness at both elevated and ambient temperatures. Demand for improved high temperature structural materials is widespread for manufacturing of supersonic airplanes, spacecrafts, missiles, rockets, turbines and various types of reactors. In order to be useful, a potential high temperature material must satisfy certain physical (e.g. density) and chemical criteria (e.g. corrosion resistance), many of which are highly sensitive to processing history and the resultant internal structure.

Alloys based on high melting materials as well as refractory elements with superior creep strength had been considered for high temperature applications. However, these materials had poor oxidation resistance. Several ceramic materials with good environmental stability did have the desired qualities but they failed to satisfy the toughness criteria. Hybrids of ceramics and metals, known as cermets, were also found to be inferior because of their low toughness. Eventually, Ni-base superalloys emerged during the last few decades as the primary material for high temperature applications. The quest for materials that may exceed the performance of superalloys, led to the development of ordered intermetallics, especially Ni and Ti aluminides as potential new generation materials for such applications. These intermetallics, with long range ordered structure, possess many desirable properties like high melting temperature, low density and a significant

elevated temperature strength. These aluminides are also highly oxidation and corrosion resistant because of their ability to form compact and adherent oxide surface films.

Various atomic species in an ordered alloy tend to occupy specific sublattice sites, giving rise to superlattice structures. Long range order produces stronger bonding and generally leads to sluggish diffusion processes as well as better creep resistance. The tendency to have covalent bonding between the component atoms of a compound leads to strong cohesive strength. Complex crystal structures also lead to large burgers vectors, thus resulting in higher peierls stress and a shortage of operative slip systems. That is why most intermetallics are hard to deform plastically. The deformation of ordered intermetallics is usually achieved by the movement of superlattice dislocations which are separated by antiphase boundaries. These faults generally have low energies on certain planes. The anisotropy of fault energies gives rise to complex dislocation movement and leads to high strength and strong work-hardening behaviour at low temperatures and increase in flow stress with increase in temperature. This unique behaviour makes the aluminides strong candidates for high strength and high temperature usage.

The best known example of intermetallics is Ni_3Al (γ') which is the main strengthening constituent of Ni-base superalloys. In contrast to the behaviour of conventional metals and alloys the yield strength of Ni_3Al increases with temperature upto 600°C . The maximum strength of Ni_3Al occurs just above half of its melting temperature which is generally considered to be the maximum usable temperature for single phase materials. This alloy is highly resistant to oxidation by air as a result of its ability to form adherent oxide surface films that protect the base metal from excessive attack.

The major drawback of this intermetallic compound is its low ductility

and brittle intergranular fracture behaviour in the polycrystalline state. Considerable effort has been devoted towards improving the ductility and fabricability of Ni_3Al and aluminides in general, in order to make them commercially viable. The brittle fracture of these materials was reported earlier as due to the intrinsic grain boundary weakness; though recent investigations revealed that an extrinsic factor (such as moisture) could be responsible for this low ductility. Aoki and Izumi [1] first discovered that small amounts of boron addition could substantially improve the ductility of Ni_3Al at room temperature. Liu et al. [2] achieved a tensile elongation exceeding 50% by control of boron concentration, alloy stoichiometry and thermomechanical treatment.

Boron additions have been found to be quite effective in enhancing the cohesion of grain boundaries in Ni_3Al at temperatures below 800°C , but this effect deteriorates at higher temperatures. It has been reported that boron doped Ni_3Al can be ductile at high temperature if the structure was fine [3]. Bend tests on recrystallized Ni_3Al [4], indicated that grain boundary cracking occur preferentially along large angle boundaries. This result implies that ductility improvement may be possible by the control of grain orientations. Thus, an effective scheme for increasing strength and ductility must involve thermomechanical processing. Substantial ductility of boron-doped Ni_3Al makes it suitable for conventional processing routes, usually comprising of cold forming (rolling) followed by annealing. This type of thermomechanical treatment is likely to lead to recrystallization and change the microstructure as well as the crystallographic texture.

Only a limited amount of research has been reported on these aspects. No systematic attempt has yet been made to analyze the microstructure vis-a-vis the textural development in such materials. In order to bridge this gap in the existing knowledge, a Ni-rich boron-doped polycrystalline $\text{Ni}_{76}\text{Al}_{24}$ alloy

was subjected to cold rolling followed by annealing. The changes in the microstructure as well as the textural development as a function of the processing parameters were investigated using a number of characterization techniques including X-ray diffraction, Transmission Electron Microscopy (TEM), Scanning Electron Microscopy (SEM) and Differential Scanning Calorimetry (DSC). The textural evolution was investigated by studying conventional pole figures and the orientation distribution function (ODF) of materials subjected to various thermomechanical processing. The evolution of microstructure during thermomechanical processing and its correlation with texture development was studied in detail in this work.

CHAPTER II

LITERATURE REVIEW

2.1 Structure of the γ' phase, Ni_3Al :

2.1.1 Unit Cell :

The γ' phase, Ni_3Al has the Cu_3Au type structure and its strukturbericht designation is L1_2 . In this structure, nickel atoms occupy the face centered positions and aluminium atoms occupy the corner positions in a cubic array (Fig. 2.1). The structure may be described in terms of four interpenetrating simple cubic sublattices out of which three are occupied by nickel atoms and the remaining one is occupied by aluminium atoms.

2.1.2. Ordering Behaviour :

The compound Ni_3Al forms peritectically at 1395°C in the Ni-Al system [5]. Literature on the ordering behaviour of this compound is quite extensive. Guard and Westbrook [6] reported the presence of diffuse (100) superlattice peak intensity at 1000°C . Based on electrical resistivity measurements, Corey and Lisowsky [7] reported that Ni_3Al having 22.5 at.% aluminium became disordered between 1100° and 1300°C . Later, Stoeckinger and Newmann [8] showed that Ni_3Al having less than 23 at.% Al contained $\gamma + \gamma'$ at 1100°C . They found strong (100) line intensity in both stoichiometric and nickel-rich off-stoichiometric single crystals. They further reported on the basis of (100)/(200) and (300)/(400) intensity ratios that long range order was maintained upto 1320°C . Pope and Garin [9] also reported constant long range order parameter below 1300°C . Masahashi et al. [10] observed that the superlattice reflections of Ni_3Al got intensified due to addition of carbon and boron in stoichiometric and off-stoichiometric compositions.

Noguchi et al. [11] reported that alloy additions changed the relative stability of the structures L1_2 , DO_{19} and DO_{22} of composition Ni_3Al . This is

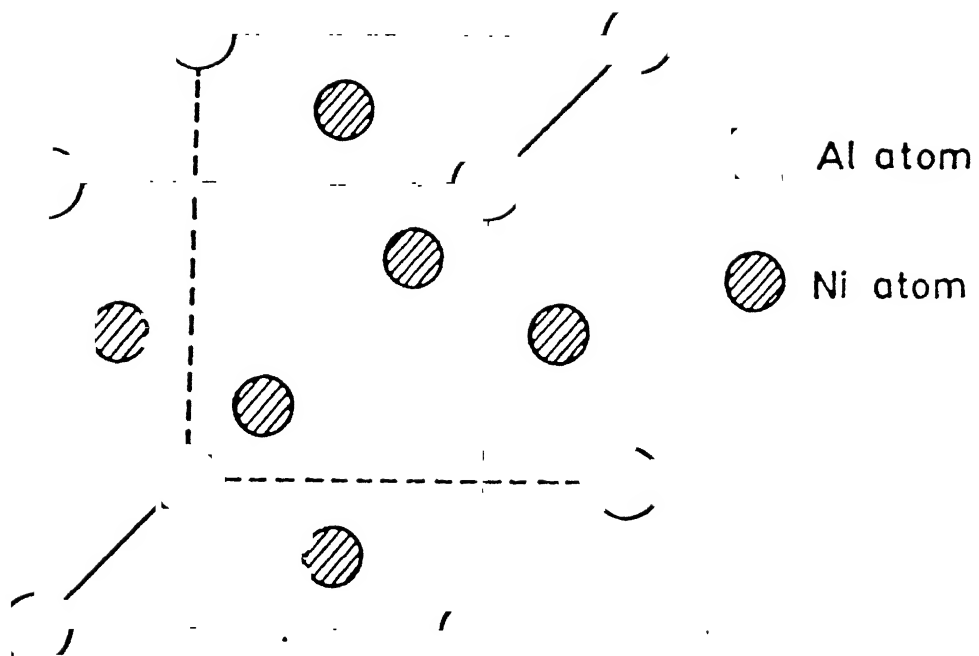


Fig.2.1 : Unit cell of Ni_3Al (L1_2 structure).

said to be because of the creation of the anti-structure defects. The anti-structure defects are created when one particular atom occupies the position of different sublattice. Ramesh et al. [12] measured the long range order parameter, S , on the basis of $(100)/(200)$ and $(110)/(220)$ intensity reflections for stoichiometric as well as nickel-rich off-stoichiometric Ni_3Al with and without boron addition. According to them, the L1_2 structure attains the near theoretical value of S at about 600°C . They found splitting of (100) , (110) , (200) and (220) reflections (Fig.2.2) and concluded that the structure of Ni_3Al at 1000°C could be DO_{22} . Yamaguchi et al. [13] suggested that the DO_{22} structure could be derived from the L1_2 structure by introducing one $1/2[110]$ APB on every (001) planes (Fig.2.3).

Ordered Ni_3Al having L1_2 structure could be made disordered by intense plastic deformation. Horton et al. [14] reported that the separation distance between the superpartials increased and hence lowered the APB energy during in-situ straining experiments carried out in the TEM of an off-stoichiometric Ni_3Al . However, no detailed mechanism is known to account for this phenomenon. Corey and Potter [15] measured the $(100)/(200)$ intensity ratios and Clark and Mohanty [16] measured the $(110)/(220)$ intensity ratios of filed Ni_3Al powders and concluded that Ni_3Al could be substantially disordered by intense plastic deformation due to filing. This conclusion was based on the fact that the intensities of the superlattice line (100) and (110) decreased to very low values in the filed powders. Clark and Mohanty [16] examined the gradual return of order when such filed powders was isothermally annealed at various temperatures (Fig.2.4). Corey and Potter [15] did similar studies in the same temperature range. The resulting curve was similar to that presented in Fig.2.4. Ramesh et al. [12] also showed that after filing the (100) and (110) peaks disappeared (Fig.2.2). Later, Jang and Koch [17] showed that Ni_3Al could be efficiently disordered by ball milling in a vibrating ball

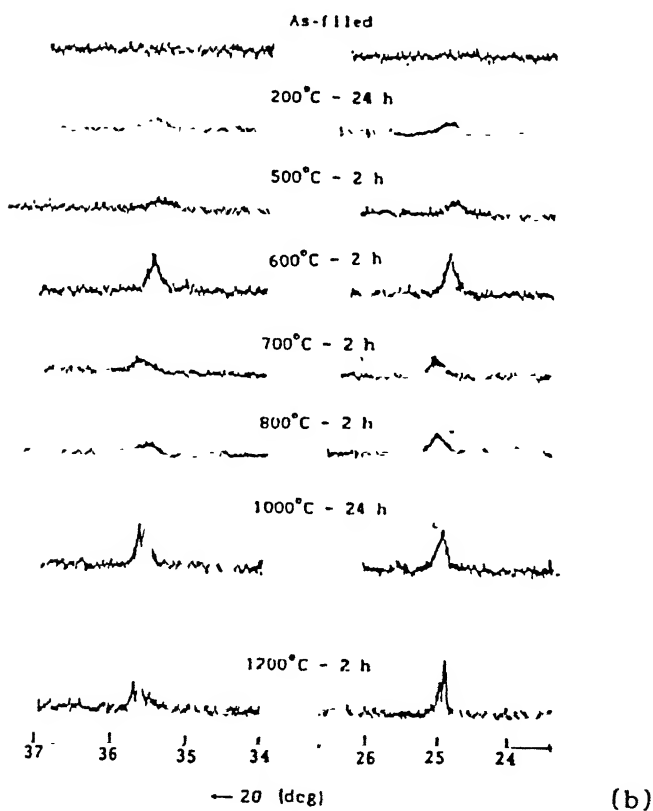


Fig.2.2 : XRD intensity profiles for (a) (111), (200) and (220) reflections; (b) (100) and (110) reflections [12].

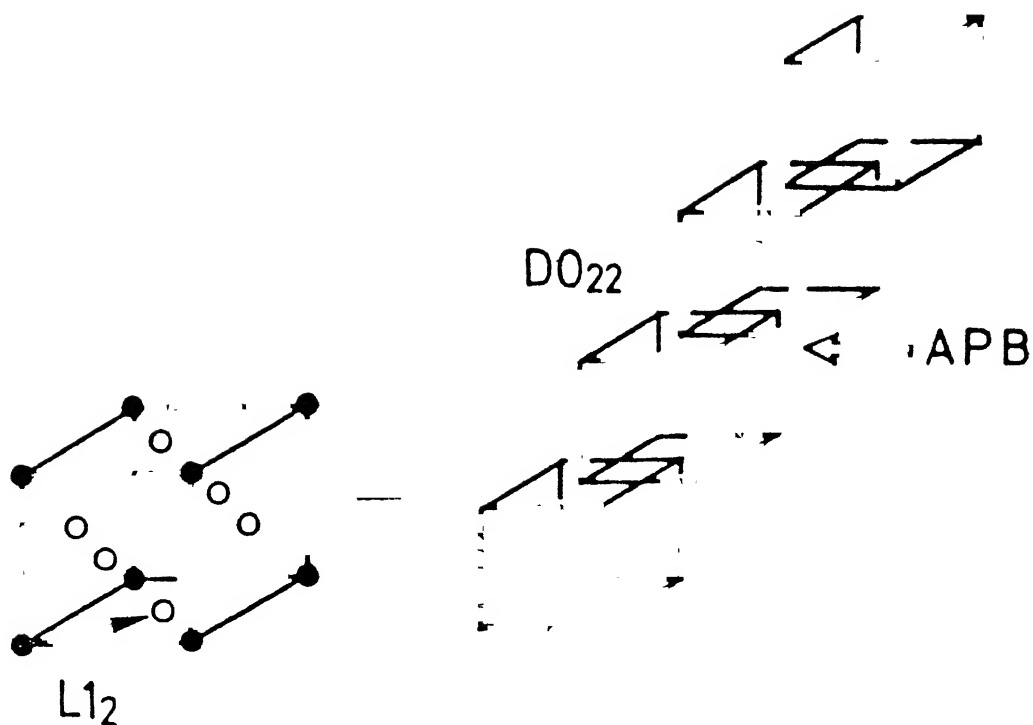


Fig.2.3 : Structural relationship between $L1_2$ and DO_{22} structures [13].

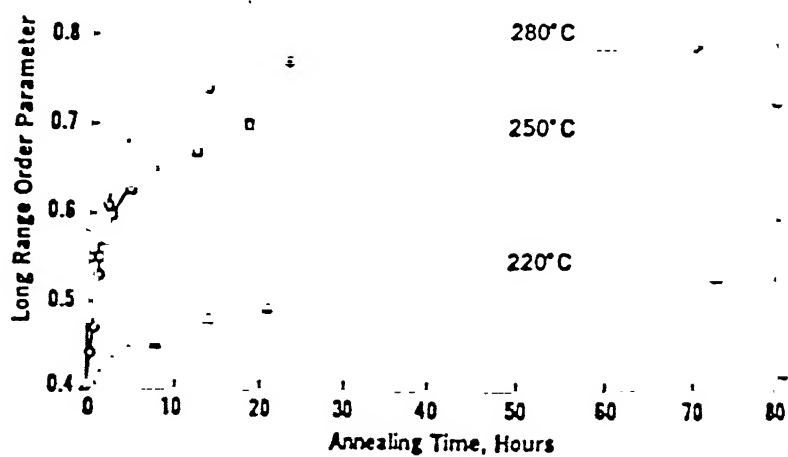


Fig.2.4 : Reordering of mechanically disordered Ni_3Al filings on the basis of (100) and (200) reflections [16].

mill. The intensity of the superlattice lines disappeared with milling time (Fig.2.5). In a recent study, Gialanella et al. [18] found that off-stoichiometric Ni_3Al powders got disordered during ball milling in a planetary mill. They studied this effect by measuring the variation of the integrated intensity ratio between (110) and (200) reflections for increasing milling time (Fig.2.6). Baker et al. [19], from the intensity of their selected area diffraction spots of (100) and (110) reflections suggested that Ni_3Al could be partially disordered by cold rolling. The same view has been expressed by Ball and Gottstein [20] who reported that long range order parameter became 0.6 after 70% cold rolling. They measured the intensities of (100) and (200) reflections from background corrected pole figures.

2.2 Planar Faults :

In FCC metals and alloys, $1/2[110]$ is the burgers vector of a single dislocation whereas in L1_2 alloys that corresponds to a partial dislocation. In Fig.2.7, it has been shown that introduction of a $1/2[\bar{1}01]$ dislocation on (111) plane leads to B-B bonds across the slip plane. However, introduction of another $1/2[\bar{1}01]$ dislocation on the same plane eliminates the wrong bonds. Though $a[100]$ is the shortest unit translation vector, dislocations occur after plastic deformation at all temperatures have burgers vector of $a[110]$. It was reported by Veyssi re et al. [21] that due to this large burgers vector, the dissociation of dislocations are more complex. The dissociation of a superdislocation into superpartials is controlled by a balance between the elastic energy decrease due to dissociation and the energy increase due to the creation of the planar faults between the partial dislocations. Four types of faults on {111} plane of L1_2 structure have been reported [13] i.e. the antiphase boundary (APB), the superlattice intrinsic stacking fault (SISF), the complex stacking fault (CSF) and the superlattice extrinsic

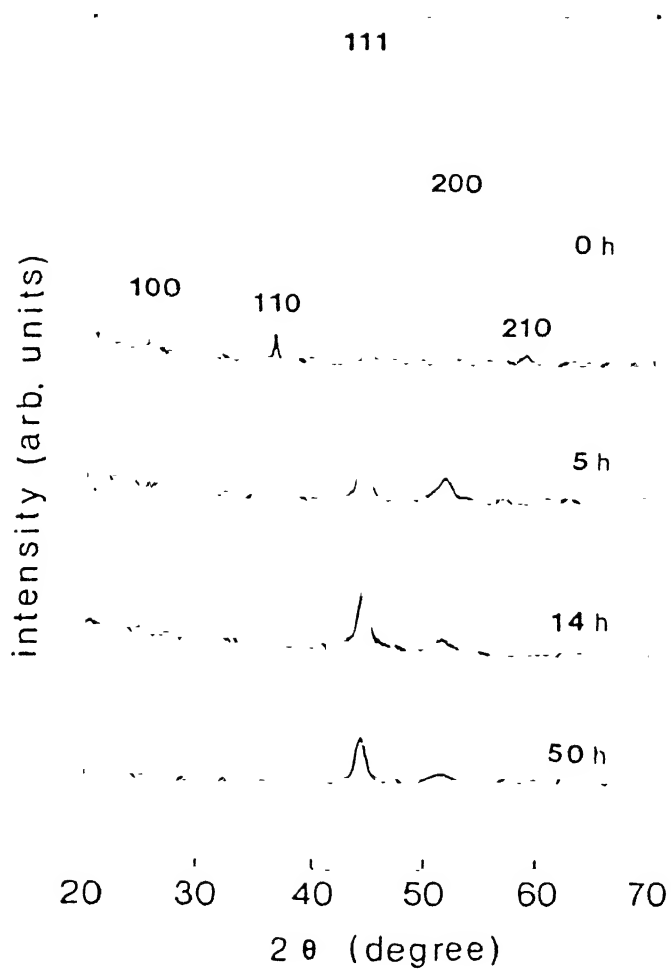


Fig.2.5 : XRD pattern of Ni_3Al powders with milling time [17].

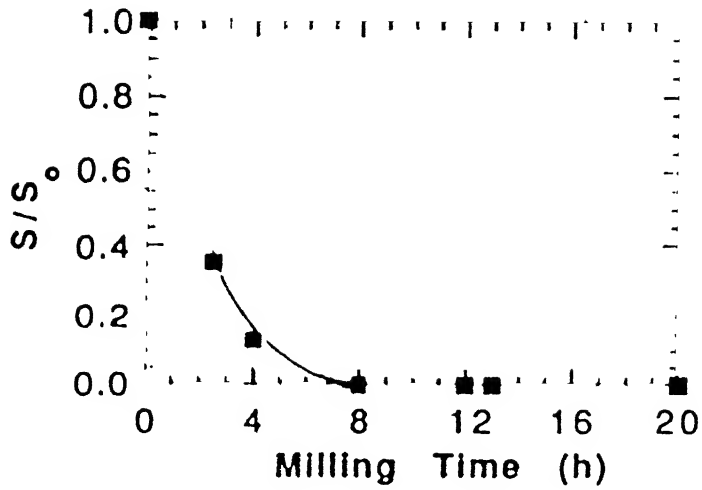


Fig.2.6 : Variation of LRO parameter as a function of milling time on the basis of (110) and (200) reflections [18].

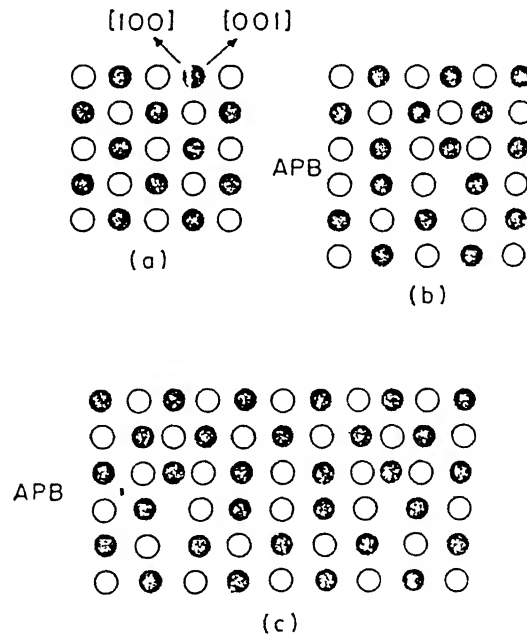


Fig.2.7 : APBs in $L1_2$ structure: (a) (010) plane; (b) $1/2[\bar{1}01]$ dislocation on (111) plane, producing APB; (c) two $1/2[\bar{1}01]$ dislocations on (111) plane with APB between them.

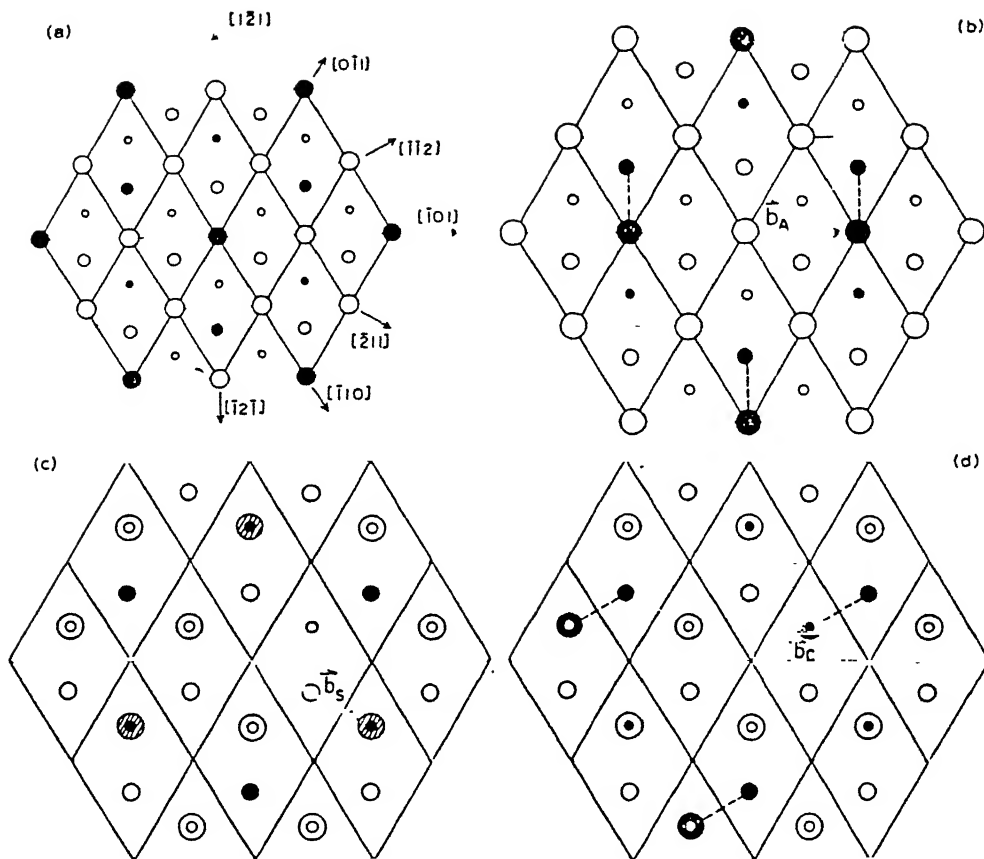
stacking fault (SESF).

As (111) and (010) planes are the important slip planes in Ni_3Al , faults on these planes will be considered. In Fig.2.8(a), three successive layers of (111) planes of an A_3B material are shown. When the top layer 'a' is displaced by the vector $\vec{b}_A = 1/2[\bar{1}01]$ with respect to the layer 'b', an APB is produced as shown in Fig.2.8(b) and the configuration of neighbour is changed. A fault having the same vector but which lies on (010) planes is expected to have a much lower energy because there is no first-nearest-neighbour' bond violations.

Another kind of planar fault which can be produced on (111) planes is also shown in Fig.2.8(c). Here, the top layer 'a' is shifted by $\vec{b}_S = 1/2[\bar{1}\bar{2}1]$, so that the B atoms in the top layer lie directly above the B atoms in the bottom layer. This leads to a change in the stacking sequence fromcbacba..... tocb|cba..... where the line indicates the position of the fault. This is known as SISF. An SISF results in a change in the stacking sequence but does not violate the nearest-neighbour relationship. Such faults can therefore be considered as low energy faults.

A third kind of fault can be produced if the top layer is shifted by $\vec{b}_C = 1/6[11\bar{2}]$ so that the B atoms in the top layer lie directly above the A atoms in the bottom layer. A complex stacking fault (CSF) is thereby produced, as shown in Fig.2.8(d). This results in a local hcp stacking, as in the case of the SISF, but there are also nearest neighbour violations. The CSF is a planar fault similar to an ordinary stacking fault in the FCC structure.

A SESF can be produced by shifting the top layer by $\vec{b}_S = 1/3[21\bar{1}]$ and the shifting of the layer above this by either $1/3[2\bar{1}\bar{1}]$ or by $1/3[11\bar{2}]$. Such a shift converts acbacba..... layer to acb_Icac_Ib..... sequence where the line indicates the position of the fault. This faults results in no



a three (111) planes; b after sliding top layer in a by $b_A = \frac{1}{2}[\bar{1}01]$ to produce APB, dashed lines indicating 'incorrect' B-B nearest-neighbour bonds; c after sliding top layer in a by $b_S = \frac{1}{3}[\bar{2}11]$ to produce SISF; d after sliding top layer in a by $b_C = \frac{1}{6}[\bar{1}\bar{1}2]$ to produce CSF

Fig.2.8 : Four types of faults in A_3B alloy with $L1_2$ structure:

large, medium and small circles represent atoms in upper,
middle and lower (111) planes, respectively; open circle :
A atoms, close circle : B atoms.

first-neighbour violations, only a change in stacking sequence.

A fault will be stable only if the energy of the faulted crystal is lower than that of the same crystal with a slightly smaller or larger fault vector. The relative stability of APB, CSF and SISF has significant influence on the character of dislocation dissociation on {111} planes. The dislocation dissociation schemes have been suggested as follows :

- (i) Dissociation with APB on (111) planes

$$[\bar{1}01] = 1/2[\bar{1}01] + 1/2[\bar{1}01]$$

- (ii) Dissociation with superlattice intrinsic stacking fault

(SISF) on (111) planes

$$[\bar{1}01] = 1/3[\bar{2}11] + 1/3[\bar{1}\bar{1}2]$$

- (iii) Dissociation with APB and complex stacking fault (CSF) on (111) planes

$$[\bar{1}01] = 1/6[\bar{1}\bar{1}2] + 1/6[\bar{2}11] + 1/6[\bar{1}\bar{1}2] + 1/6[\bar{2}11]$$

- (iv) Dissociation with APB on (010) plane

$$[\bar{1}01] = 1/2[\bar{1}01] + 1/2[\bar{1}01]$$

The APB, CSF and SISF energies in Ni_3Al are listed in Table 2.1 [22-27].

Straight screw dislocations are often observed as dipoles in Ni_3Al [28, 29]. The APB dissociation mode prevails during deformation whereas the SISF dissociation mode can be regarded as a by-product of deformation which does not control the intrinsic mobility of dislocations [28]. The most frequently reported configuration in Ni_3Al is the formation of an APB (Fig.2.9) [14, 30]. The SISF dissociation also is observed in deformed samples of Ni_3Al (Fig.2.10) [14, 31, 32]. However, according to Yan et al. [33], SISF is not observed in deformed boron doped Ni_3Al (Fig.2.11). The CSF and APB coupled dissociation are observed in Ni_3Al deformed at elevated temperatures (e.g. 650°C) [34].

Table 2.1 : Fault Energies of Ni_3Al

$\gamma_{\text{APB}} (\text{mJ}/\text{m}^2)$ (111)	$\gamma_{\text{CSF}} (\text{mJ}/\text{m}^2)$ (010)		$\gamma_{\text{SISF}} (\text{mJ}/\text{m}^2)$ (111)	Reference
111 ± 15	90 ± 5		10 ± 5	22
156	28	259	96	23
142	83		13	24
180 ± 20		206 ± 30		25
175		225		26
170		240		27



Fig.2.9 : APB coupled dissociation in Ni_3Al [14].

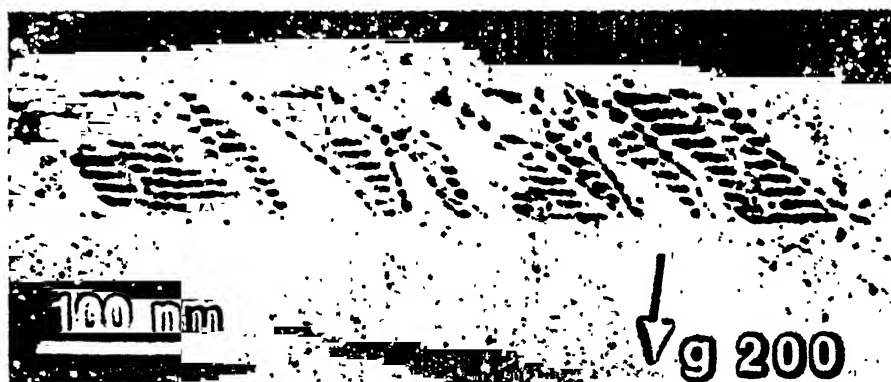


Fig.2.10: SISF coupled dissociation in Ni_3Al [14].

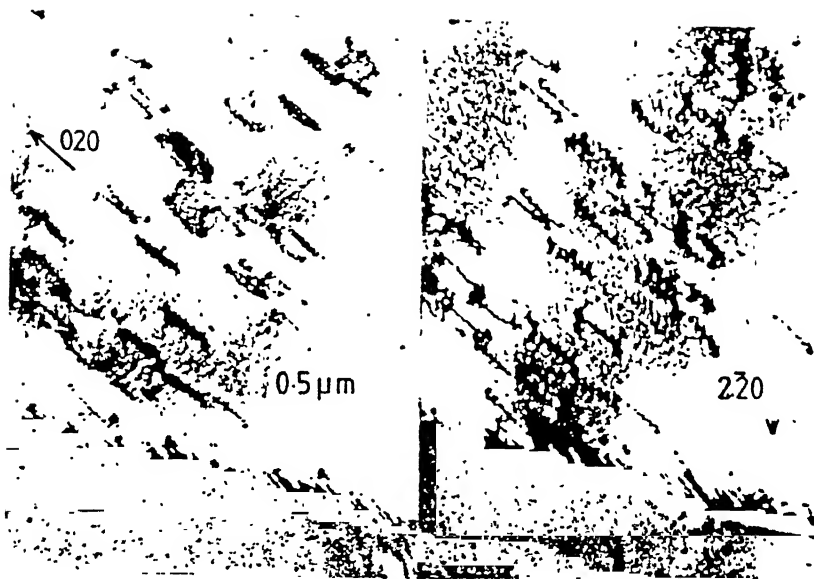


Fig.2.11: APB coupled dissociation in Ni-24at.%Al-1at.%B [33].

2.3 Deformation :

Ni_3Al deforms by $\{111\}\langle 110 \rangle$ slip at low temperature where the positive temperature dependence of flow stress is observed. After the peak, the cube slip $\{001\}\langle 110 \rangle$ becomes dominant. The following differences between the $\{111\}\langle 110 \rangle$ octahedral slip and the $\{001\}\langle 110 \rangle$ cube slip have been found [13]:

- (i) The CRSS for $\{001\}\langle 110 \rangle$ slip obeys Schmid's law, while that for the $\{111\}\langle 110 \rangle$ slip strongly depends on crystal orientation.
- (ii) The flow stress for cube slip is very much sensitive to the strain rate, whereas the strain rate sensitivity of flow stress for octahedral slip is negligibly small.
- (iii) The activation volume for cube slip is two orders of magnitude smaller than that for octahedral slip.

The slip deformation is possible by the movement of dislocations according to the dissociation mode (i) and (ii) described in 2.2.

In L1_2 structure, the primary twin system $\{111\}\langle \bar{1}\bar{2}1 \rangle$ requires atomic shuffling on every other twin plane. This leads to low mobility of twinning dislocations [35]. However, in the complimentary twin system, the shear stress is twice as large as in the primary twin system; but it requires no atomic shuffling.

It is also to be noted that if the shockley partials move on consecutive $\{111\}$ planes, a twin can be produced [35]. However, due to this movement, CSF will be produced but it is associated with a higher energy compared to other fault energies (Table 2.1). The existence of such fault has never been found in Ni_3Al at low temperature. The evidence of CSF at higher temperature [34] can be correlated with the above argument because at this temperature, the required atomic shuffling or the shear is not difficult and that may lead to twin formation.

2.3.1. Yield Strength Anomaly :

The yield stress of both single and polycrystalline Ni_3Al has been observed to increase with increase in temperature. This anomalous variation in flow stress was first observed by Flinn [36] in polycrystalline Ni_3Al . Fig.2.12 shows the variation of yield stress of Ni_3Al alloy with temperature. The figure shows a peak in the yield stress in the temperature range of $600^\circ\text{--}700^\circ\text{C}$. The position of the peak stress and its height have been found to be dependent on crystal orientation, solute addition and grain size.

Several mechanisms have been suggested to account for this phenomena. The most widely accepted ones are mainly based on the difference in the core configurations and mobilities of dislocations on $\{111\}$ and $\{001\}$ planes.

Kear and Wilsdorf [37] first proposed a 'cross-slip' mechanism in which some parts of a moving screw dislocations on the $\{111\}$ glide plane cross-slip on the energetically favourable $\{001\}$ plane; this reduces the mobility of the whole dislocation giving rise to an increase in the flow stress. The flow stress increase becomes remarkable at intermediate temperatures since cross-slip can occur more easily when the deformation temperature increases. The positive temperature dependence of the CRSS and a violation of Schmid's law for $\{111\}\langle 110 \rangle$ slip can be interpreted by the so-called 'dynamical break away' process of screw dislocations (Fig.2.13) since the driving force to produce the dragging points is given by the stress component of the applied stress on the $\{001\}$ plane and production of which is due to a thermally activated process.

Later this theory was modified by several investigators such as Takeuchi and Kuramoto [38], Lall et al. [39], Paider et al. [40], Yoo [41] and Vessière [42]. Though there were a lot of theoretical as well experimental work [43-46] on this anomalous behaviour, but there are still a lot of ambiguity to be explained :

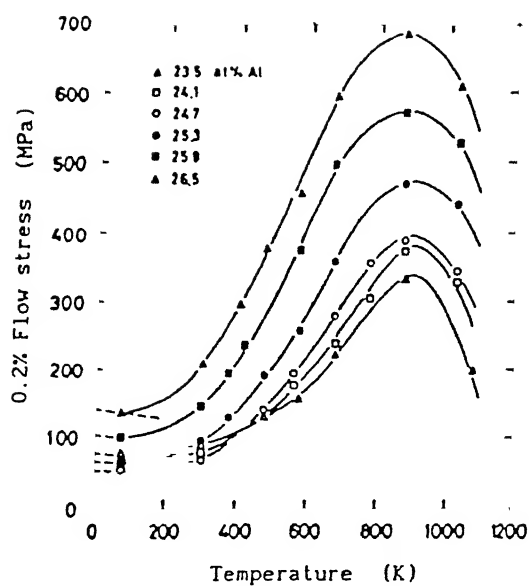


Fig.2.12: Temperature dependence of flow stress of Ni_3Al alloy [11]

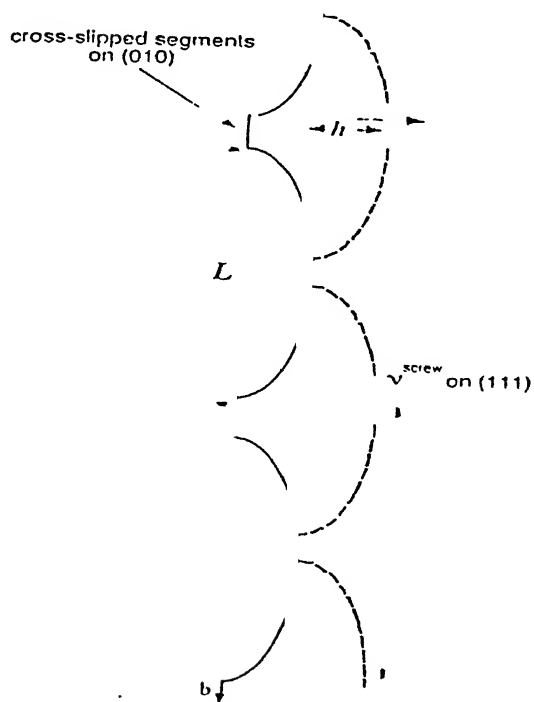


Fig.2.13: Dynamic breakaway model utilized by cross-slip pinning model [37].

(i) Deformation is temperature-path history independent (TPHI) [47]. So, dislocation glide is dynamic and changes in temperature will result in immediate and reversible changes in the flow stress.

(ii) The flow stress of $L1_2$ alloys are markedly orientation dependent. The peak temperature varies with orientation [48]. Above the peak temperature, the cube slip is governed by Schmid's law [38].

(iii) Different strengths are obtained in tension and compression [38]. The flow stress in tension σ_T is larger than that in compression σ_C .

(iv) Strength is virtually independent of strain rate [49]. It suggests that the pinning points of cross-slipped dislocations are assumed to be inherently reversible obstacles with an extremely short lifetime. So, the characteristic time (t_c) associated with a deformation increment (ϵ), ($t_c = \epsilon/\dot{\epsilon}$) is much larger than the time required to obtain an equilibrium density of cross-slipped segments.

2.3.2. Ductility :

The intermetallics show poor ductility and can not be deformed plastically because of their strong tendency to cleave in grain interior and to fracture at grain boundaries. There are many possible causes of this brittle fracture :

(a) Intrinsic factors such as weak grain boundary cohesion, poor cleavage strength and insufficient number of slip systems.

(b) Extrinsic factors such as impurity segregation to grain boundaries and environmental embrittlement.

Out of those above factors, weak grain boundary cohesion and environmental embrittlement are considered to be the major factors for the brittle fracture of Ni_3Al .

Several theoretical arguments have been put forward to explain the intrinsic grain boundary brittleness. Takasugi and Izumi [50] suggested that

alloys having large valency difference between their constituent atoms were more prone to intergranular fracture than those having small valency differences. Taub et al. [51] emphasized that electronegativity difference should be used rather than valency difference. King and Yoo [52] attributed the intrinsic grain boundary brittleness of Ni_3Al to the considerably fewer dislocation reactions that were permissible at strongly ordered grain boundaries than at compositionally disordered ones. Vitek et al. [53] using computer simulations found that the atomic structure of grain boundaries in strongly ordered compounds, like Ni_3Al , contained columns of atomic size cavities. These cavities act as nuclei for intergranular cracks and weaken the grain boundary. Later, Chiba et al. [54] pointed out that propensity of intergranular fracture increased with increasing ordering energy.

From the above points of view, the following methods can be suggested to overcome the brittleness of grain boundary :

(a) alloying with interstitial solutes :

By boron doping, fracture mode changes from brittle grain boundary fracture to ductile transgranular fracture [2, 55]. However, boron doping has been found to be effective only in hypostoichiometric Ni_3Al ($\text{Al} < 25 \text{ at.}\%$) whereas there is no effect on stoichiometric or hyperstoichiometric Ni_3Al ($\text{Al} > 25 \text{ at.}\%$) [56]. Fig.2.14 shows the effect of boron doping and stoichiometry on the ductility of Ni_3Al [2].

Boron was found to segregate on the grain boundary rather than grain interiors. This unusual type of segregation effect on grain boundary cohesion had been predicted by Rice [57] by classical thermodynamics. Liu et al. [2] used this concept to explain their findings on boron-induced ductilization of Ni_3Al alloy.

The work necessary to cause fracture (γ_{id}) is correlated to the surface energy (γ_{s}) and the grain boundary energy (γ_{gb}) by the following relation :

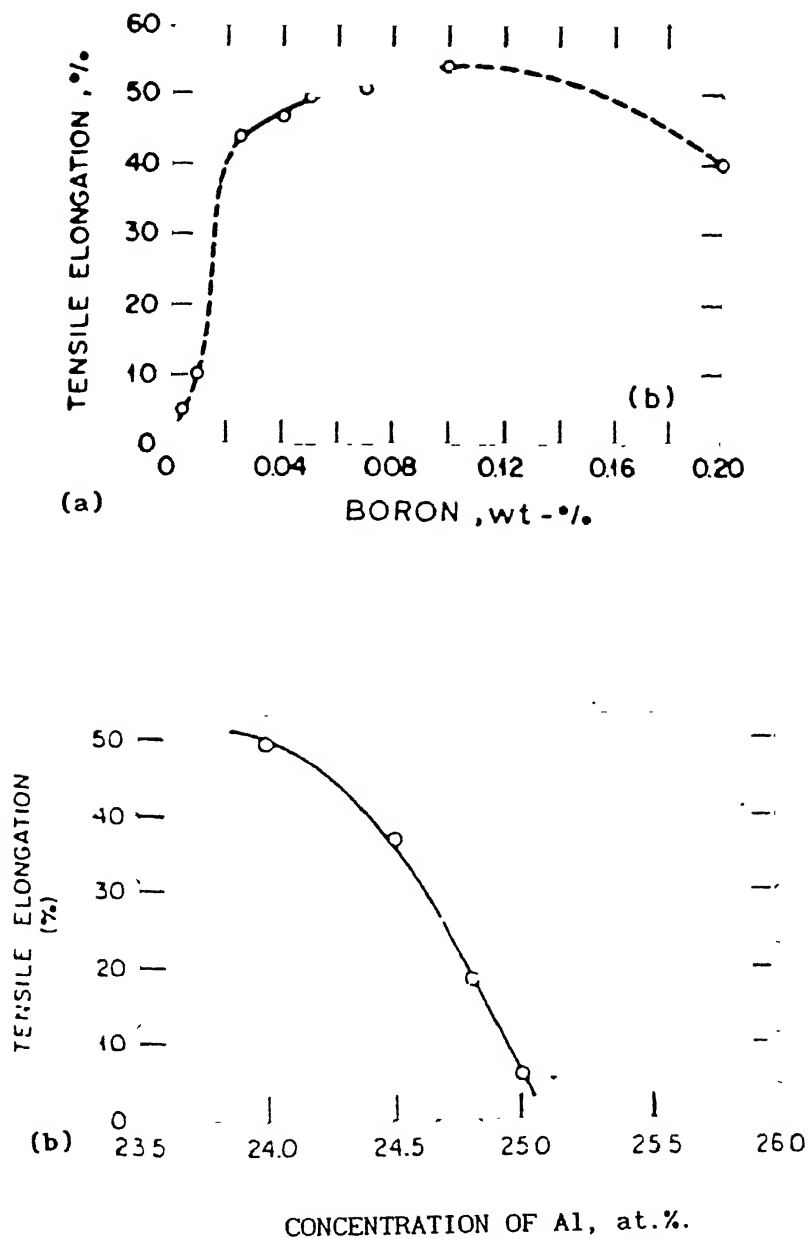


Fig.2.14: (a) Effect of boron concentration, (b) effect of aluminium concentration on the ductility of Ni_3Al [2].

$$\gamma_{id} = 2\gamma_s - \gamma_{gb}$$

γ_{id} is equivalent to the grain boundary cohesive energy. According to Rice's thermodynamic theory, the segregation behaviour of boron leads to increase in the value of γ_{id} i.e. the cohesive energy. Increased grain boundary cohesion not only suppresses crack nucleation, but by providing increased crack-tip plastic deformation and blunting, also suppresses crack propagation. These effects are so pronounced in boron-doped Ni_3Al that ductility is dramatically increased and the alloy fractures in a transgranular fashion.

Schulson, Baker and co-workers [58-60] have found that Ni_3Al gets strengthened due to boron addition. According to them, boron facilitates dislocation motion within the grain boundary plane; thereby easing the accommodation of strain resulting from dislocation pile-up at the boundary and lowering the stress intensity required for the transfer of slip from one grain to the other. The same authors [58-60] gave atomistic reason for their observation on the ease of the transfer of slip. They suggested that if the Al-B interaction is stronger than the Ni-B interaction then the difference in energy between an Al-Al rich grain boundary and an Al-Al poor one should be reduced. Thus, a grain boundary dislocation will experience a lower drag; these will allow easier accommodation of boundary shear.

Baker and Schulson [61] observed a continuous disordered (γ) grain boundary phase in boron-doped Ni-24 at.% Al produced by powder metallurgy. The grain boundary phase has a thickness of ≈ 20 nm with a boundary separating it from the matrix (γ'). Presence of disordered regions of ≈ 2 nm thickness were detected in the vicinity of large angle boundaries in Ni-24 at.% Al doped with boron by HREM studies [62]. Observations using microdiffraction [63], showed partially ordered regions (≈ 10 nm wide) adjacent to low angle boundaries in doped Ni-rich alloy. Based on the above observations, Baker and Schulson suggested that partially disordered grain boundary might be a

prerequisite for easy transmission of slip across grain boundaries via direct passage of dislocations. The enhanced mobility of dislocations lead to global plasticity.

However, the controversy regarding the boron-induced ductilization, whether it is due to grain boundary cohesion or due to easier slip transfer across grain boundaries, is still persisting and researches are continuing in this direction.

(b) alloying with substitutional solutes :

The grain boundary structure can be modified by alloying with substitutional elements. Pak and Inal [64] pointed out that in strongly ordered alloys, nearest-neighbour bonds between unlike atoms are the strongest bonds; but many broken bonds are present across these ordered grain boundaries which lead to weak boundaries. The enhancement of ductility due to macroalloying has been explained by the following models such as Valency model [65], Electronegativity model [50] and Ordering energy model [54]. The solutes found to ductilize Ni_3Al are Pd, Cu, Co, Au, Pt and Ag with the composition of $\text{Ni}_{75}\text{Al}_{25-x}\text{C}_x$ (C is the solute).

(c) Thermomechanical Treatment :

The ductility of the boron-doped Ni_3Al alloy has been significantly improved by grain refinements through thermomechanical treatments. By thermomechanical treatments, the grain size could be of the order of few microns and in this case, ductility will be extended upto the superplastic range [66]. The ductility can be maintained at high temperature, if the structure is fine. Stoloff and Dillamore [67] showed that cold rolling of an Fe-40Co-2pct.V alloy (B2 structure) in the disordered condition, followed by a recovery annealing, could significantly increase the room-temperature tensile ductility. Later, Schulson [68] also reported a similar effect of working on the ductility of NiAl.

2.3.3. Deformation Texture :

The textures developed in FCC metals and alloys are generally described by two types of nomenclatures ; one is known as 'pure metal or copper type' and the other one is 'alloy type or α -brass type'. The pure metal type texture usually contains four texture components. These are the Cu component $\{112\}\langle 111 \rangle$, the B_s component $\{110\}\langle 112 \rangle$, the S component $\{123\}\langle 634 \rangle$ and the Goss component $\{011\}\langle 100 \rangle$. However, the alloy type texture consists of mainly the B_s component $\{110\}\langle 112 \rangle$ along with the Goss. Standard (111) pole figures illustrating these two types of deformation textures are shown in Fig.2.15.

There are a limited number of investigations on the deformation texture of $L1_2$ alloys. Hutchinson et al. [69] found that in ordered Cu_3Au , the texture after cold rolling (90%) was mainly copper type. They described the texture as a string of orientations extending from $\{112\}\langle 111 \rangle$ through $\{123\}\langle 412 \rangle$ and $\{110\}\langle 112 \rangle$ to $\{011\}\langle 100 \rangle$. However, the mechanism of development of this texture was not investigated.

The rolling texture of boron-doped Ni_3Al investigated by Gottstein et al. [70] consists of the B_s component $\{110\}\langle 112 \rangle$ and the Goss component $\{011\}\langle 100 \rangle$ (Fig.2.16). According to them, the origin of this brass rolling texture was due to heavy shear band formation which resulted from the strong work hardening of the material.

Recently, Ball and Gottstein [20] found that the rolling texture of cold rolled $Ni_3Al(B)$ was of copper type with a strongly scattering components which remained weak even after heavy deformation (Fig.2.17). From their TEM work, they observed microband clusters as well as shear bands on the longitudinal sections of 70% cold rolled samples (Fig.2.18). They proposed that the microband formation was associated with local disordering in the slip bands. They attributed that development of this weak texture could be due to formation of microbands associated with local disordering in heavily

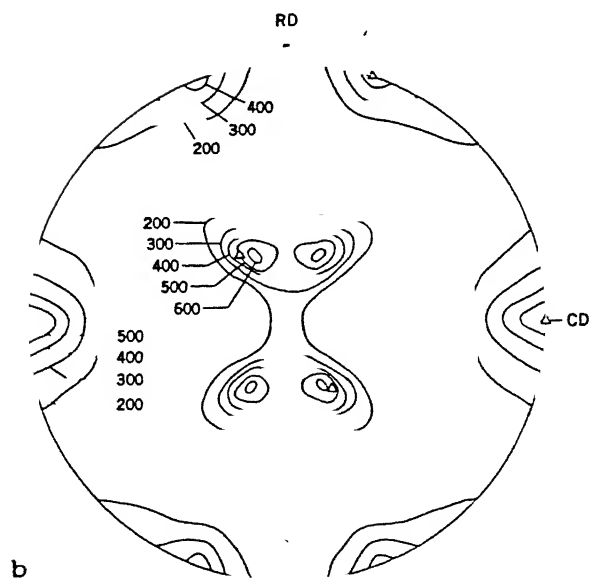
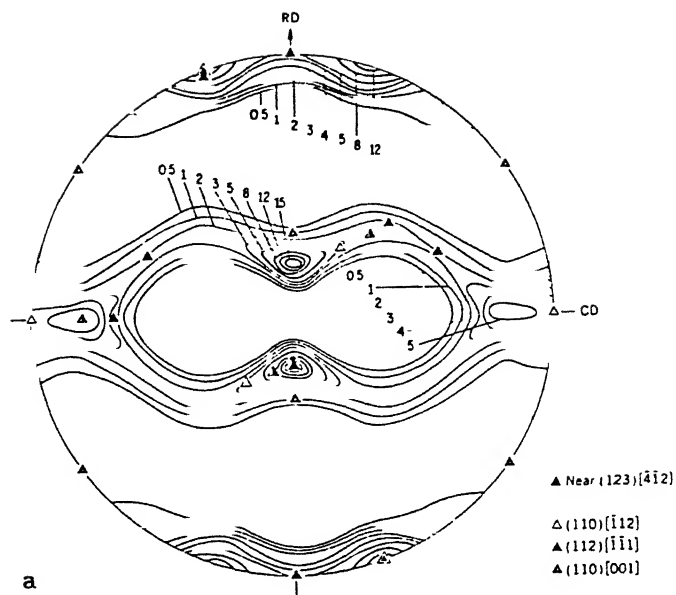


Fig.2.15: Standard {111} pole figures of (a) Copper and (b) Brass.

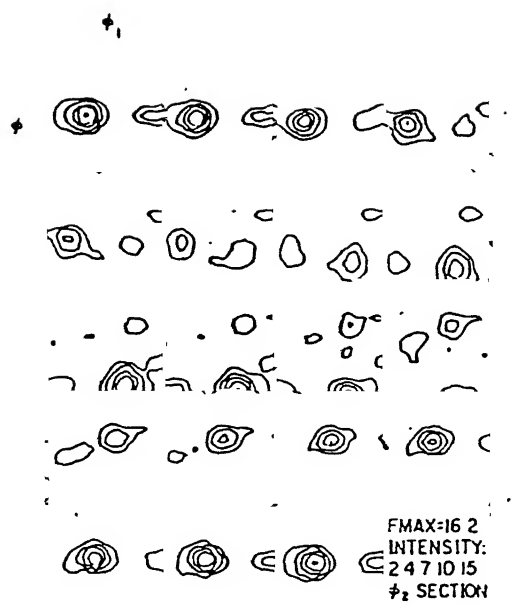


Fig.2.16: ODF of 90% cold rolled boron-doped Ni_3Al [70].

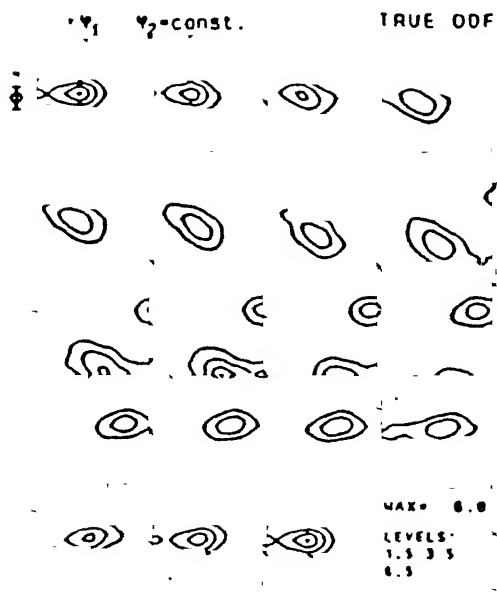


Fig.2.17: ODF of 92% cold rolled boron-doped Ni_3Al [20].

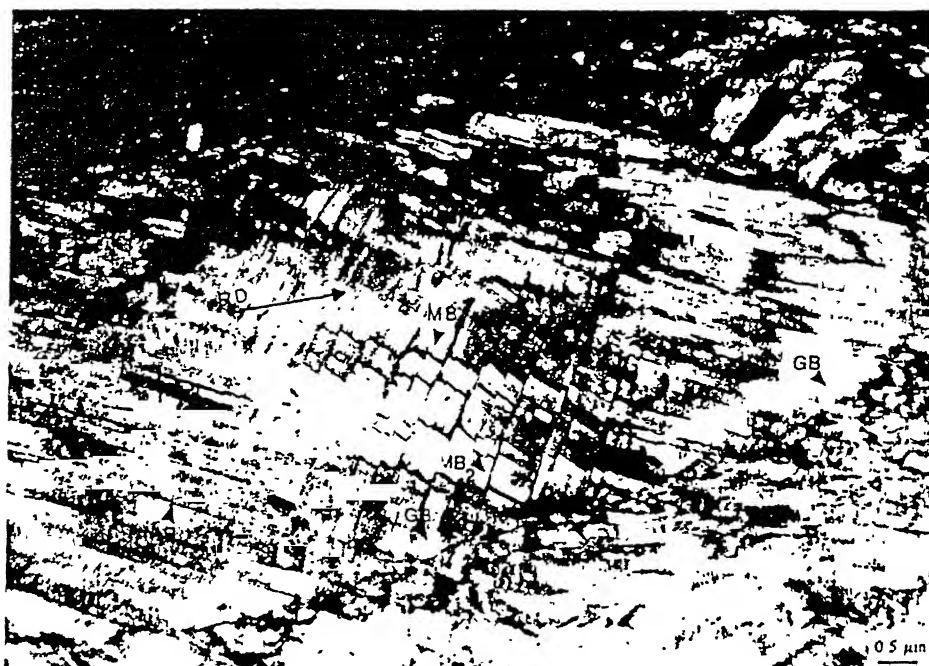


Fig.2.18: TEM micrograph of the longitudinal section of 70% cold rolled boron-doped Ni_3Al [20].

activated slip bands. As described above, the deformation mechanism in $L1_2$ alloys is not clear; hence the mechanism for the development of deformation texture is still ambiguous.

2.4 Diffusion :

Diffusion in ordered alloys is of considerable interest for understanding the high temperature behaviour of the ordered intermetallic compounds. The theoretical treatments of diffusion in ordered alloys are much more complicated because of the atomic interaction between the diffusing species. In other words, atomic jump in an ordered alloy strongly depends on the nature of ordering in the immediate environment at the microscopic level. Considering diffusion via the vacancy mechanism, when diffusing atoms exchange with vacancies, they tend to leave behind traces of disordered region and locally deviate from thermodynamic equilibrium. In order to maintain equilibrium, the migration of atoms must occur in a way or sequence to compensate or minimize the increase of energy during diffusion. As a result, diffusion in ordered alloys is strongly correlated; the degree of correlation (or order) is a function of composition and temperature.

Diffusion in ordered alloys tends to be much slower than in disordered alloys. Slow rates of diffusion has the advantage of improved microstructural stability at elevated temperatures. Although, the diffusion of ordered intermetallics has high technical importance, relatively little work has been done on this aspect.

Hancock [71] and Bronfin et al. [72] conducted tracer diffusion measurements of Ni in Ni_3Al in the range of $920^\circ - 1200^\circ C$. The diffusivity of Ni was found to be independent of composition and the activation energy for diffusion was insensitive to aluminium content. The above findings had been attributed to the temperature independent defect concentration i.e. the

constitutional vacancies, or the vacancies introduced by impurities such as 3 wt.ppm Si in these samples [71]. It was Aoki and Izumi [73] who reported that Ni_3Al did not have any constitutional vacancies on either side of the stoichiometry. Only substitutional anti-site defects occur.

Hosino et al. [74] reported that the diffusivity of ^{63}Ni in Ni_3Al was independent of Al content in binary Ni_3Al above 1000°C ; however, there was a minima in diffusivity at the stoichiometric composition between 692° to 1000°C . The diffusivity of Ni in binary Ni_3Al is shown in Fig.2.19. The diffusivity changes at about 925°C . The deviation at low temperature was suggested to be due to the presence of temperature independent vacancy concentration. Das Gupta et al. [75] indicated that three types of vacancies exist only in Al-rich and stoichiometric alloys; whereas Sun and Lin [76] totally disregarded the presence of any constitutional vacancies in off-stoichiometric Ni_3Al . The activation energies for volume diffusion of Ni and Al in Ni_3Al are tabulated in Table 2.2.

Addition of boron resulted in increased diffusivity of Ni for all aluminium contents at 1200°C and for stoichiometric alloys in the temperature range of 692° to 1352°C [74]. However, previous work did not show any effect of B [75]. The enhanced diffusivity due to boron can be due to higher concentration of vacancies than in binary Ni_3Al alloy.

In intermetallic compounds, random vacancy jumps would disrupt the ordered arrangement of atoms on lattices. Sun and Lin [76] considered the anti-site defects and found that these could explain the low diffusivity of Ni in Ni_3Al at the stoichiometric composition below 727°C . In Ni_3Al , Ni atoms may not jump onto 4 Al sublattice sites of their 12 nearest neighbour sites, which leads to a decrease of the correlation factor from 0.7815 to 0.727. Since, constitutional anti-site defects exist on both sides of stoichiometry, diffusivity will increase with the higher concentration of anti-site defects

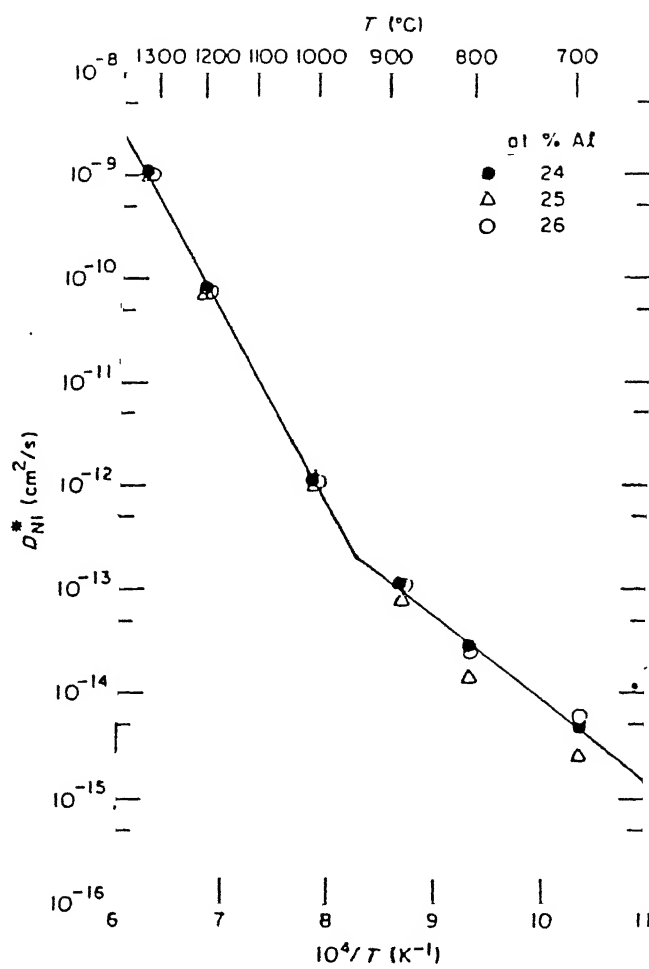


Fig.2.19: Temperature dependence of D_{Ni}^* in pure Ni_3Al [74].

Table 2.2 : Activation Energies and Frequency Factors for Ni and Al in

Ni₃Al

	D_0 (m ² /s)	Q (kJ/mol)	C (at.% Al)	T (K)	Ref.
Ni	4.41×10^{-4}	306	23.8	1190-1471	71
	1.00×10^{-4}	303	25.3	1187-1513	71
	3.11×10^{-4}	300	26.8	1190-1557	71
	1.00×10^{-4}	287	25.3	1187-1513	72
	1.32×10^{-2}	345	24	1200-1623	74
	1.46×10^{-2}	347	25	1200-1623	74
	1.05×10^{-2}	342	26	1200-1623	74
	1.0×10^{-11}	135	24	965-1273	74
	1.1×10^{-11}	141	25	965-1273	74
	2.0×10^{-12}	122	26	965-1273	74
Al	6.6×10^{-8}	185	25	1273-1473	77

in non-stoichiometric Ni_3Al . The concentration of anti-site defects in stoichiometric Ni_3Al increases with temperature. This also confirms that the diffusivity of Ni in Ni_3Al will be independent of bulk composition above a definite temperature which was also reported by Hosino et al. [74]. However, high concentration of antisites will increase the correlation factor for Ni diffusion.

Hancock [71] pointed out that the ratio of activation energy for migration (E_m) to the activation energy for diffusion ($E_m + E_f$) is more than 0.5. It has been suggested that diffusion in Ni_3Al is more complicated than mere exchange of vacancies.

Grain boundary diffusivities in Ni_3Al have been measured in the temperature range $955^\circ - 1124^\circ\text{C}$ using $\text{Ni}/\text{Ni}_3\text{Al}+\text{B}$ couple [78]. It was found that the grain boundary diffusivities of Ni are 5-6 orders of magnitude greater than the volume interdiffusion coefficient; however, the activation energy for grain boundary diffusion is higher than that for volume diffusion. Later, Yasuda et al. [79] pointed out that the Matano interface employed by Chou and Chou [78] were in fact placed in the γ region and this might lead to erroneous result.

2.5 Recrystallization :

Recrystallization is a major phenomenon that occurs during processing of structural materials. As discussed in the previous chapter, the diffusivity of ordered alloys is very low; hence recrystallization which is a diffusion dependent transformation, becomes sluggish. Ordering leads to changes in the kinetics of recovery and recrystallization compared to alloys which do not undergo ordering. It has been shown that recrystallization sets in at a temperature $T \geq T_c$ [80], where T_c is the order-disorder transition temperature. However, the effect of ordering on recrystallization is not yet

in non-stoichiometric Ni_3Al . The concentration of anti-site defects in stoichiometric Ni_3Al increases with temperature. This also confirms that the diffusivity of Ni in Ni_3Al will be independent of bulk composition above a definite temperature which was also reported by Hosino et al. [74]. However, high concentration of antisites will increase the correlation factor for Ni diffusion.

Hancock [71] pointed out that the ratio of activation energy for migration (E_m) to the activation energy for diffusion ($E_m + E_f$) is more than 0.5. It has been suggested that diffusion in Ni_3Al is more complicated than mere exchange of vacancies.

Grain boundary diffusivities in Ni_3Al have been measured in the temperature range $955^\circ - 1124^\circ\text{C}$ using $\text{Ni}/\text{Ni}_3\text{Al}+\text{B}$ couple [78]. It was found that the grain boundary diffusivities of Ni are 5-6 orders of magnitude greater than the volume interdiffusion coefficient; however, the activation energy for grain boundary diffusion is higher than that for volume diffusion. Later, Yasuda et al. [79] pointed out that the Matano interface employed by Chou and Chou [78] were in fact placed in the γ region and this might lead to erroneous result.

2.5 Recrystallization :

Recrystallization is a major phenomenon that occurs during processing of structural materials. As discussed in the previous chapter, the diffusivity of ordered alloys is very low; hence recrystallization which is a diffusion dependent transformation, becomes sluggish. Ordering leads to changes in the kinetics of recovery and recrystallization compared to alloys which do not undergo ordering. It has been shown that recrystallization sets in at a temperature $T \geq T_c$ [80], where T_c is the order-disorder transition temperature. However, the effect of ordering on recrystallization is not yet

conclusively known. The recrystallization behaviour of different alloys having $L1_2$ structure is considered below.

Cu_3Au : This alloy undergoes an order-disorder transformation at around $390^\circ C$. It can also be disordered due to cold work [81, 82]. Roessler et al. [81] studied the annealing response of cold worked ($\sim 63\%$ reduction) polycrystalline ordered Cu_3Au at temperatures below T_c . During annealing, they found evidences for strain-age hardening. The order parameter which had gone down with the cold work, regained its value at the peak hardness.

Later, Feller-Kniepmeier and Ruckert's [83] showed that at low strains, the excess vacancy concentration was low and ordering was sluggish enough to allow some recovery. However, heavily worked samples ordered quickly and recovery as well as recrystallization stopped below T_c .

Hutchinson et al. [69] investigated the kinetics of recrystallization in a 90% cold rolled Cu_3Au . The kinetics investigated both above and below T_c followed the normal sigmoidal curve. However, the rate of recrystallization was severely slowed down in the presence of order (Fig. 2.20). Recovery as indicated by the decrease in half intensity line breadth was not affected by the state of order. The activation energy for recrystallization in the ordered state was found to be lower than that in the disordered state.

They also determined the texture of the recrystallized sample. Annealing above T_c gave rise to a weak texture consisting of cube component $\{100\}\langle 001\rangle$, its twin and the retained deformation texture, $\{112\}\langle 111\rangle$. However, annealing below T_c developed a stronger texture comprising of all deformation texture components, $\{112\}\langle 111\rangle$, $\{123\}\langle 412\rangle$, $\{110\}\langle 112\rangle$ and $\{011\}\langle 100\rangle$ with a reduction of sharpness compared to the deformed state.

According to them, the high angle grain boundaries in the ordered phase lead to differences in misorientation across the boundary. Therefore, the migration of these grain boundaries will lead to an increase of the

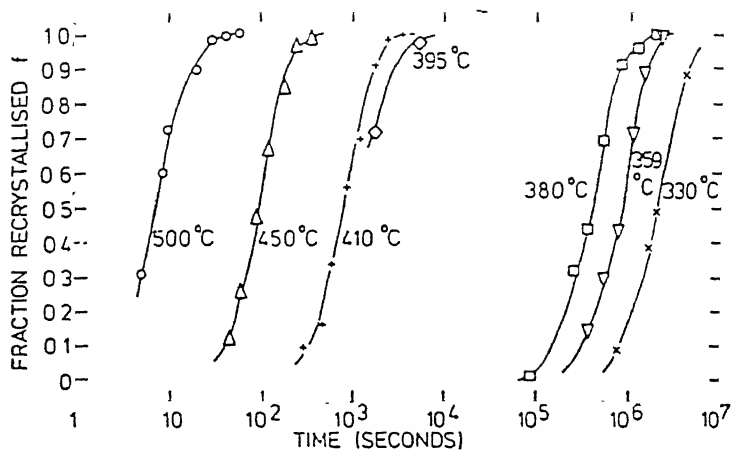


Fig.2.20: Recrystallization volume fraction vs annealing time for 90% cold rolled Cu_3Au [69].

activation energy. For low and medium angle boundaries, the coherency between the two grains is maintained and migration does not require high activation energies. This was derived from their results and reproduced in Fig.2.21. So, the low angle boundaries take part in recrystallization of the ordered structure. This behaviour is also consistent with the textural development in this material during annealing.

Ni₃Fe : The ordering temperature for this alloy is 500°C. Vidoz et al. [84] found that alloys close to stoichiometry i.e. perfectly ordered alloys strain-age hardened strongly; while those away from stoichiometry did not harden but softened gradually during recrystallization (Fig.2.22). The strain age-hardening can be attributed to the change in work-hardenability after deformation followed by ordering. Hardness isotherms plotted in Fig. 2.23 show that after initial increase the hardness drops only at about 525°C which is well above T_c . Hence, the ordering phenomena precedes recrystallization below T_c and that reduces the elastic strains in the cold worked alloy. This in turn hinders the progress of recrystallization.

Co₃Ti : This alloy is ordered upto its melting point. Takasugi et al. [85] found from their hardness results that recovery preceded recrystallization. The recrystallization behaviour was also sluggish.

Zr₃Al : Gagné and Schulson [86] found that recrystallization behaviour in this alloy was normal as it was not prevented by ordering. The short term hardness maxima during annealing of cold rolled alloy was due to the transient increase in faulting. Later, Gialanella et al. [18] found that Zr₃Al could be disordered by ball milling. So, the above concept of fault induced hardness maxima can not be valid.

(Co₇₈Fe₂₂)₃V : The ordering temperature of this alloy is nearly about 950°C. Cahn et al. [87] found sluggish recrystallization behaviour; but the recovery took place before recrystallization. It can be seen that, at T_c , the

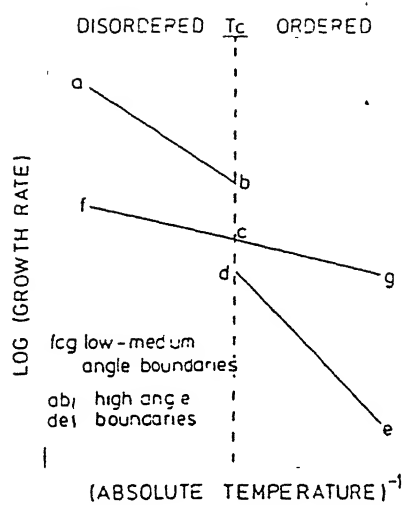


Fig.2.21: Schematic Arrhenius plot of migration rates for grain boundaries in the ordered and disordered states [69].

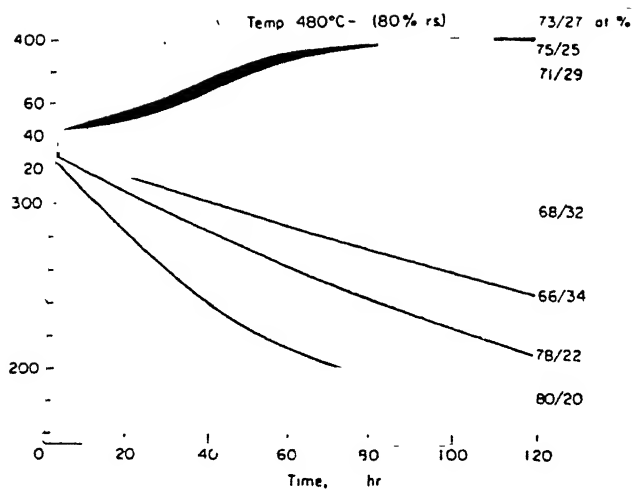


Fig.2.22: Long term hardening kinetics at 480°C of different Ni_3Fe alloys [84].

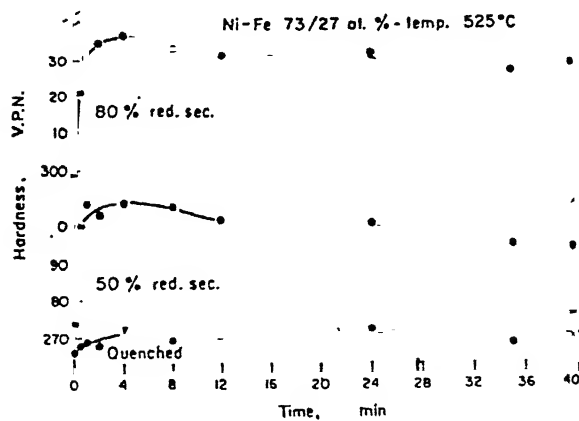


Fig.2.23: Short term hardening kinetics at 525°C in Ni_3Fe [84].

time for 50% recrystallization suddenly drops by a factor of 300 (Fig. 2.24). So, it is the order parameter which reduces the grain boundary mobility.

Ni₃Al : This alloy is ordered upto its melting point. Baker et al. [19] found that Ni₃Al could be partially disordered by cold rolling. By measuring hardness, Baker et al. [19] showed that recovery preceded recrystallization (Fig.2.25). However, the initial material before rolling was a single crystal.

The most comprehensive study on this alloy was done by Gottstein et al. [70]. They found that the kinetics of recrystallization followed the Avrami equation but the rate was sluggish (the recrystallization temperature was about $0.55 T_m$). They also determined the texture after annealing. Like other FCC metals, cube texture was not found; rather some other component was observed. This texture continued to change with annealing at different temperatures; $\{310\}\langle 135 \rangle$ and $\{211\}\langle 135 \rangle$ at 650°C and $\{310\}\langle 135 \rangle$ at 700°C (Fig.2.26).

Zhou et al. [88] found that the effect of boron was very small on the activation energy for recrystallization. Hence, the concept of drag force on the moving grain boundary by boron atoms can be ruled out.

Later, Jena et al. [89] confirmed the presence of extensive recovery from their calorimetric study of a 35% cold rolled hypostoichiometric Ni₃Al(B). Due to recovery, the recrystallization kinetics which followed the Avrami relation was slow. They found that nucleation started by strain-induced grain boundary migration as well as at deformation bands and grain boundaries. Comparing the findings of other investigations, they concluded that at low deformation levels the nucleation and growth rate decreased with time due to exhaustion of the nucleation sites and this led to higher activation energy; whereas at higher deformation levels, growth determined the kinetics of the transformation.

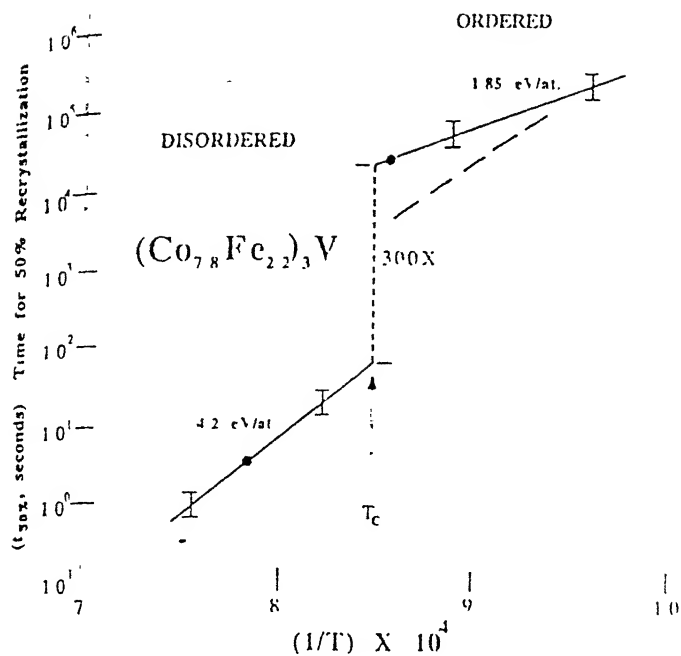


Fig.2.24: Time for 50% recrystallized volume fraction of 50% cold rolled $(\text{Co}_{78}\text{Fe}_{22})_3\text{V}$ annealed above and below T_c [87].

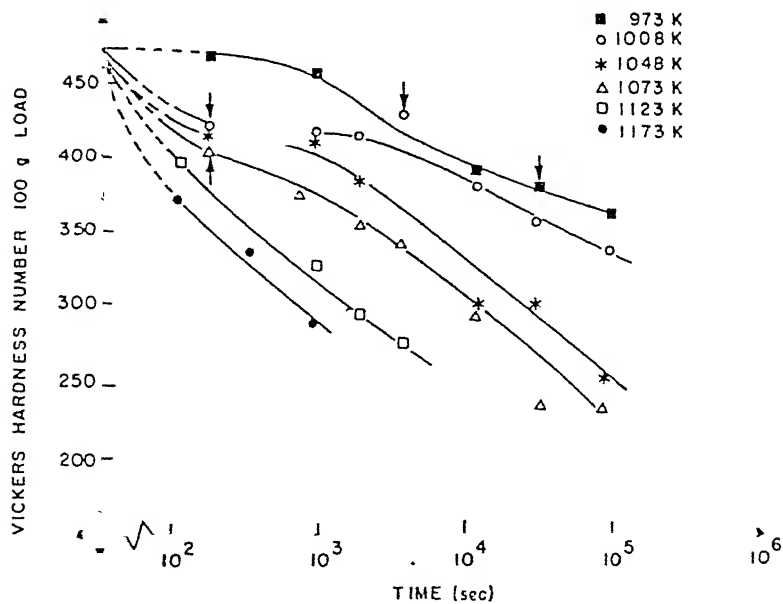


Fig.2.25: Reduction of hardness in Ni_3Al during annealing at various temperatures. '↑' denote starting of recrystallization [19].

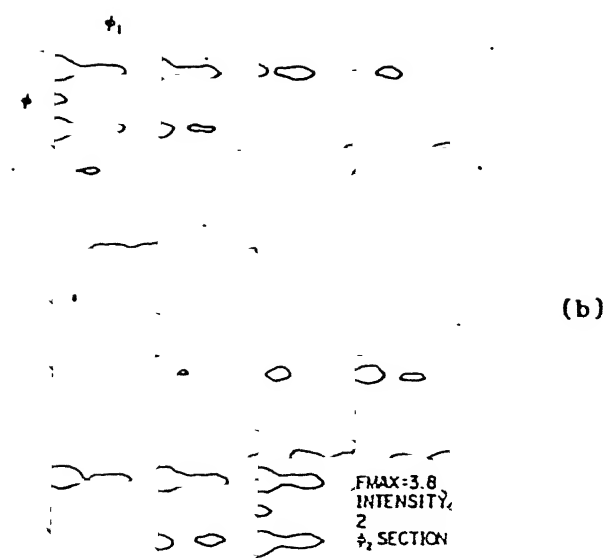
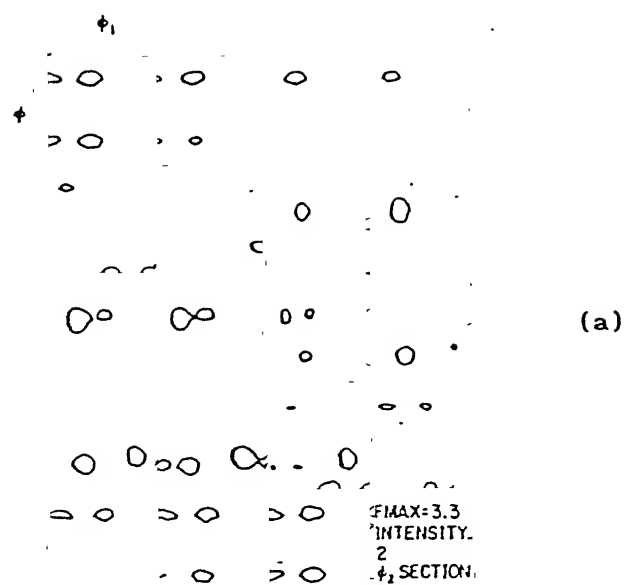


Fig.2.26: ODF of boron-doped Ni_3Al after annealing at:

(a) 1 hr at 650°C ; (b) 2 hrs at 700°C [70].

Recent investigations on this material by Ball and Gottstein [90] found that recrystallization started locally with very different kinetics, with the highest rate at the shear bands. The high nucleation rate in shear bands in combination with a low grain boundary mobility produced a very small recrystallized grain size. The recrystallization textures were very weak compared to the rolling textures (Fig.2.27). The discernible components were $\{025\}<100>$ and $\{011\}<100>$.

The different recrystallization parameters reported in the literature have been tabulated in Table 2.3.

2.6. Scope of the Present Investigation :

It is clear from the literature reviewed above that there are a lot of ambiguity concerning the deformation behaviour of the ordered intermetallic compound Ni_3Al . The microstructural evolution, structural changes and textural developments during cold work and subsequent annealing need to be investigated and rationalized. In the present investigation, the reasonably ductile compound, $\text{Ni}_{76}\text{Al}_{24}$ + 0.24 at.% Boron was subjected to cold rolling followed by recrystallization. The evolution of structure along with texture is carefully studied and their correlations have been depicted and discussed in the following chapters.



Fig.2.27: ODF of $\text{Ni}_3\text{Al(B)}$ after annealing for 30 min. at 750°C [90].

Table 2.3 : Comparison of the Parameters of the Recrystallization Kinetics Reported in the Literature

% Deformation	Temperature Range °C	Q kJ/mol	n	Reference
16.7% Comp.	850 - 1000	487.7	--	88
22% CR	925 - 975	189.3	1.69	89
25% CR	850 - 900	172.6	1.74	89
30% CR	850 - 925	118 - 146	2.26	89
40% CR	850 - 1000	301	1.0	88
59% CR *	750 - 900	331	--	19
80% CR	650	120	2.3	70
	675	120	2.1	70

CR : Cold Rolled; Comp. : Compression; * : Single Crystal.

CHAPTER III

EXPERIMENTAL PROCEDURE

3.1. Alloy Preparation :

A hypostoichiometric alloy of composition $\text{Ni}_{76}\text{Al}_{24}$ + 0.24 at.% boron was selected for the present investigation, as this alloy composition is reported [2] to have excellent ductility (approx. 50%). This alloy is also designated as IC 15 by the Oak Ridge National Laboratory, USA. The alloy was prepared by arc melting with a non-consumable tungsten electrode. The cast alloy was homogenized for 1 hour at 1050°C under high vacuum ($<10^{-6}$ torr) and cold forged to a strain of 35% at room temperature. These cold forged samples were sealed in quartz tubes under a vacuum of 10^{-6} torr and annealed at 1050°C for 20 minutes to yield an initial grain size of 25-30 μm .

3.2. Cold Rolling :

Plates of 4.5 mm thickness and 10 mm width were cut from the homogenized alloy. The edges of the cut-plates were smoothened by grinding. These plates were then cold rolled at room temperature for different degrees of reduction ranging from 15% to 90%. Cold rolling was carried out in a two high laboratory rolling mill having 150 mm dia rolls. The thickness reduction was 5% at each pass. Edge cracks were detected after 40% cold rolling; however, the length of the cracks were limited within the micron range. The cracks propagated only after 90% cold rolling.

3.3 Annealing :

Deformed samples were trimmed from the sides to remove the cracked edges. Since the cracks were quite extensive after 90% cold rolling, recrystallization behaviour was investigated on the 85% deformed samples.

Isochronal annealing was carried out at temperatures ranging from 100° to 1000°C at 100°C intervals. Recrystallization characteristics were studied at temperatures in the range of 800° to 950°C. All heat treatments were performed with samples sealed in quartz tube under high vacuum ($<10^{-6}$ torr) in a vertical tubular furnace using a Proportional temperature controller to maintain the temperature within $\pm 2^\circ\text{C}$.

At each stage of recrystallization annealing, the volume fraction of recrystallization was measured by point counting. Approximately 20 -25 areas were examined for each specimen using a 21 x 21 square grid.

3.4. X-ray Diffraction :

X-ray diffraction was carried out for lattice parameter as well as order parameter measurements. For lattice parameter measurement, powders of $\text{Ni}_{76}\text{Al}_{24}(\text{B})$ were used. For some experiments rolled sheets were also taken. Powders were prepared by filing the sheet specimen with a jeweller's diamond file. Before filing, the surface of the sample was cleaned by grinding to remove any surface contamination. For the homogenized sample, powder was sealed in a quartz tube under vacuum ($<10^{-6}$ torr) and annealed at 1050°C for 15 minutes for stress-relieving.

An Iso-Debyelex 2002 X-ray diffractometer with copper target was used. The diffraction patterns were recorded on a strip chart recorder. Initially rapid scan was done from $20^\circ - 150^\circ$ (2θ values) to ascertain the peak positions and then slow scan was made to measure precisely the 2θ value for the corresponding peak. Conditions under which the diffraction patterns were obtained were as follows :

Rapid Scanning :

Voltage	30 kV
Current	20 mA

Scanning Speed	3°/min (in 2θ)
Chart Speed	3 cm/min.
Time Constant	10 sec.
Counts per second	10 K

Slow Scanning :

Scanning Speed	0.3°/min.
Chart Speed	0.6 cm/min.
Time Constant	10 sec.
Counts per second	Varied according to the peak intensities.

In order to determine the instrumental error in the machine, a standard silicon sample was scanned at slow speed. The deviation (theoretical value - experimental value) of the recorded peak position from the theoretical value calculated from the lattice parameter of silicon was the amount of error. This error factor was added to the recorded peak angles to get the exact angular positions of the peaks. These corrected angles were later used in calculating the precise lattice parameter of the alloy using the Nelson-Riley extrapolation technique and the least square regression method.

The order parameter (S) was calculated from the integrated intensity ratios of the (100)/(200) and (110)/(220) pairs of reflections. The used relationship between S and the above intensity ratios is as follows [91] :

$$S^2 = \frac{I_s}{I_f} \cdot \frac{(x_{Al}f_{Al} + x_{Ni}f_{Ni})^2}{(f_{Ni} - f_{Al})^2} \cdot \frac{(L_p)_f (e^{-2M})_f}{(L_p)_s (e^{-2M})_s}$$

Here, I is the measured integrated intensity (scatter is $\pm 1\%$); x_{Al} and x_{Ni} are the atomic fractions of Al and Ni, respectively; f_{Al} and f_{Ni} are the atomic scattering factors for Al and Ni, respectively; L_p is the Lorentz-Polarization factor; and e^{-2M} is the Debye-Waller factor. The subscripts s and f refer to the superlattice and fundamental reflections, respectively.

3.5. Texture Representation and Determination :

Texture in a rolled polycrystalline sheet metal is frequently represented as being of the type $\{hkl\}\langle uvw \rangle$, where $\{hkl\}$ is the crystallographic plane of the grains which lie parallel to the rolling plane and $\langle uvw \rangle$ the direction that lies parallel to the rolling direction. However, if the texture is more complex, it is possible to describe it as consisting of a number of components of different severity.

Generally, texture is represented in the form of pole figures [92]. Although pole figures are useful to describe the texture present in a material, these are only qualitative or at best semiquantitative in nature. A more thorough and quantitative description of texture can be given in terms of the orientation distribution function or ODF.

An ODF gives the distribution of specific orientations present in a sample. It describes the frequency of occurrence of orientations in the three-dimensional (Euler) orientation space. This space is defined by three Euler angles, ϕ_1 , ϕ , ϕ_2 . The Euler space constitutes a set of three consecutive rotations that bring the crystallographic $\langle 100 \rangle$ axes of each crystallite into coincidence with the specimen axes. The orientation of each crystallite can thus be represented by a point in the three dimensional Euler Orientation space. Mathematical models [93, 94] are available for calculating ODF from several experimentally determined pole figures. The most widely adopted methods are those proposed independently by Bunge [93] and Roe [94], who used generalized spherical harmonic functions to represent the crystallite distributions. A thorough mathematical treatment of the subject can be found in two books by Bunge [95, 96]. The Bunge notation [93] is the more common among the two and this has been used all throughout in the present investigation.

For cubic crystal symmetry, a three-dimensional orientation volume may

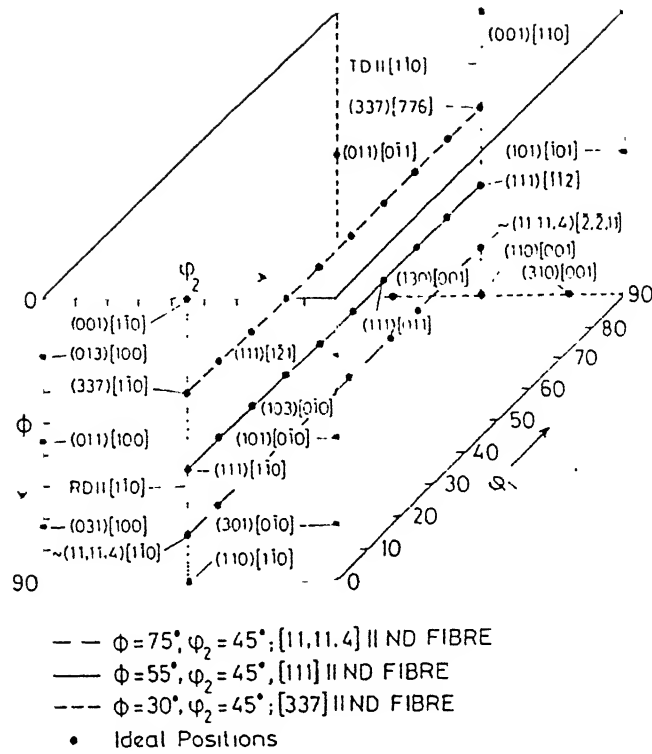


Fig.3.1 : Three dimensional Euler space showing locations of ideal orientations.

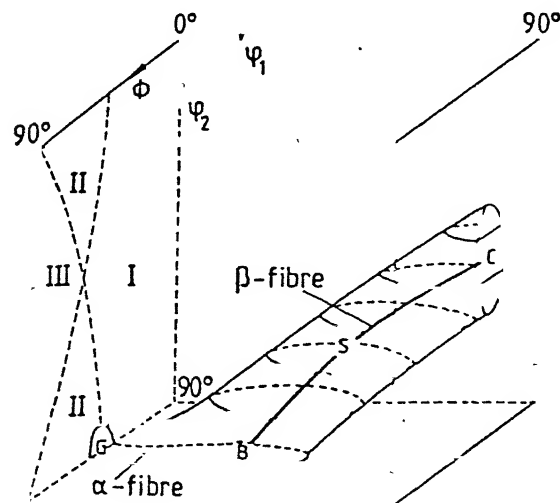


Fig.3.2 : Schematic presentation of the FCC rolling texture in the first subspace of three dimensional Euler angle space [97].

orientation density $f(g)$, obtained by the above mentioned procedure, was represented as functions of orientations given by $g(\phi_1, \phi, \phi_2)$ in the form of contour lines in sections $\phi_2 = \text{constant}$. For ODF calculation, the data were generated from four pole figures i.e. (111), (200), (220) and (311) using Cu-K α radiation. From these data, the ODF was determined by means of series expansion to an order of $l = 22$. For each specimen, the texture measurements were done at one-quarter thickness from one of the free surfaces. Later, for several of the samples texture measurements were done at the mid-section level also and it was ascertained, therefore, that there was no textural difference between the quarter and the mid-section planes.

3.6. Optical and Scanning Electron Microscopy :

The rolled and recrystallized specimens were cold mounted, polished and etched. The etching reagent used was alcoholic ferric chloride having the following composition :

Anhydrous Ferric Chloride	5 gm.
Concentrated HCl	2 ml.
Ethanol	96 ml.

Scanning electron microscopy was carried out in JSM 840A JEOL SEM which had an EDAX facility attached to it.

3.7. Transmission Electron Microscopy :

The rolled as well as annealed samples were thinned down to 0.05 mm by mechanical grinding on fine waterproof emery papers. Discs of size 3 mm were punched out of the thin sheets and were further thinned in a Fishione twin jet polisher. The conditions used were :

Electrolyte	10% H ₂ SO ₄ and 90% methanol
Temperature	- 3°C

Voltage

10 V

TEM studies were carried out on the rolling plane section at 160 kV in a JEOL 2000 FXII machine in the bright field conditions.

3.8. Microhardness and Resistivity :

Hardness values of cold rolled as well as annealed samples were measured using a Vicker's hardness tester. The load used was 25 gm. An average of at least ten measurements was used as the correct hardness value (scatter $\pm 3\%$).

The most commonly used technique for measuring resistivity is the 'four-point probe method'. This method is nondestructive, speedy and does not involve any elaborate specimen preparation. This method was used in the present investigation. Four equally spaced metal probes were pressed on to the material surface. The probes were set parallel to each other on a sheet specimen with spacing of about 3 mm between the probes.

If the ratio of the material thickness (X) to the probe spacing (S) is less than 0.4, then the average resistivity of an infinitely thin sample in which the current flow is parallel to the surface is [99] :

$$\rho = \frac{\pi}{\log_e 2} \cdot \frac{V}{I} \cdot X = 4.532 \cdot \frac{V}{I} \cdot X$$

Here, I is the current flowing between the outer probes and the voltage (V) is measured across the inner probes. This ρ is called 'Sheet Resistivity'. It is not affected by the geometrical shape of the material. The resistivity values are within the range of $\pm 0.01\%$ and the experiments are carried out for several times for reproducibility.

3.9. Differential Scanning Calorimetry :

Differential Scanning Calorimetry (DSC) has been used in order to gain an insight into the kinetics of the transformation processes in the present

alloy. When a specimen and a reference material are heated in a DSC at a known heating rate, the heat inputs to the specimen and the reference remain almost the same unless a heat related transformation takes place in the specimen. The rate of heat input to the specimen relative to the reference is directly related to the amount of the transformation product in the specimen. Therefore, the kinetics of transformation can be estimated from the DSC runs.

The DSC operation was carried out in a Stanton Redcroft DSC 1500 machine. In this equipment, both the reference and the sample have the same thermal environment and the thermal resistances between the sample and the environment and the reference and the environment are identical.

The specimens were loaded in the DSC cell at room temperature and equilibrated for a few minutes. High purity argon gas was passed through the cell to avoid oxidation. The reference used was well annealed platinum and the sample was cold rolled boron-doped $\text{Ni}_{76}\text{Al}_{24}$ alloy. The weights of the samples were chosen such that the heat capacities were approximately same. Heating rates of 15° , 20° and 25°C/min were used. Two specimens were used for each heat treatment and the results obtained were found to be highly reproducible. The output was in mcal/sec. The net heat flow to the reference relative to the sample was recorded as a function of temperature. From this plot, volume fraction of the transformed product and the activation energy for the transformation were evaluated.

CHAPTER IV

COLD ROLLING CHARACTERISTICS

4.1. Microstructure :

The microstructure of homogenized $\text{Ni}_{76}\text{Al}_{24}$ (B) alloy shows the presence of a single phase (Fig.4.1). The X-ray diffraction pattern contains the peaks due to Ni_3Al only. The lattice parameter of this alloy is 3.569\AA . EDAX analysis carried out at several spots on the homogenized samples yielded consistent results and confirmed that the composition was $\text{Ni}_{76}\text{Al}_{24}$ and that the sample was homogeneous.

Cold rolling of the homogenized material produced edge cracks. These were monitored optically. Cracks were first detected after about 40% cold deformation (Fig.4.2). However, they were present within micron range. The cracks started to propagate fast and led to failure of the specimen only after 90% cold rolling.

The starting material had a grain size of $25\text{--}30\text{ }\mu\text{m}$. With the progress of cold rolling, the grains become flattened and elongated. Slip bands are observed after 25% cold rolling (Fig.4.3). Shear bands start to develop after 65% cold rolling. The frequency of these bands increases with increase in the degree of cold rolling (Fig.4.4). The shear bands make an angle of about 32° to the rolling plane (Fig.4.4 (c)).

TEM examination reveals that at low degree of deformation (45%), the structure consists of a large number of more or less straight dislocation lines (Fig.4.5). Fig.4.6 (a), (b) and (c) show the TEM micrographs of the alloy deformed to the extent of 45%, 65% and 85%, respectively. After 45% deformation, a cellular substructure develops (Fig.4.6a), whereas after 65% deformation, microbands appear with small orientation changes between neighbouring bands and the dislocation density increases appreciably. The

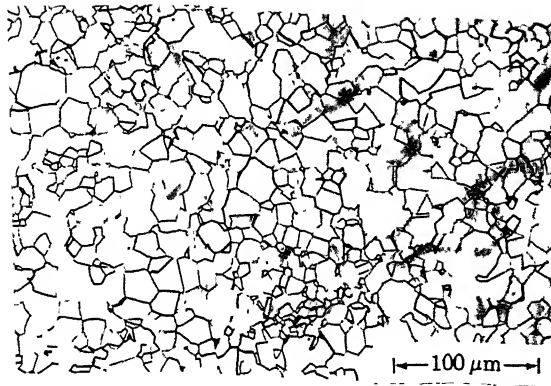


Fig.4.1 : Optical micrograph of homogenized boron-doped Ni₇₆Al₂₄ alloy.

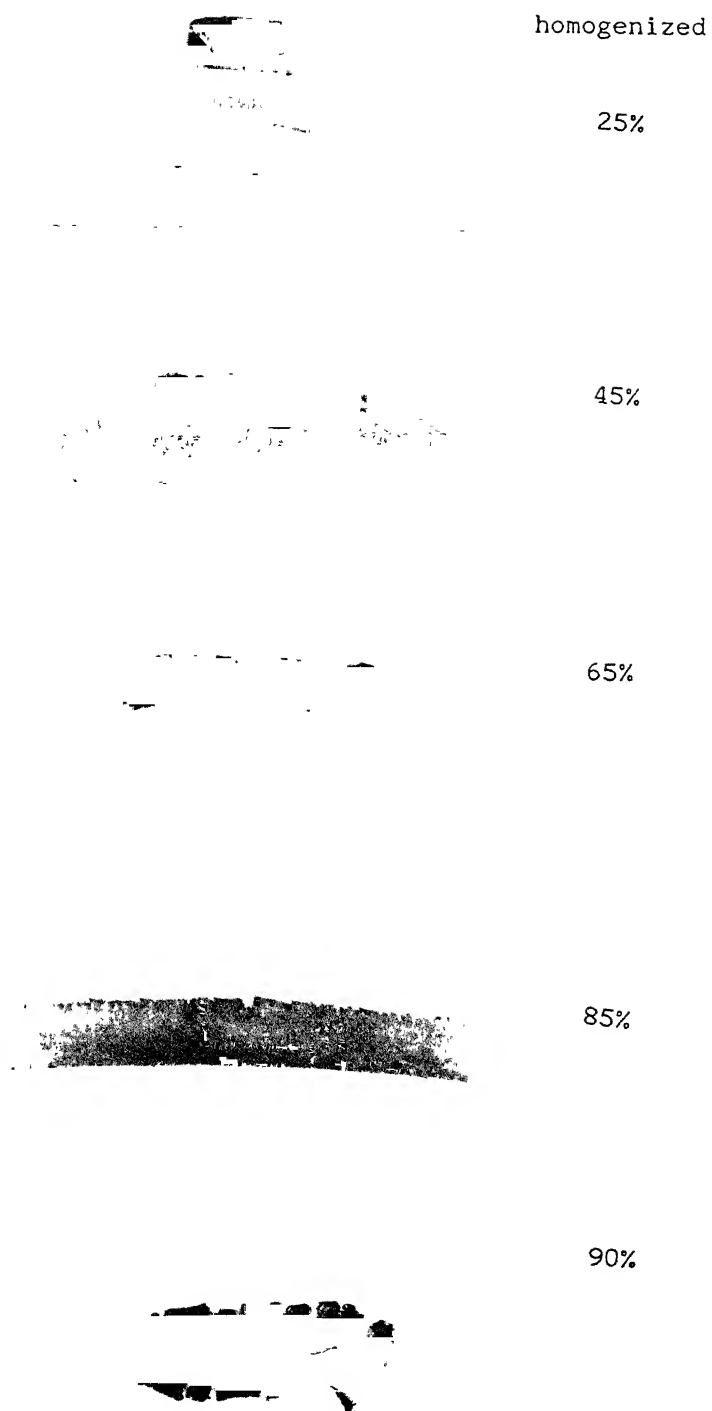


Fig.4.2 : Effect of cold rolling on crack nucleation and propagation in the present alloy.

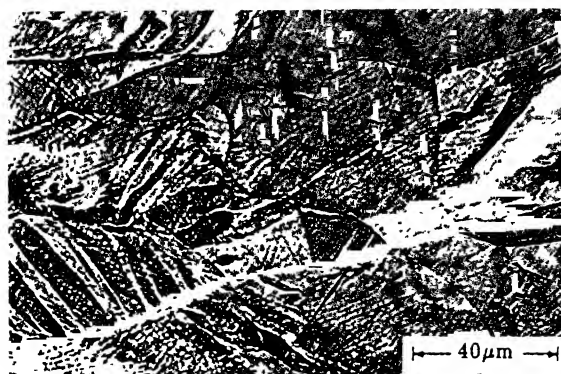
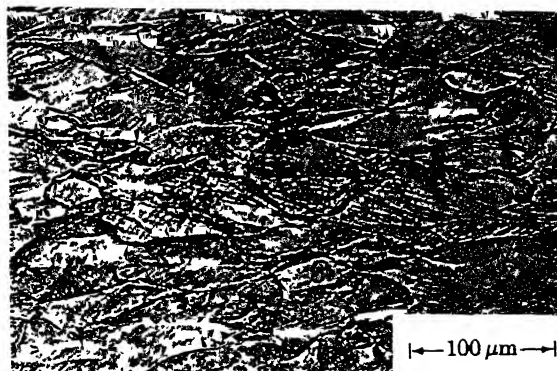
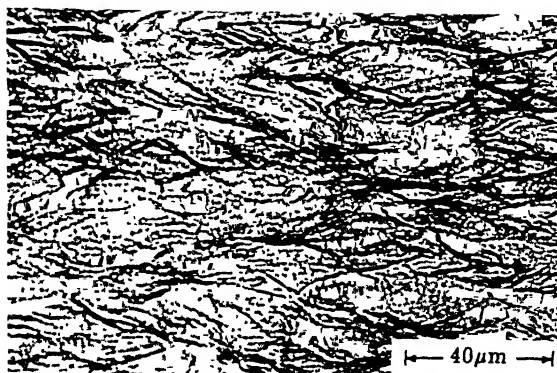


Fig.4.3 : Optical micrograph of longitudinal section after 25% cold rolling (RD parallel to the markers).



a



b



c

Fig.4.4 : Optical micrographs of longitudinal sections of (a) 45%, (b) 65% and (c) 85% cold rolled $\text{Ni}_{76}\text{Al}_{24}(\text{B})$ alloy (markers parallel to RD).

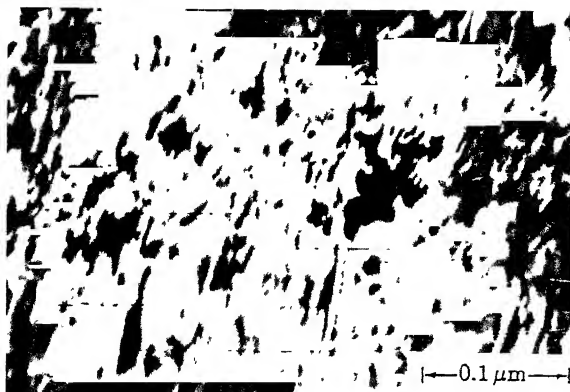


Fig.4.5 : TEM micrograph showing straight dislocation on the rolling plane section of 45% cold rolled $\text{Ni}_{76}\text{Al}_{24}(\text{B})$ (Markers parallel to RD).



Fig.4.6 : TEM micrographs of the rolling plane sections of (a) 45%, (b) 65% and (c) 85% cold rolled $\text{Ni}_{76}\text{Al}_{24}(\text{B})$ (Markers parallel to RD).

microstructure of the 85% deformed sample shows large scale twinning and numerous microbands across it (Figs.4.6c and 4.7).

4.2. Texture :

4.2.1. Development of texture :

The (111) pole figures for the 25%, 45%, 65% and 85% cold rolled specimens are presented in the Figs.4.8 (a) to (d), respectively. After 25% cold deformation, a weak texture develops (Fig.4.8a) which later strengthens significantly (more than 3 times) after 45% cold work (Fig.4.8b). The texture at this stage is of pure metal type. There is a distinct change in the texture after 65% deformation and the texture here appears to be mixed type, containing features similar to both pure metal and alloy type textures. After 85% cold work, the (111) pole figure shows alloy type texture. Thus, increasing amount of cold work appears to produce a texture transition in $\text{Ni}_{76}\text{Al}_{24}(\text{B})$ alloy. In order to bring out the textural differences more clearly, ODFs taken from the cold rolled samples were carefully examined. Fig.4.9 (a) to (d) show the ODF's of the 25%, 45%, 65% and 85% cold rolled materials, respectively. The gradual development of a pure metal type texture is apparent from a deformation level as low as 25%. The important texture components in this case are Cu {112}<111>, B_s {110}<112>, S {123}<634> and Goss {011}<100>, the locations of which have been marked at the appropriate places in the ODFs. The ODF of the 45% cold rolled material shows fully developed pure metal type texture. The intensities of the texture components show significant increase as compared to the ODF's of the 25% deformed material. The overall sharpness of the texture decreases after 65% deformation. After 85% deformation, the ODF shows a distinct alloy type texture. The texture at this stage is characterized by sharp intensity at the B_s position and drastic decrease of intensity at the Cu position.

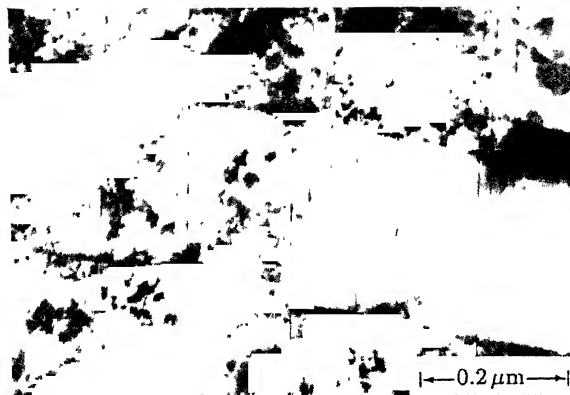


Fig.4.7 : TEM micrograph showing twins in 85% cold rolled boron-doped

Ni₇₆Al₂₄ (Markers parallel to RD).

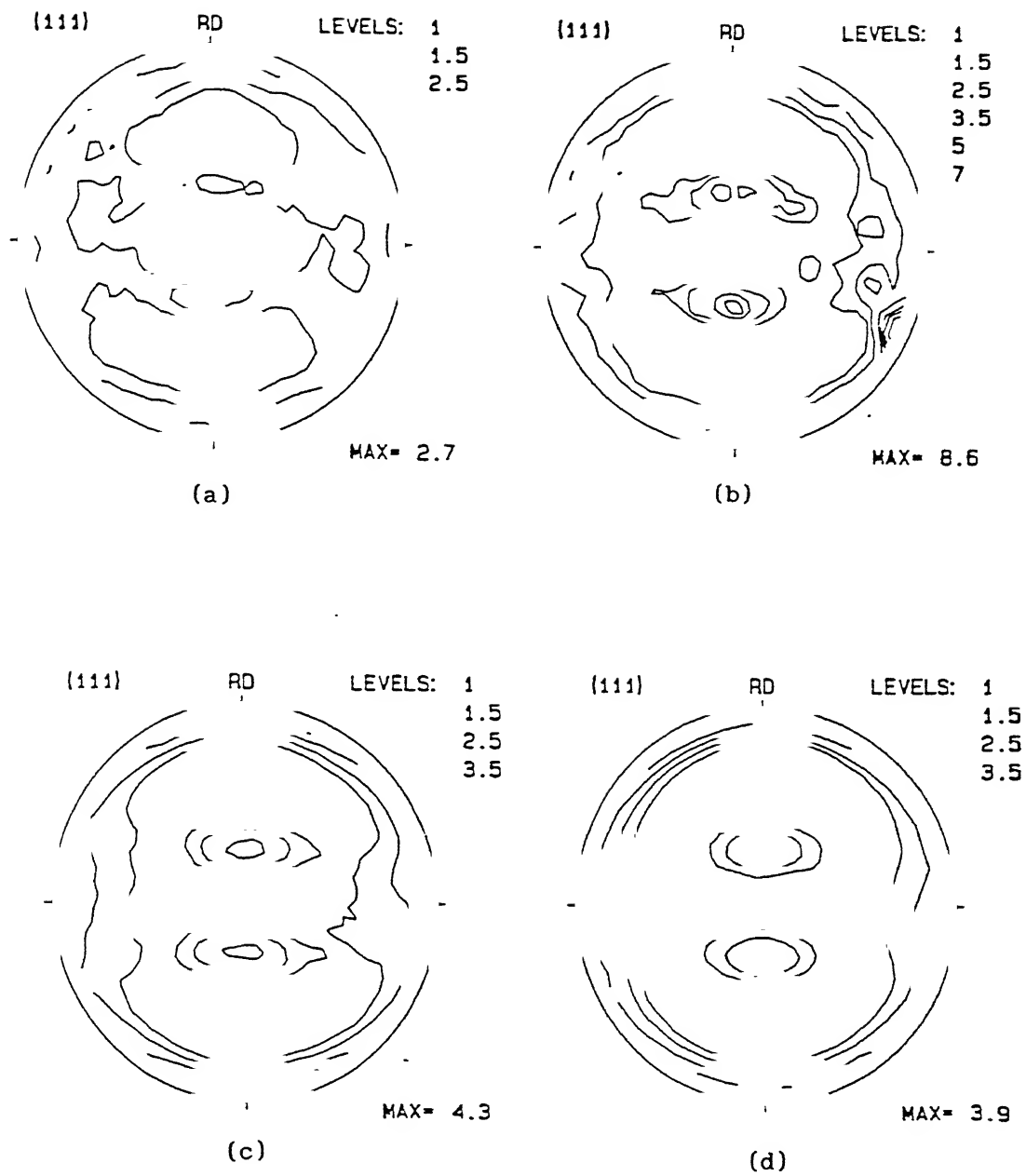


Fig.4.8 : (111) pole figures of (a) 25%, (b) 45%, (c) 65% and (d) 85% cold rolled $\text{Ni}_{76}\text{Al}_{24}(\text{B})$.

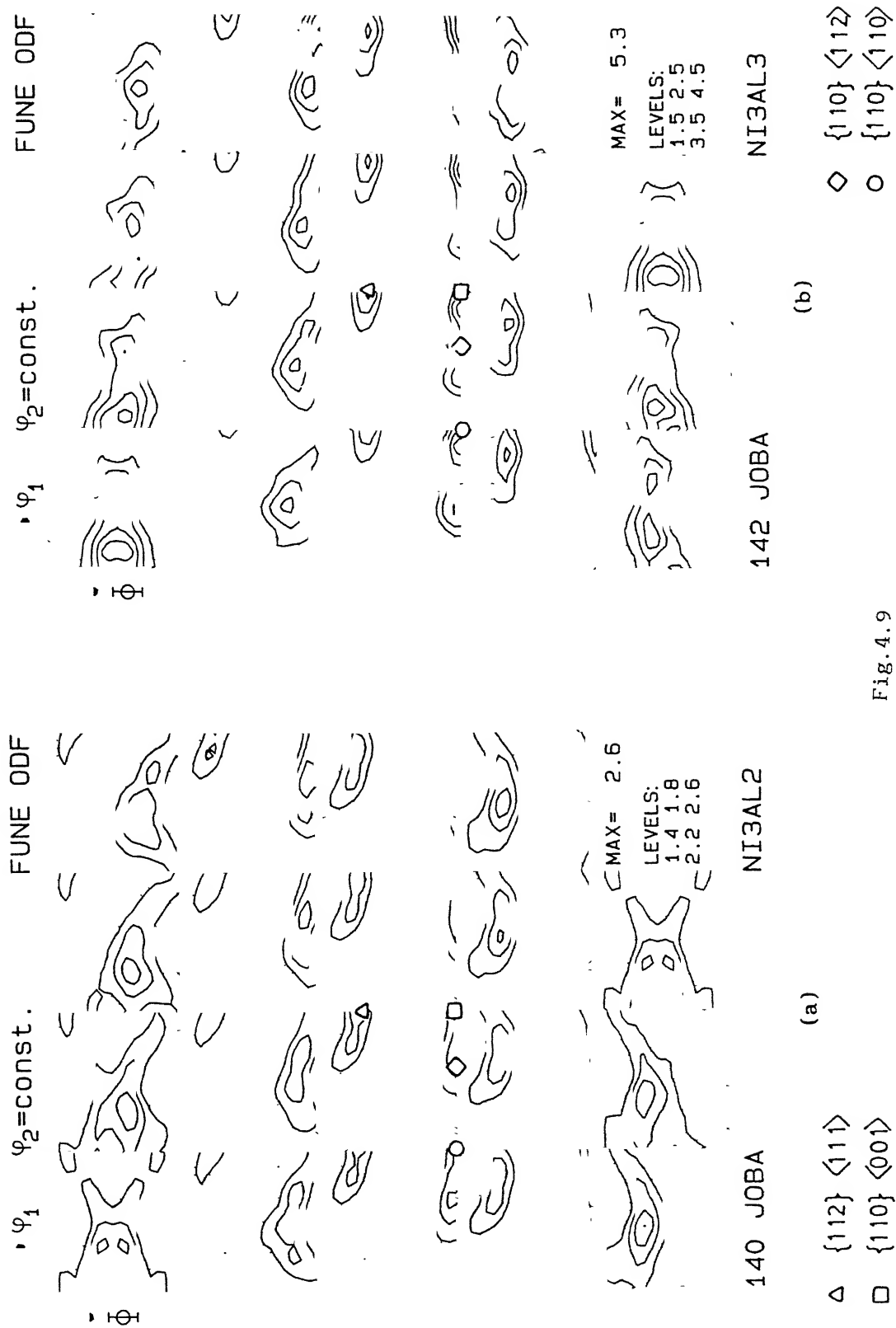


Fig. 4.9

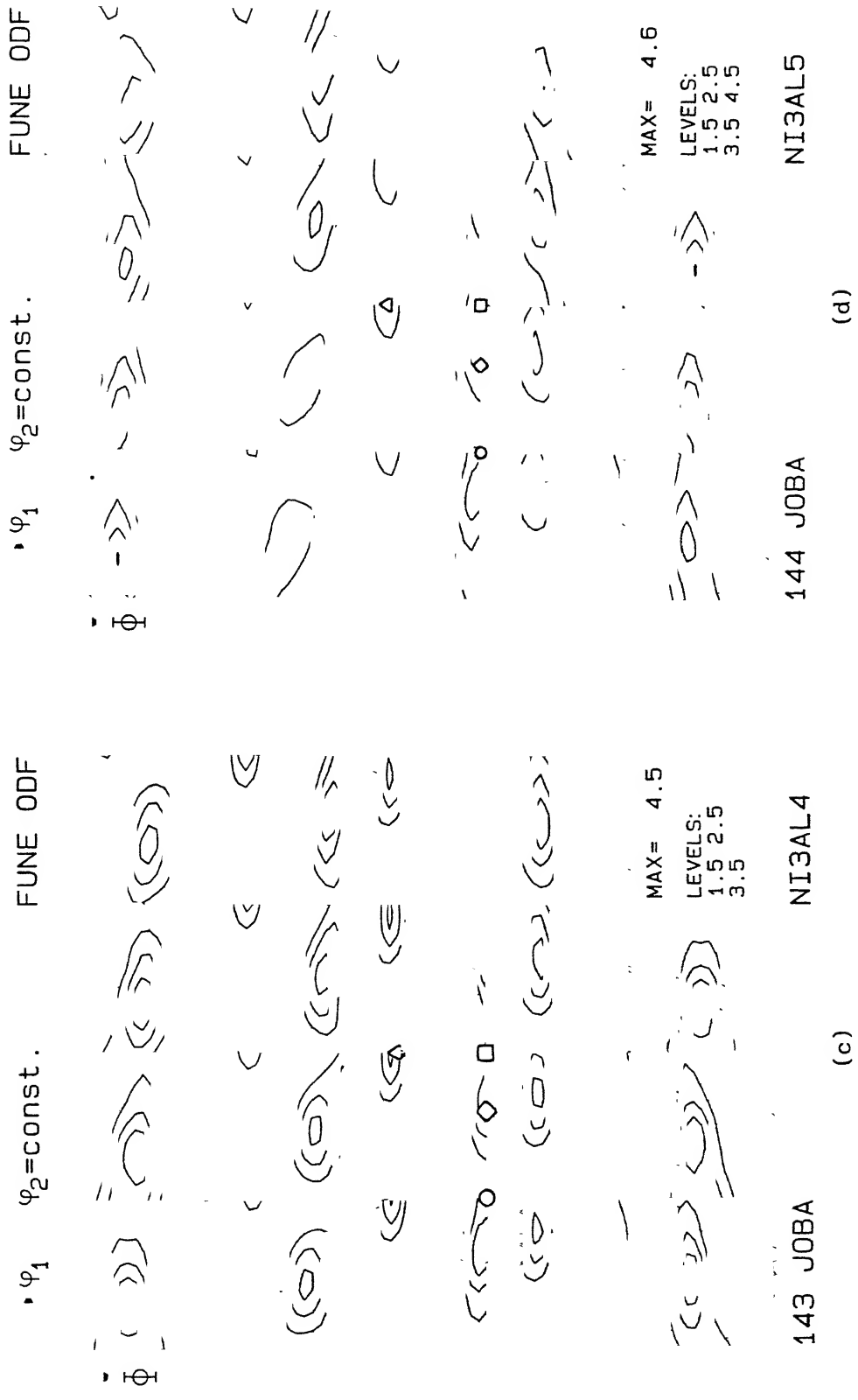


Fig.4.9 : ODFs of (a) 25%, (b) 45%, (c) 65% and (d) 85% cold rolled

Ni₇₆Al₂₄(B) at constant ϕ_2 sections.

In order to bring out the differences between the above ODFs in a more quantitative manner, the variations in orientation density, $f(g)$ in the three dimensional orientation space are plotted in the form of fibers such as α , β and τ [98]. The α -fiber extends from the Goss orientation $\{011\}\langle 100 \rangle$ through the B_s orientation $\{110\}\langle 112 \rangle$ to the rotated Goss orientation $\{011\}\langle 110 \rangle$. In this, the $f(g)$ values at $\phi = 45^\circ$ in the section $\phi_2 = 0^\circ$ are plotted against ϕ_1 . This plot, for different degrees of cold rolling, is shown in Fig.4.10. The β -fiber runs from the Cu position $\{112\}\langle 111 \rangle$ through the S orientation $\{123\}\langle 634 \rangle$ to meet the α -fiber at the B_s position. It is plotted in Fig.4.11 which shows the variations of the maximum intensities in different ϕ_2 sections against ϕ_2 . Furthermore, the exact course of the β -fiber in the orientation space is given in Fig.4.12 where the positions (ϕ_1, ϕ) of the maxima of orientation density $f(g)$ in different ϕ_2 sections are plotted against ϕ_2 . The τ -fiber extends from $\{001\}\langle 110 \rangle$ through $\{112\}\langle 111 \rangle$ and goes upto $\{011\}\langle 100 \rangle$. Here, the variation of $f(g)$ for $\phi_1 = 90^\circ$ and $\phi_2 = 45^\circ$ is plotted against ϕ and this is shown in Fig.4.13.

At low degrees of cold rolling (25%), the intensities of all the orientations are more or less homogeneously distributed along the α and β -fibers (Fig.4.10 and 4.11). At intermediate degrees of rolling ($\sim 45\%$), the homogeneity of the fibers deteriorates. In the α -fiber, there is an increase in the intensity of the Goss orientation; in addition, other components like $\{011\}\langle 8\bar{1}1 \rangle$ at $\phi_1 = 10^\circ$, $\phi = 45^\circ$ and $\phi_2 = 0^\circ$ and $\{011\}\langle 1\bar{1}1 \rangle$ at $\phi_1 = 55^\circ$, $\phi = 45^\circ$ and $\phi_2 = 0^\circ$ appear. However, with the increase in the degree of deformation, those two components disappear. The B_s component becomes prominent after 65% cold rolling and it shifts to lower ϕ_1 side after 85% deformation. The rotated Goss component whose intensity is less than the random after 65% cold rolling, becomes markedly sharp after 85% cold deformation (Fig.4.10). The density distribution of orientations along the β

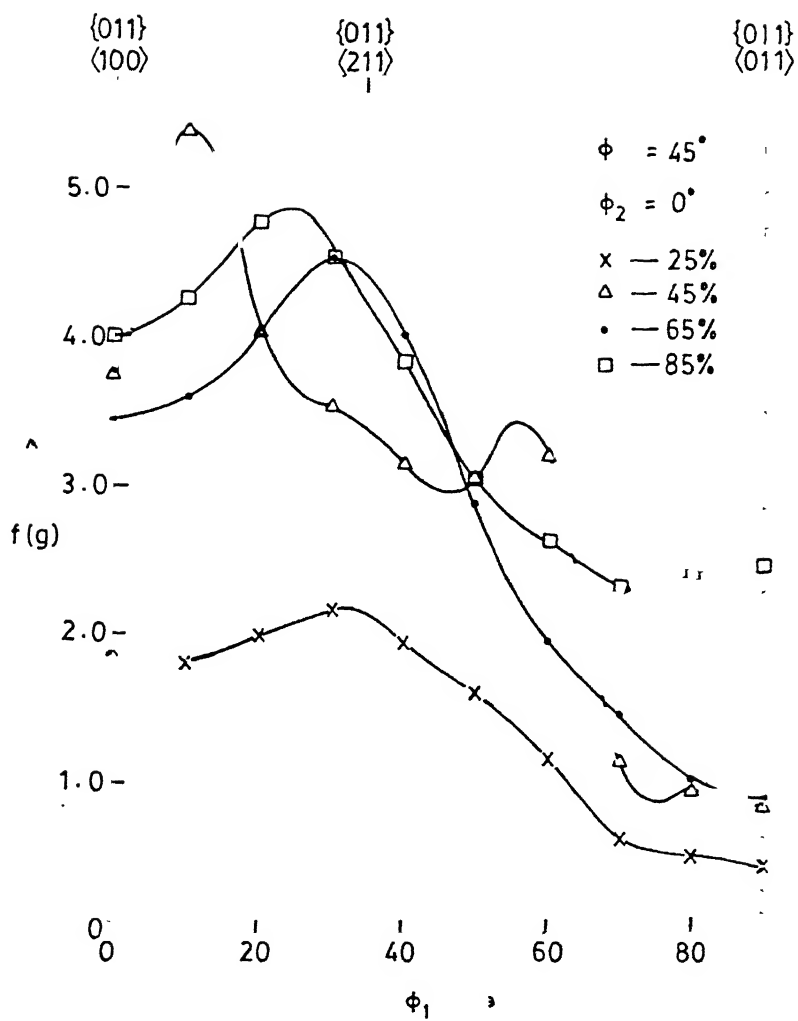


Fig.4.10 : Plot of $f(g)$ vs ϕ_1 along $\phi = 45^\circ$ and $\phi_2 = 0^\circ$ for $\text{Ni}_{76}\text{Al}_{24}(\text{B})$.

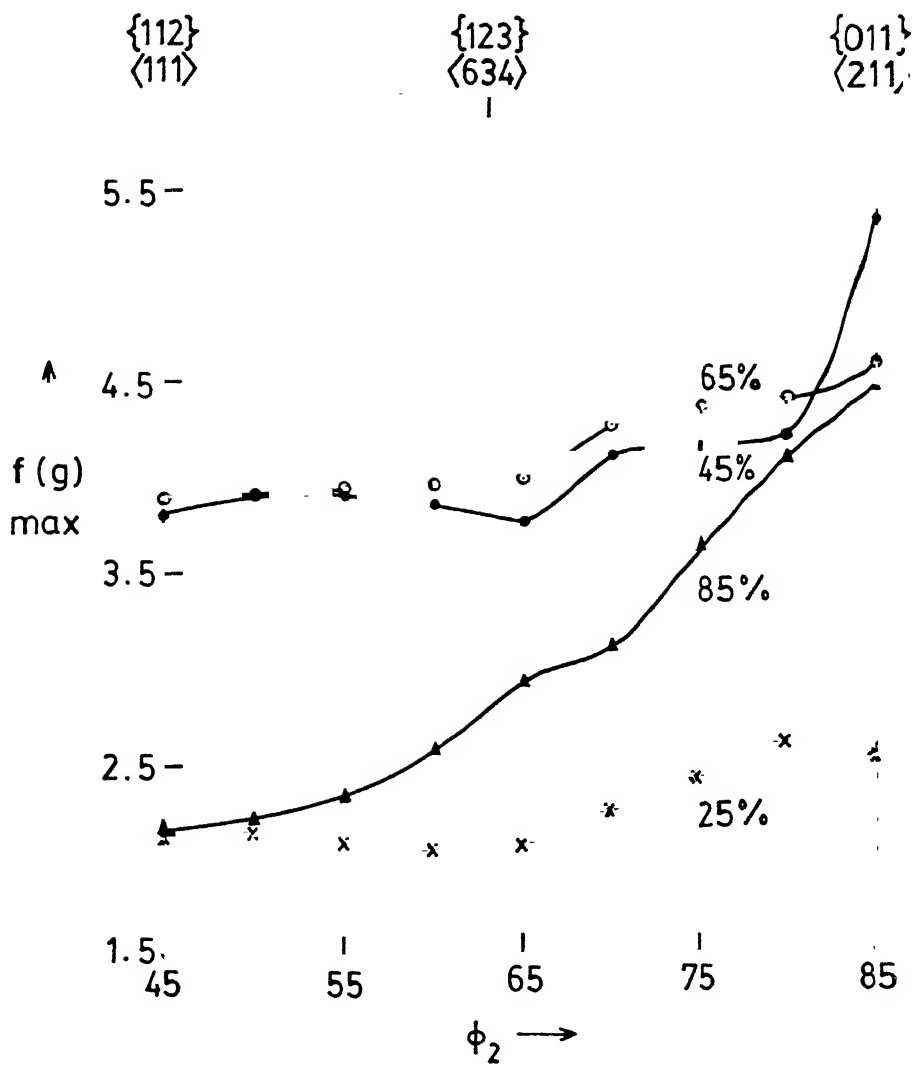


Fig.4.11 : Plot of $f(g)$ vs ϕ_2 for $\text{Ni}_{76}\text{Al}_{24}(\text{B})$.

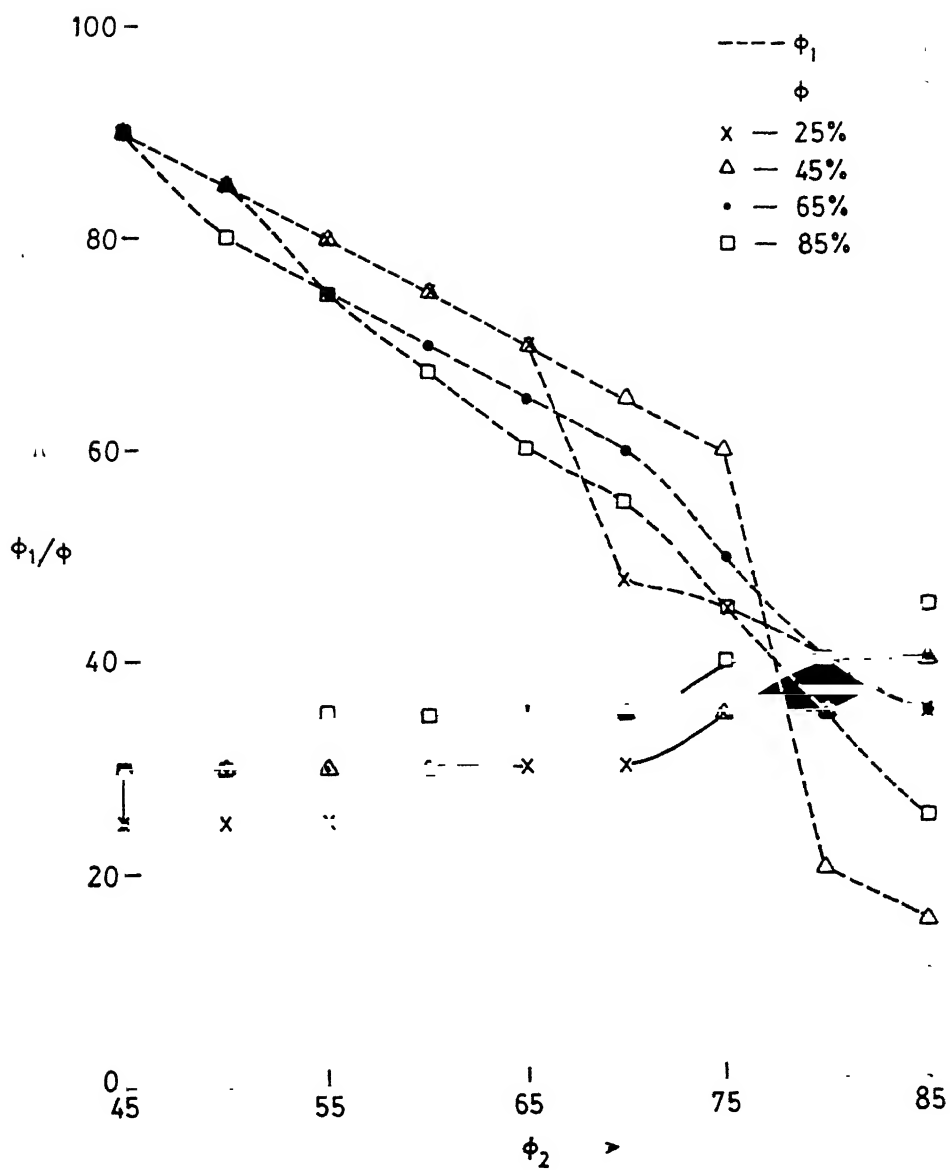


Fig.4.12 : Plot of ϕ_1/ϕ vs ϕ_2 for $\text{Ni}_{76}\text{Al}_{24}(\text{B})$.

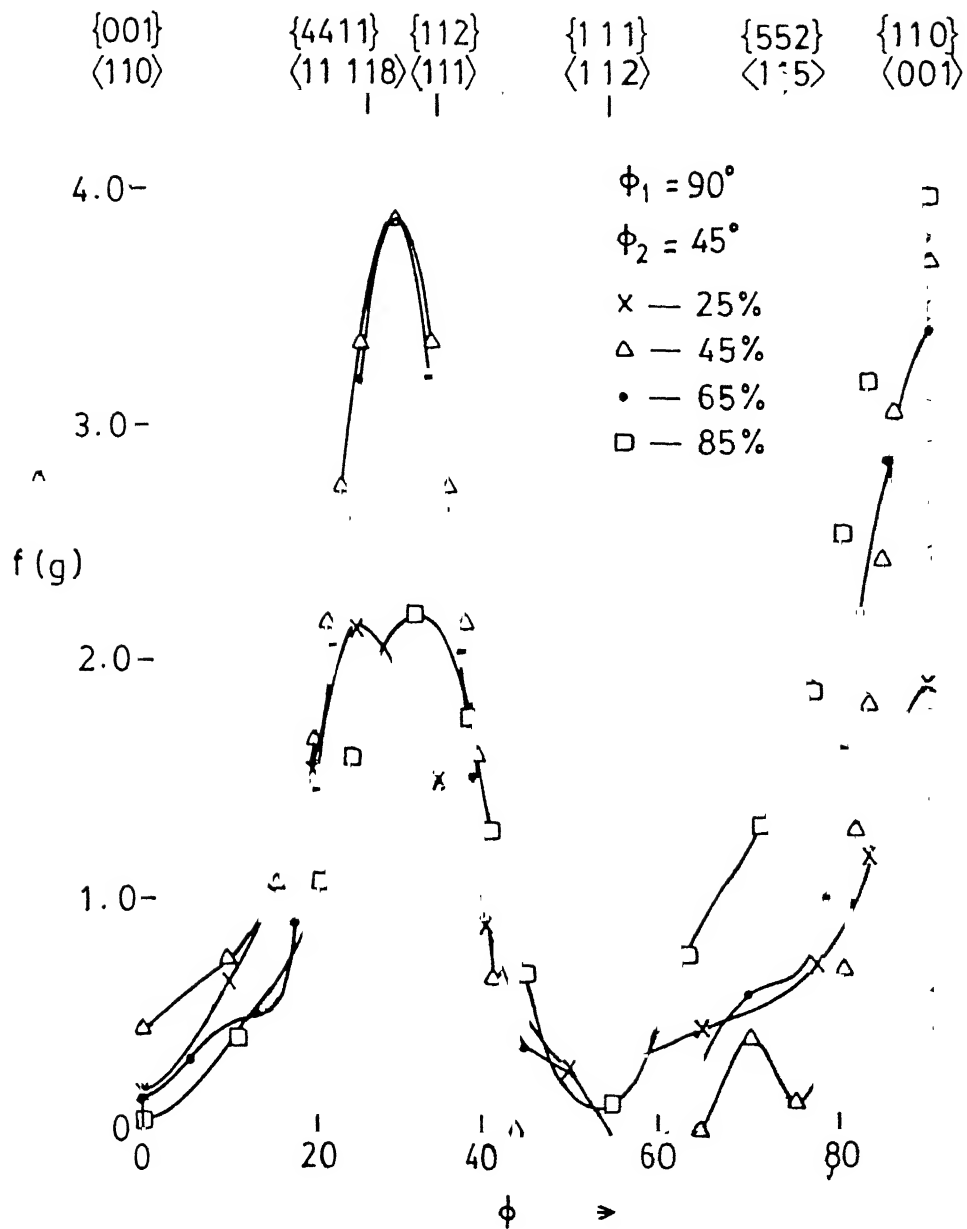


Fig.4.13 : Plot of $f(g)$ vs ϕ along $\phi_1=90^\circ$ and $\phi_2=45^\circ$ for $\text{Ni}_{76}\text{Al}_{24}(\text{B})$.

tube increases continuously with cold deformation and the homogeneity is maintained upto 65% deformation. At the highest degree of cold rolling (85%), the β tube intensity deteriorates drastically except at the B_s position, which maintains a high intensity comparable to the case of 65% deformed material (Fig.4.11). Fig.4.12 which shows the exact course of the β tube for the cold deformed samples through different ϕ_2 sections, reveals that the locations of the texture components vary substantially depending on the amount of deformation given to the material. In general, the positions of the texture components shift to lower ϕ_1 and higher ϕ values with increasing amount of cold rolling. The τ -fiber plot (Fig.4.13) shows that after 25% deformation, an orientation maxima near the ideal location $\{4\ 4\ 11\} \langle \bar{1}\bar{1}\ \bar{1}\bar{1}\ 8 \rangle$, as predicted by Dillamore and Katoh [100], is obtained. An equally strong Goss component is also present at this stage. On increasing the level of deformation the intensities of both these orientations increase till upto 65% cold rolling. The component at $\{4\ 4\ 11\} \langle \bar{1}\bar{1}\ \bar{1}\bar{1}\ 8 \rangle$ is found to shift to the Cu position $\{112\} \langle 111 \rangle$ with increased deformation level, beyond 25%. After 85% cold work, however, the Cu component drastically decreases in intensity whereas the Goss component still maintains its high intensity value. In addition, the strength of the twin Cu orientation $\{552\} \langle 115 \rangle$, which remains rather low ($< \text{random}$) upto 65% deformation, shows a perceptible increase after 85% deformation.

4.2.2. Texture Transition:

The textural changes that take place as a function of the amount of cold rolling clearly indicate that the $\text{Ni}_{76}\text{Al}_{24}(\text{B})$ undergoes a texture transition from the pure metal type to alloy type at the cold rolling level of 65% and above.

It is known that heavily cold deformed FCC metals and alloys with medium to high stacking fault energies exhibit a pure metal type texture, which is

characterized by reasonably strong Cu $\{112\}\langle 111\rangle$, B_s $\{110\}\langle 112\rangle$ and S $\{123\}\langle 634\rangle$ components. On the other hand, FCC metals and alloys of low stacking fault energies show an alloy type texture, characterized by mainly a strong B_s component [101].

The structure of $L1_2$ $Ni_{76}Al_{24}$ (B) alloy can be considered as basically of FCC type. Therefore, the development of rolling texture in this material is expected to be similar to that of pure FCC metals or alloys of comparable stacking fault energies (SFE). The stacking fault energy of a FCC metal can be written as $\nu_{SFE} \propto \mu b/x$ where ν_{SFE} is the stacking fault energy, x is the dissociation width of Shockley partials, μ is the shear modulus and b is the burgers vector. Substituting the shear modulus of Ni_3Al (80 GPa) as well as the appropriate values of x and b in the above equation, the SFE of Ni_3Al (B) is found to be comparable with the value for pure Ni (130mJ/m^2) [70]. Heavily rolled (95%) nickel shows a distinct pure metal type deformation texture; the main characteristics of which start to develop right from rather low level of deformation [102]. The present $Ni_{76}Al_{24}$ (B) alloy also shows pure metal type rolling texture upto 45% deformation. However, in contrast to the behaviour of pure Ni, the texture in $Ni_{76}Al_{24}$ (B) departs considerably from pure metal type after 65% cold rolling and assumes the typical alloy type texture, characteristic of low stacking fault energy FCC alloys. A comparison of the β -fiber plots for pure Ni at different levels of cold rolling (Fig.4.14) [102] with the corresponding plot for $Ni_{76}Al_{24}$ (B) (Fig.4.11) clearly brings out these differences.

The textural changes taking place in the present $Ni_{76}Al_{24}$ (B) alloy, as a function of the degree of cold rolling, have however been found to be very similar to those in a Ni-40wt.% Co alloy, which shows a transition from pure metal to alloy type deformation texture with increasing levels of deformation [102]. Fig.4.15 shows the β -fiber plot for this latter alloy for different

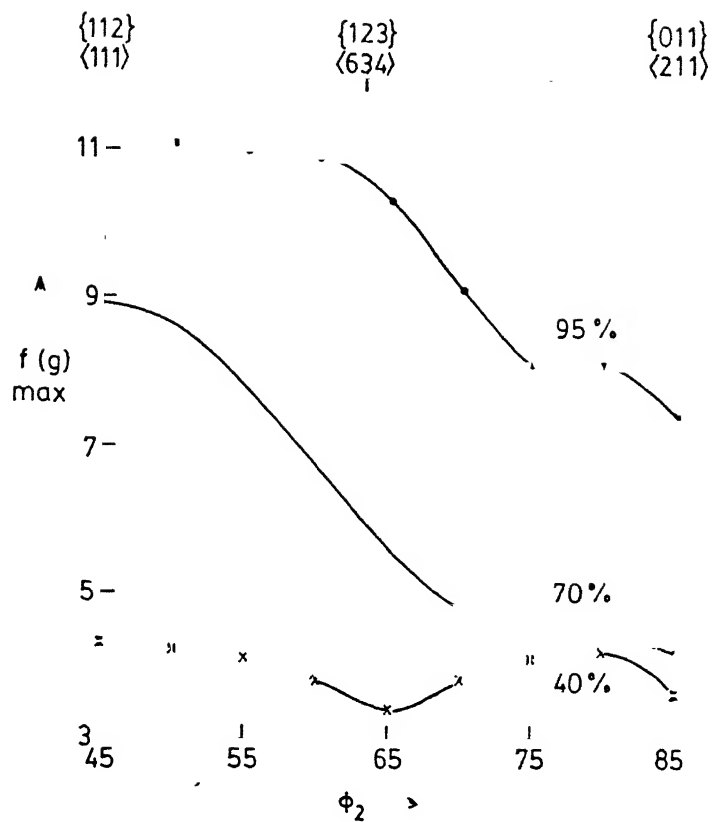


Fig. 4.14 : Plot of $f(g)$ vs ϕ_2 for Ni.

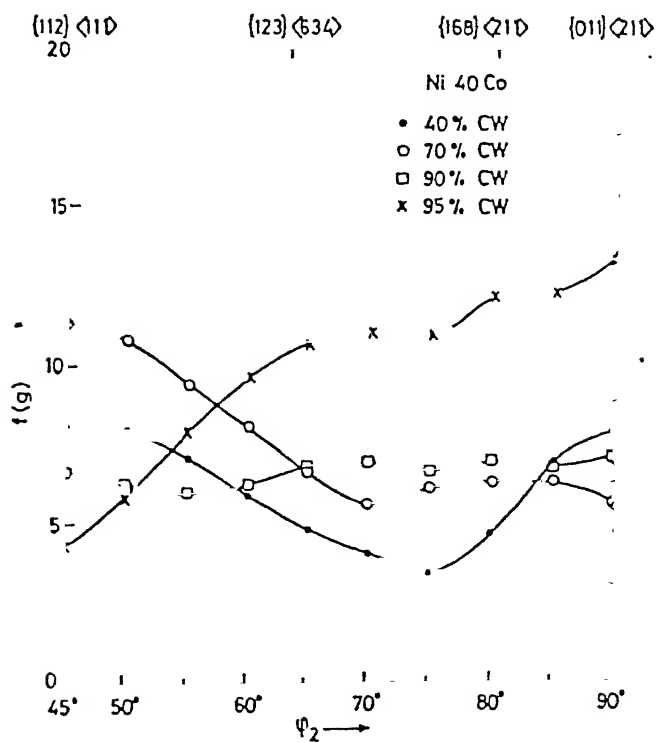


Fig. 4.15 : Plot of $f(g)$ vs ϕ_2 for Ni-40Co alloy.

levels of cold rolling. A comparison of the Fig.4.11 and Fig.4.15 clearly brings out the essential similarities in the two alloy systems.

In general, in FCC materials, the dominance of dislocation glide or deformation twinning basically determines the type of rolling texture that develops at high strains. Chin, Hosford and Mendorf [103] assumed that just as a critical shear stress exists for slip (σ_s), there is also a 'critical shear stress' for twinning (σ_t). Texture transition from pure metal to alloy type will be dependent on the magnitude of the ratio σ_t/σ_s ($= m$) [104]. For $m > 1$, deformation by slip should be promoted, whereas a value of $m < 1$ should promote deformation by twinning. In the former case, texture will be pure metal type whereas in the latter case, the texture will be of alloy type. The value of 'm' has been suggested to decrease with decrease in stacking fault energy and also with increasing rolling reduction in a particular alloy [104]. According to Wassermann [105], if mechanical twinning is an available mode of deformation, in addition to normal slip, the Cu component $\{112\}\langle 111 \rangle$ will be transformed to its twin orientation $\{552\}\langle 115 \rangle$ by twinning. Further deformation of the twin orientation will then take place on the favourable slip system which will rotate it to the Goss position $\{011\}\langle 100 \rangle$ and finally to the B_s position $\{110\}\langle 112 \rangle$ by further rotation. The B_s component $\{110\}\langle 112 \rangle$, on the other hand, is a stable one in FCC materials and will not be affected by twinning during deformation.

The observation that twins are not present in the microstructure of the $Ni_{76}Al_{24}(B)$ alloy till it is subjected to about 85% cold deformation, gives credence of the above ideas on texture transition. Further evidence to this effect is also provided by the perceptible increase in the intensity of the twin Cu $\{552\}\langle 115 \rangle$ orientation in the τ -fiber plot (Fig.4.13) after 85% cold deformation from its very low values till after 65% deformation. As mentioned in section 2.3.3., Ball and Gottstein [20] did not find twins in their TEM

investigation which was carried out on a similar alloy after 70% cold deformation. They examined the longitudinal sections whereas TEM studies in the present work was carried out on the rolling plane section.

As mentioned above, the textural changes during cold rolling of the present $\text{Ni}_{76}\text{Al}_{24}(\text{B})$ alloy have been found to be very similar to the changes encountered in a Ni - 40wt.% Co alloy. However, these two alloys have widely different stacking fault energies. While the SFE of $\text{Ni}_{76}\text{Al}_{24}(\text{B})$ alloy is $\sim 130 \text{ mJ/m}^2$ it is only $\sim 30 \text{ mJ/m}^2$ for the Ni - 40wt.%Co alloy. It is not very clear, therefore, why the deformation mode changes from slip to twinning in case of $\text{Ni}_{76}\text{Al}_{24}(\text{B})$ alloy, with increasing cold deformation, whereas slip appears to be the only deformation mode throughout in case of pure Ni. It should be remembered, however, that $\text{Ni}_{76}\text{Al}_{24}(\text{B})$ is different from pure Ni in the sense that it has a highly ordered FCC structure. There is a likelihood that the degree of order of this alloy may change with the degree of cold working and this may interfere with the deformation mode of the alloy.

4.3. Structural Changes :

4.3.1 Order Parameter :

The XRD line profiles for different degrees of cold rolling are represented in Fig.4.16. Two superlattice reflections (100), (110) and three fundamental reflections (111), (200) and (220) were considered to characterize the effect of cold rolling. The changes in the individual peak intensities for the reflections (100), (200), (110) and (220) are shown in a magnified scale in Fig.4.17(a) and (b). The order parameter (S) value was calculated as described in chapter III using the integrated intensity ratios of both (100)/(200) as well as the (110)/(220) pair of reflections. The intensities were measured on the cold rolled sheet specimens. As mentioned earlier, the material gets textured during cold rolling; hence, there is a

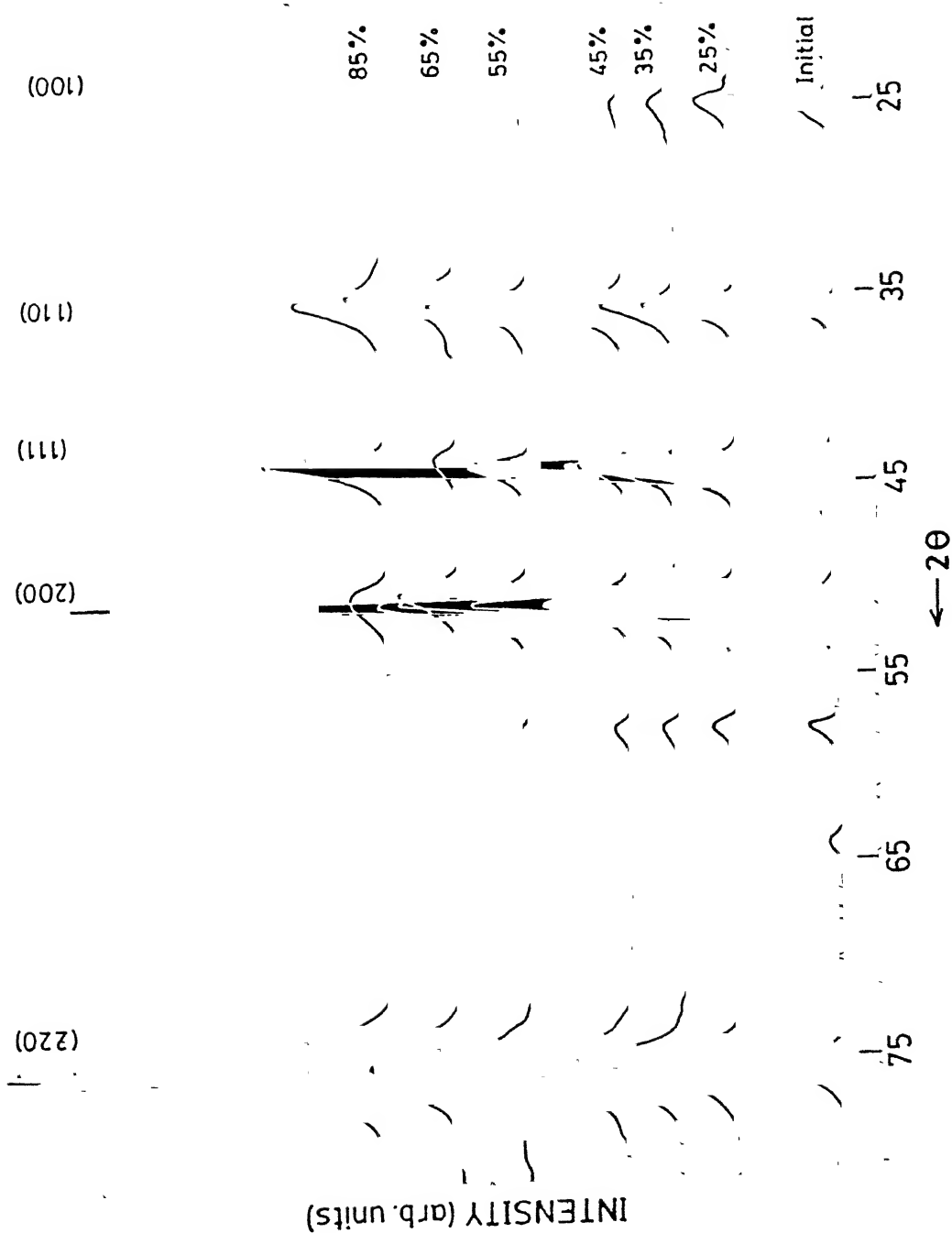


Fig.4.16 : XRD pattern for $\text{Ni}_{76}\text{Al}_{24}(\text{B})$ with various degrees of cold rolling.

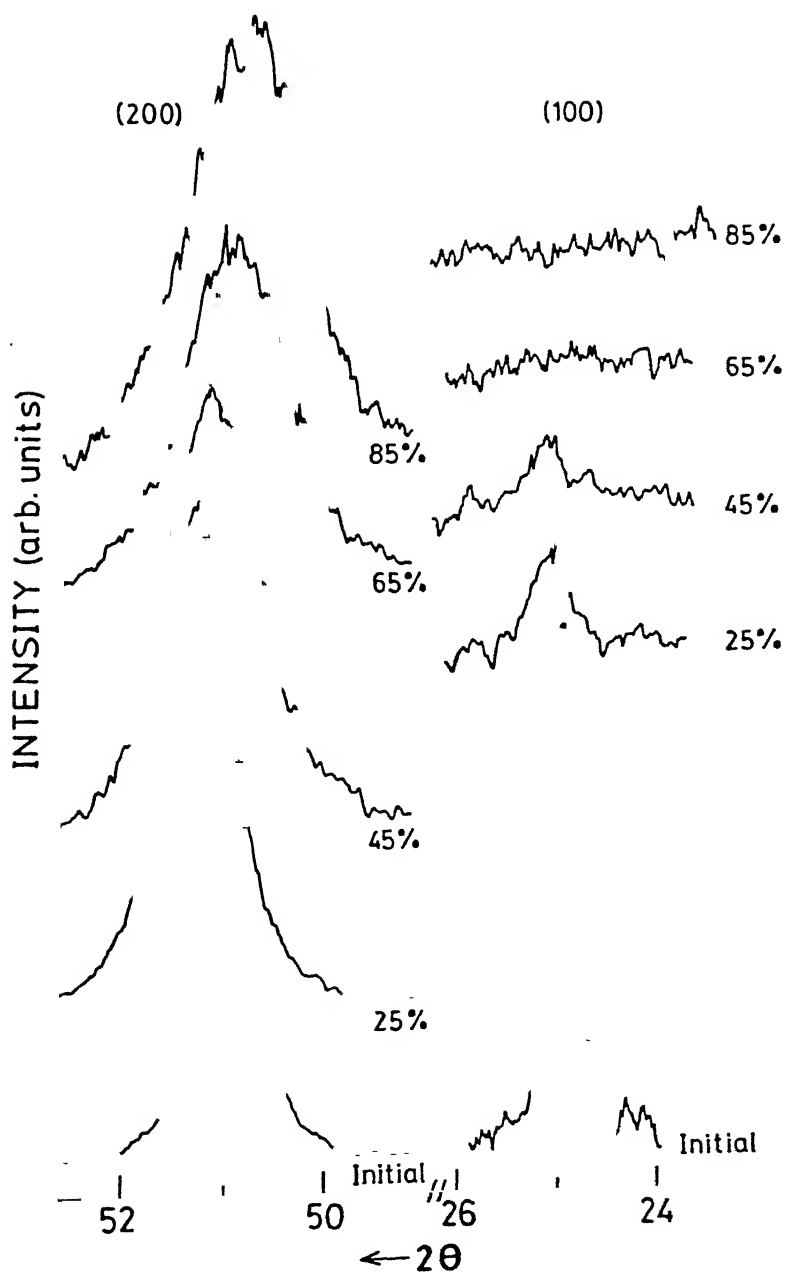


Fig. 4.17 (a)

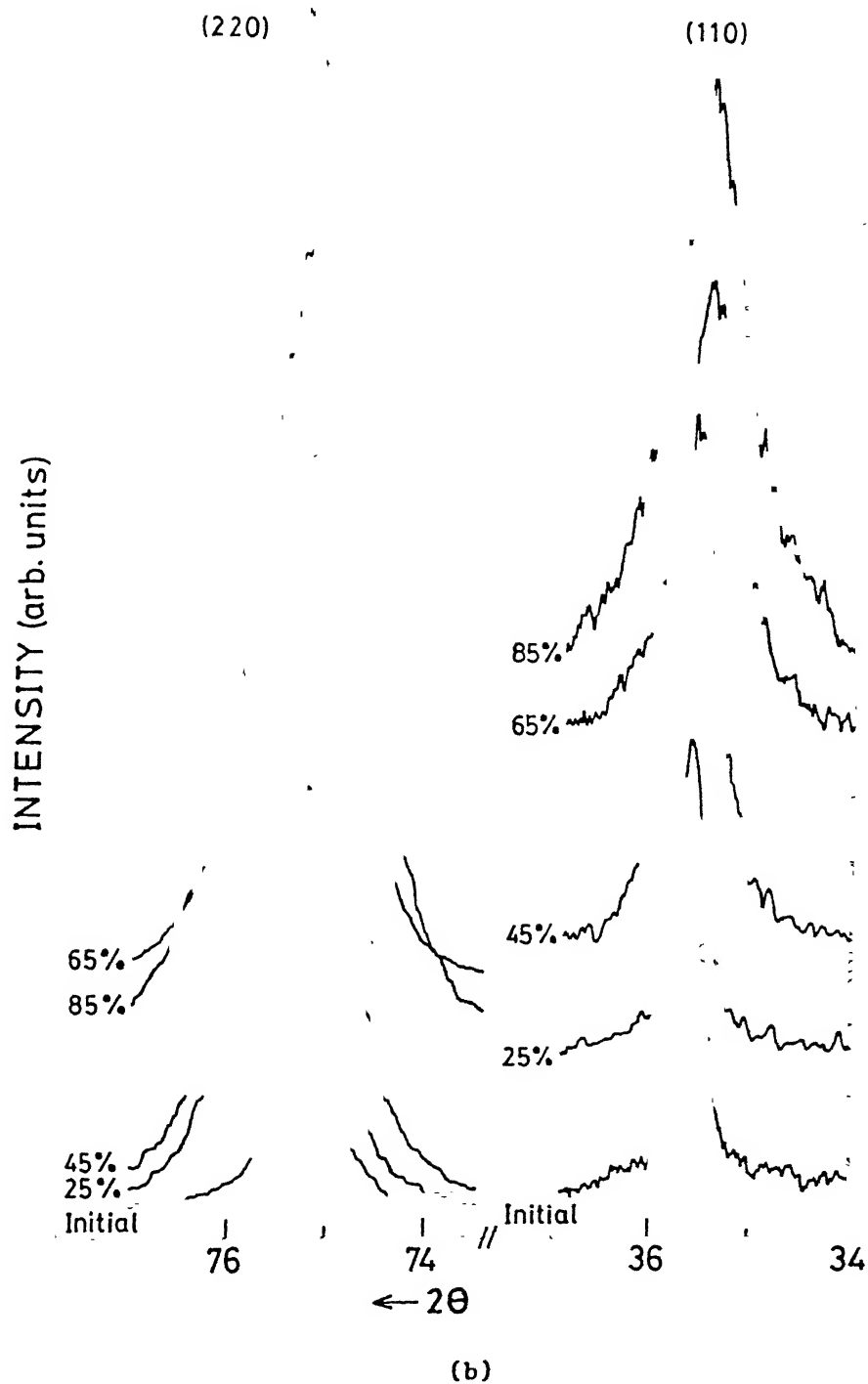


Fig.4.17 : XRD line intensities with various degrees of cold rolling

(a) (100) and (200) reflections; and

(b) (110) and (220) reflections.

possibility that this will affect the intensities of the peaks. However, the reflections chosen for order parameter measurement i.e. $(100)/(200)$ and $(110)/(220)$ are from parallel sets of planes. As a result, the textural effect will be the same on both the planes of the two pairs and therefore, it will not affect the order parameter. The effect of the degree of cold work on order parameter is depicted in Fig.4.18. The intensity of the (100) peak decreases with increasing cold work and becomes zero after 65% cold deformation. The value of the order parameter (S) calculated from the $(100)/(200)$ integrated intensity ratio progressively decreases with cold work and becomes zero after 65% deformation. By contrast, the value of S , calculated from the $(110)/(220)$ integrated intensity ratio, decreases gradually and attains a nearly constant value of 0.4 after 65% cold rolling. This value of 0.4 is retained even after 90% cold rolling. It is worthwhile to mention here that in Cu_3Au , another L1_2 structured alloy, the order parameter (S) has been found to vary in a similar way with the degree of cold rolling (Fig.4.19) [106]. In this alloy also, the S value calculated from $(100)/(200)$ reflections comes down to zero rapidly after equivalent true strain of $\epsilon = 1$, similar to the observation made in the present boron-doped $\text{Ni}_{76}\text{Al}_{24}$ alloy. By contrast, the value of S calculated from $(110)/(220)$ decreases gradually and becomes zero after 95% cold rolling. It can be seen from Fig.4.19 that the values of S measured from $(110)/(220)$ reflections after equivalent true strain of $\epsilon = 1$ is nearly 0.40 which is the same as found in the present alloy. It is known from the literature that Cu_3Au can be made completely disordered by cold rolling; whereas, as observed in the X-ray diffraction pattern of the present alloy (Fig.4.16), (100) peak disappears but (110) peak still remains after 65% deformation. These differences in behaviour may be due to changes in the local atomic configurations during cold rolling.

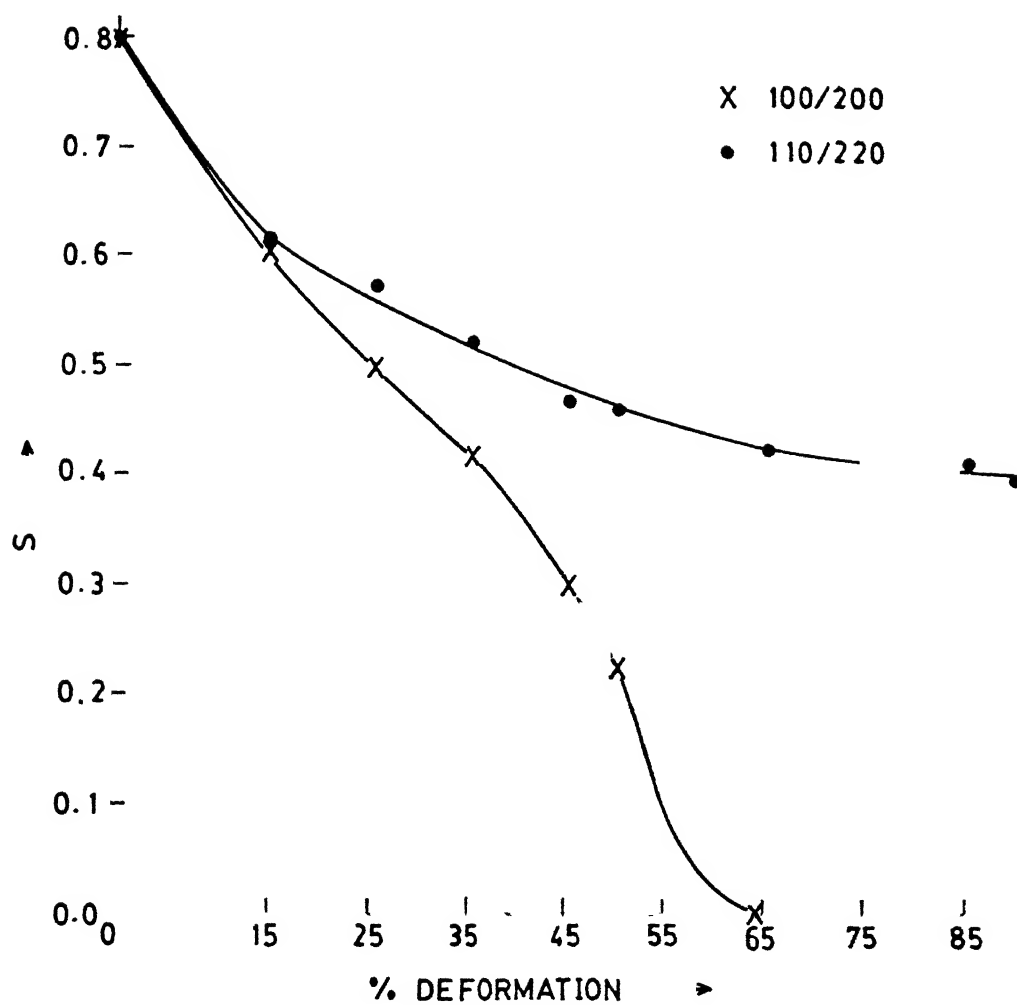


Fig.4.18 : Variation of order parameter (S) with cold rolling.

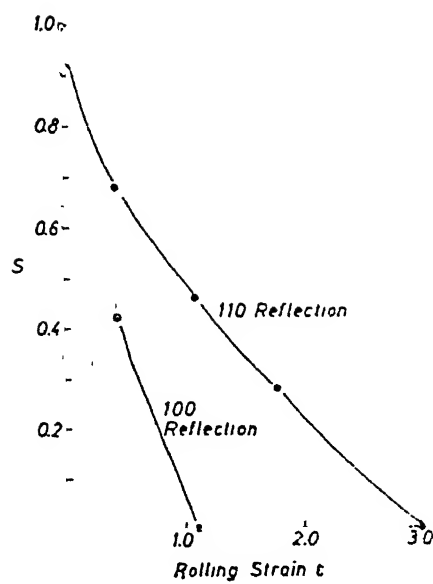


Fig.4.19 : Variation of S with cold rolling in Cu_3Au [105].

4.3.2. Crystal Structure :

The relative intensities and the peak positions of the X-ray line profiles of the 85% cold rolled sheet specimen have been listed in Table 4.1. These relative peak intensities will certainly be affected by the strong texture present in this material. Therefore, filings were prepared from the 85% cold rolled sample and X-ray diffraction pattern was taken with the powdered sample in the usual manner. The relative intensities and the peak positions of the powder sample are also listed in Table 4.1 along with those of the sheet specimen. This pattern is presented in Fig.4.20. As expected, the peak positions in the powder sample have not changed with respect to the sheet sample, but the relative intensities have changed appreciably. The theoretical relative intensities and the indices corresponding to the observed angles for the $L1_2$ structure are given in Table 4.2. Comparison of these data with those in Table 4.1 shows that there is hardly any correspondence. Disorder introduced by cold work might change the $L1_2$ structure to disordered FCC. The theoretical relative intensities and the indices of the disordered FCC structure are also listed in Table 4.2. Comparison of these data with those in Table 4.1 shows that at the two lower 2θ values the intensities of disordered FCC is zero while those of the deformed specimen are finite and at 35.57° it is 7 for the sheet material. Thus the agreement of the experimental data for the powder sample with those calculated theoretically for the disordered FCC is not satisfactory.

Sato and Toth [107], Beattie [108] and Yamaguchi et al. [13] have suggested that the $L1_2$ structure can change into the DO_{22} structure by the introduction of $1/2[110]$ APB on every $\{001\}$ plane of $L1_2$. The suggested mechanism involves deformation of $L1_2$ structure by $\{111\}\langle 101 \rangle$ slip at room temperature and shifting of atoms by $1/2\langle 101 \rangle$ along the slip plane. All these features are shown schematically in Fig.2.3. The stability of DO_{22} structure

Table 4.1 : Peak positions and relative intensities for the 85% cold rolledsheet specimen and powders made from that.

2 θ in deg.	I/I _{max.}	
	Sheet	Powder
~24	<1	<1
35.57	7	<1
43.86	15	100
50.82	8	30
75.10	100	20

Table 4.2 : Comparison of theoretical relative intensities for L1₂ and disordered FCC structures.

2 θ	L1 ₂		FCC	
	hkl	I/I _{max.}	hkl	I/I _{max.}
~24	100	16	100	0
~35	110	16	110	0
~43	111	100	111	100
~51	200	90	200	50
~75	220	55	220	25

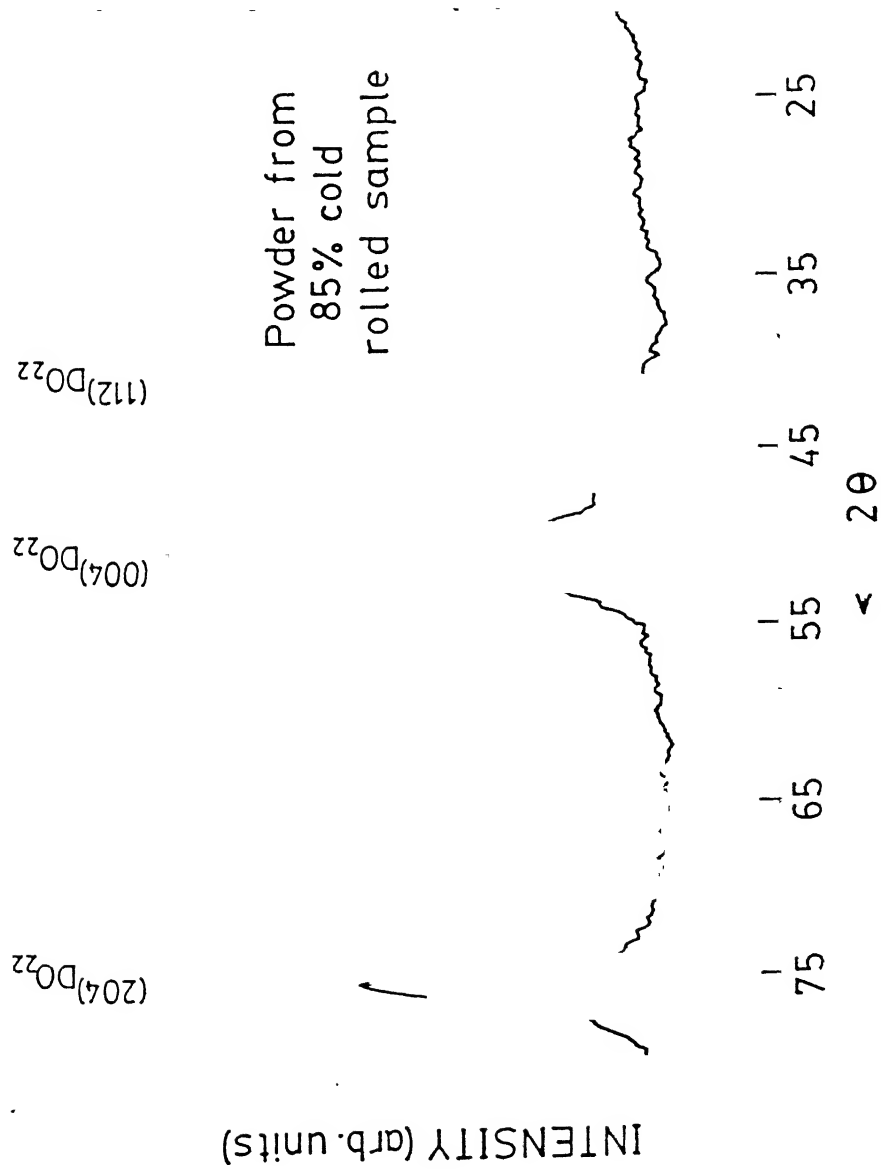


Fig.4.20 : XRD pattern of powders from 85% cold rolled $\text{Ni}_{76}\text{Al}_{24}(\text{B})$.

of $\text{Ni}_{76}\text{Al}_{24}^{(\text{B})}$ can also be inferred from the work of Ramesh et al. [12]. They observed that high temperature annealing of filed powders of a $\text{Ni}_{76}\text{Al}_{24}$ alloy led to changes in the relative intensities of $\{200\}$ and $\{220\}$ peaks as a function of the temperature of annealing. From the splitting of the $\{200\}$ peaks in their well annealed samples, they concluded that the L1_2 structure transformed to DO_{22} with a c/a ratio of ~ 2.01 above 1000°C .

It would be worthwhile to explore the possibility of a structural change in the present alloy from L1_2 to DO_{22} . The indices and relative intensities of reflections for the DO_{22} structure were theoretically calculated using appropriate multiplicity factor, p , Lorentz-polarization factor, L_p and structure factor, F and are listed in Table 4.3. The value in Table 4.3 can now be compared with the experimental values in Table 4.1. However, as c/a ratio of the DO_{22} structure is expected to be small, there will be small differences in 2θ values. Also, as the experimental intensities were taken from a heavily cold rolled material, some of the closely spaced peaks may be expected to appear as composite peak. Therefore, in order to compare the theoretical intensities, the expected composite peak were estimated in the following manner (Table 4.4). For the DO_{22} structure, the relative intensity of (002) reflection is 3 and of (010) or (100) is zero; therefore, the sum of these three overlapping peaks is taken as 3. Similarly, the sum of the relative intensities of (110), (012) and (102) reflection would be 7.5. The (004), (020) and (200) planes also tend to overlap and the combined relative intensity will be 48. Similarly, (204), (024) and (220) also tend to overlap. The intensities are 18 for (204) and (024) and 9 for (220) and the combined intensity is therefore 27. The Table 4.4 shows that the theoretical intensities expected from the DO_{22} structure compares reasonably with those obtained experimentally for the powder sample and the appreciable intensity found at the superlattice peak position, $2\theta = 35.57^\circ$, demonstrated by the

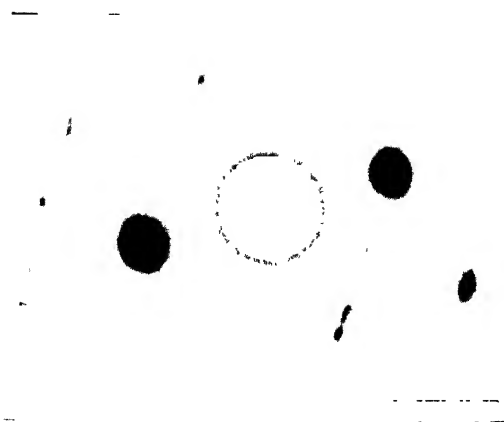
**Table 4.3 : Theoretical intensities and the peak positions
for DO_{22} structure.**

hkl	$I/I_{\text{max.}}$
100	0
002	3
110	2.5
102	5
112	100
004	16
200	32
204	18
220	9

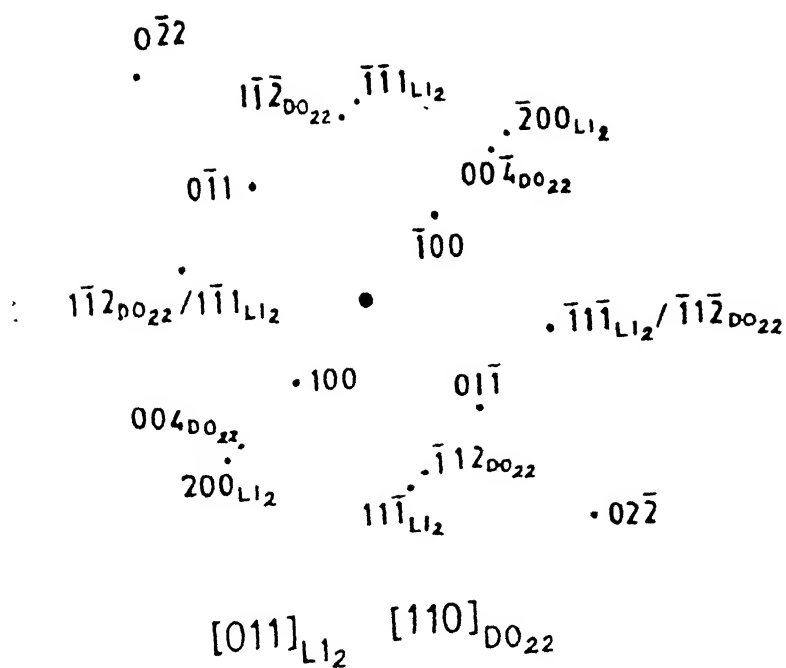
sheet material. Intensities of lines from the DO_{22} structure at higher angles are similar to those expected from disordered FCC. However, as pointed out above the intensity at $2\theta = 35.57^\circ$ is zero for disordered FCC but appreciable in the DO_{22} and the experimental pattern.

We note from Table 4.4 that the tetragonality of DO_{22} structure should result in splitting of a number of peaks. However, because of heavy cold work of the sheet material and filed powder, appreciable peak broadening and peak overlap are expected. The XRD line profiles show that as the degree of cold rolling increases from 45% to 65%, there is a marked broadening of all the lines and there is a marked shift of the peaks towards lower 2θ values for $\{200\}$ whereas the $\{220\}$ peak shifts to the higher angle side (Fig.4.17). The shift of the $\{200\}$ and $\{220\}$ peaks can be correlated with the influence of deformation faulting (in the present case it can be due to APB) on the x-ray diffraction pattern [109]. The broadening of peaks does not allow any peak splitting due to the DO_{22} structure to be clearly observed particularly because c/a ratio of the DO_{22} structure is expected to be small. However, examination of Fig.4.17 shows that the peaks obtained after 85% cold work give an indication of peak splitting. If the split reflections are designated as due to (004) and $\{200\}$, the lattice parameters of the DO_{22} structure would be $c = 7.188 \text{ \AA}$ and $a = 3.567 \text{ \AA}$, giving a c/a ratio of ~ 2.015 . This value is also comparable to the value of ~ 2.01 reported by Ramesh et al. [12].

The SAD pattern taken from a thin foil of the 45% cold rolled material is shown in Fig.4.21(a). This pattern shows the splitting of the fundamental spots. If the presence of DO_{22} structure is assumed, the SAD pattern can be analyzed on the basis of mutually parallel [011] zones of coexisting DO_{22} and $L1_2$ structures. The analysis is shown in Fig.4.21(b). The (200) and (004) spots indicate a change of about 10% in the interplaner spacings. This value is much larger than that expected from X-ray results. However, part of the



(a)



(b)

Fig.4.21 : (a) SAD pattern of 45% cold rolled $Ni_{76}Al_{24}^{(B)}$;
 (b) Analysis of the above pattern.

discrepancy may be attributed to the uncertainty of exact position of the diffused spots. The TEM specimens for the sheet sample shows a profusion of fine twins in 85% cold rolled material as discussed in Sec.4.1. It is known that the major deformation mode of the DO_{22} structure is twinning, whereas that of the disordered FCC material of such high SFE ($\sim 130 \text{ mJ/m}^2$) is unlikely to be twinning. This gives an indication that the heavily cold rolled $Ni_{76}Al_{24}^{(B)}$ may have a DO_{22} structure.

Thus, X-ray peak positions, relative intensities and the intensity ratios, tendency for peak splitting, the splitting of the spots in the SAD patter, observation of twins only at the heavy cold rolled material and a plausible mechanism for change of $L1_2$ structure to DO_{22} give a strong suggestion of the $L1_2$ structure changing into the DO_{22} structure.

4.3.3. Strain Parameter :

The strain parameter (B_r/B_o) [B_r is line breadth at half intensity for rolled sample while B_o is for initial starting material] was measured from the $\{111\}$ reflection because it was not affected by ordering of atoms but by cold rolling induced defects. It is shown in Fig.4.22 that after initial slow increase, there is a sudden drop in this parameter after 45% cold rolling. Beyond 50% deformation, it increases again and becomes more or less constant at high deformation levels.

The sudden drop in the strain parameter after 45% cold rolling can be explained as due to the formation of DO_{22} structure from the initial $L1_2$. It may be mentioned here that during cold rolling the formability of the sample was found to increase after $\sim 40\%$ reduction. Thus it can be concluded that at least a part of the energy for crack formation and propagation have been accommodated as the energy of transformation (transformation-induced plasticity).

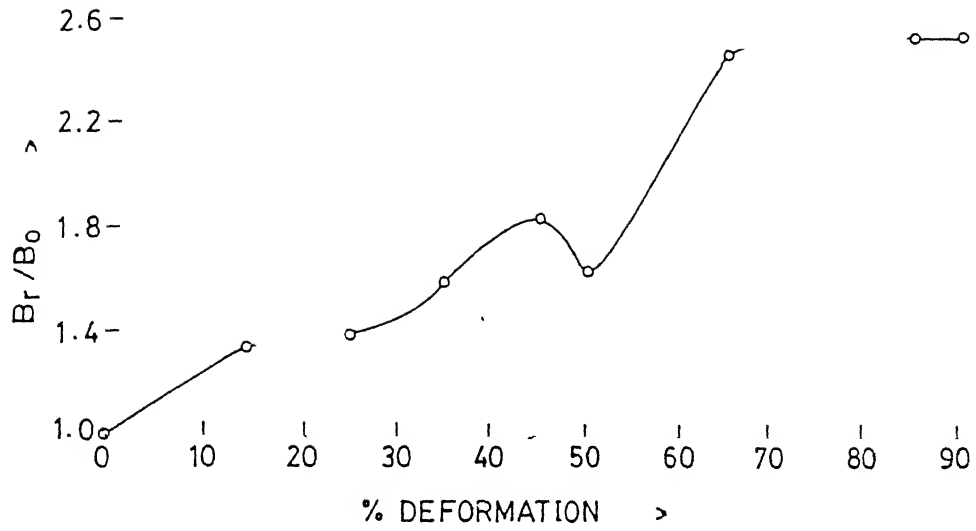


Fig.4.22 : Variation of strain parameter with cold rolling.

4.3.4. Microhardness and Resistivity :

Hardness variations with cold rolling have been plotted in Fig.4.23. The measurements have been taken after averaging out 10-12 indentation values. Hardness value increases quite fast upto 15% deformation and then shows gradual increment. However, there is a sudden softening after 45% cold rolling. The hardness value again increases and finally levels off at high deformation levels. The drop in hardness value occurs at the same deformation level where the strain parameter also shows a sudden decrease.

Resistivity has been measured by the four probe method as described in chapter III. As shown in Fig.4.24, the resistivity decreases with cold rolling which is unusual for conventional metals and alloys. This decrement continues upto 45% deformation, beyond which the resistivity value becomes nearly constant. This type of anomalous change in resistivity was first observed in Cu_2ZnNi (which was deformed by torsion), another L1_2 structured alloy [110].

4.4. Correlation of Structure with Texture Transition :

As mentioned in section 4.2, during cold rolling the pure metal type texture changes to alloy type and this could be clearly observed after 65% cold rolling. This change in texture can be correlated with the evolution of microstructure with progressive deformation. From X-ray diffraction analysis, hardness, resistivity as well as TEM SAD pattern analysis, it has been concluded (section 4.3) that during cold rolling the parent L1_2 structure changes to DO_{22} . Based on the above findings, the overall textural development in $\text{Ni}_{76}\text{Al}_{24}$ (B) alloy can be described as follows.

In L1_2 alloys, dislocation motion occurs on $\{111\}$ planes, just as in ordinary FCC metals, but the burgers vector (\vec{b}) happens to be twice as large in the ordered compound. In Ni_3Al , it is known that during slip deformation

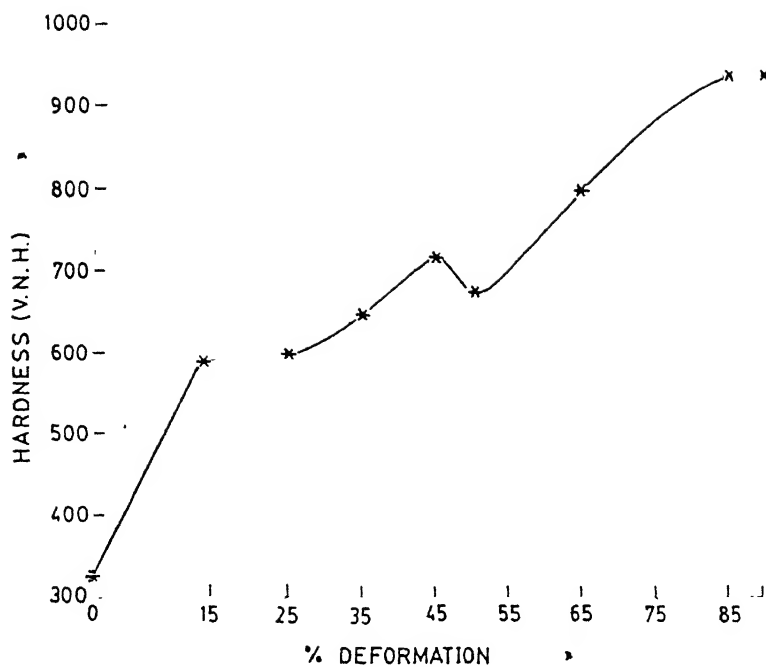


Fig.4.23 : Variation of hardness with cold rolling in Ni₇₆Al₂₄(B).

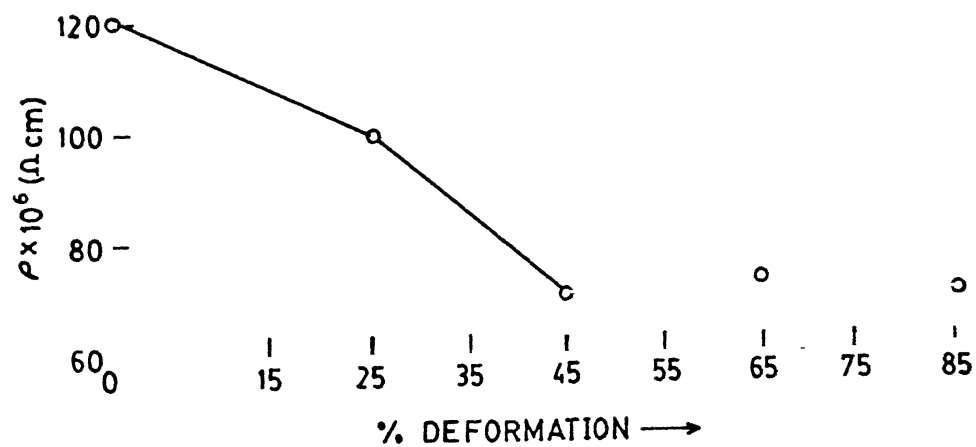


Fig.4.24 : Variation of resistivity with cold rolling in Ni₇₆Al₂₄(B).

dislocations move from the octahedral $\{111\}$ to the cubic $\{001\}$ plane and form Kear-Wilsdorf (KW) configuration. The superpartial dislocations can not expand easily on the $\{001\}$ plane and as a result, the motion of screw dislocations in the cross-slipped configuration is severely impeded. Ni_3Al having high stacking fault energy (as discussed previously) develops pure metal type texture during slip induced deformation. However, even at lower deformation levels ($\sim 25\%$), inhomogeneous deformation occur which leads to the formation of deformation bands (Fig.4.3). These bands are geometrically necessary to compensate for the incompatible strain effects. With increasing strain, strong work hardening results from the forced planar slip, which inhibits normal crystallographic slip. This leads to shear band development which can be seen in Fig.4.4(b). According to Huh et al. [111], this type of shear bands develop in the matrix region with copper orientations. The Goss orientation is also known to form in the shear bands [111].

With the progress of deformation, as pointed out earlier, boron-doped $\text{Ni}_{76}\text{Al}_{24}$ alloy transforms to DO_{22} structure. In the DO_{22} structure, $1/2\langle 112 \rangle$ is the shortest burgers vector on $\{111\}$ plane. The $1/2\langle 112 \rangle$ dislocations can dissociate into an SISF, an APB and a CSF [112]. As this dissociation process is energetically stable, it does not disturb the ordered symmetry of the DO_{22} structure. The Shockley partials having $\vec{b} = 1/6\langle 112 \rangle$ can move independently and this leads to twin formation. The above dissociation process does not disturb the ordered symmetry of DO_{22} structure. Hence, the DO_{22} structure, unlike L_{12} , deforms mainly by the twinning mode [112]. According to Wassermann [105], if mechanical twinning is an available mode of deformation, in addition to normal crystallographic slip, the Cu component $\{112\}\langle 111 \rangle$ will be transformed to $\{552\}\langle 115 \rangle$ by twinning. Further deformation of the twin orientation will then take place on the favourable slip system which will rotate it to the Goss position $\{011\}\langle 100 \rangle$ and finally to the B_s position

$\{110\}\langle 112\rangle$ by further rotation. The B_s component $\{110\}\langle 112\rangle$, on the other hand, is a stable one and will not be affected by twinning during deformation. There are certain similarities as well as differences in the development of the B_s component in the present alloy as well as in brass itself. In 70:30 brass the phenomena of twinning and shear banding at intermediate strains affect the normal development of the deformation texture and lead to the formation and growth of the B_s component [**]. Micro-twinning was observed in $Ni_3Al(B)$ right after 65% deformation and the volume of twinned material increased to a very substantial amount after 85% cold work. The attendant increment in the B_s component can be attributed mostly to the presence of microtwins as in the case of brass. The intensity of the B_s component, after 85% cold rolling, is practically the same as after 65% cold deformation. On the other hand, within this range, the intensity of the rotated Goss component $\{011\}\langle 110\rangle$ increases perceptibly. The Brass and the rotated Goss component are related by a rotation of 55° around $[110] \parallel ND$.

The increase in the intensity of the rotated Goss component and a nearly constant pole density for the B_s component during the deformation range 65%-85% strongly suggest that there is a limited amount of rotation of B_s oriented regions into the rotated Goss. The manner in which this may take place is still unclear. However, since, the B_s component is not generally known to twin that easily and the theoretically derived first and second generation twins from the B_s component are nowhere near the rotated Goss component $[113]$, it may be assumed that the observed rotation takes place by shear banding. It may be recalled that at this stage normal slip is almost inhibited and therefore, the occurrence of a high density of shear bands automatically point to the possibility of such a situation. The observed textural changes during the deformation of boron-doped $Ni_{76}Al_{24}$ alloy can be shown schematically in the $\phi_2 = 45^\circ$ section of an ODF (Fig.4.25).

** : B.J.Duggan, M.Hatherly, W.B.Hutchinson and P.T.Wakefield, Met.Sci., August 343 (1978).

CHAPTER V

ANNEALING CHARACTERISTICS

5.1. Recovery :

In order to find out the effect of temperature on various annealing stages in cold rolled boron-doped $\text{Ni}_{76}\text{Al}_{24}$ alloy, isochronal annealing was carried out between room temperature and 1000°C at intervals of 100°C . In this experiment, specimens were annealed at each isochronal annealing temperature for 1 hour and the effect of annealing temperature on various properties were measured.

5.1.1. Order Parameter :

The effect of isochronal annealing on the long range order parameter (S) of specimens cold rolled by 25%, 45% and 85% were measured from the integrated intensity ratios of (100)/(200) and (110)/(220) pairs of reflections as mentioned previously. The results for the (100)/(200) and (110)/(220) pairs of reflections for samples with different levels of deformation are shown in Figs.5.1(a) and (b), respectively. The 25% cold rolled sample shows (Fig.5.1(a)) gradual increase in the order parameter, S [calculated from (100)/(200)] from 0.48 at the beginning to about 0.8 at 1000°C . The value of S for the 85% cold rolled material was initially zero. It remains so till upto 200°C ; however, it shoots up to 0.55 in the temperature range $200^{\circ} - 400^{\circ}\text{C}$, beyond which it increases gradually and attains the maximum value of 0.8 at 1000°C . For the 45% cold rolled sample the initial value of 0.3 at first decreases to zero at 100°C and remains at zero upto 300°C . It then quickly increases to about 0.55 between $300^{\circ} - 500^{\circ}\text{C}$, beyond which it increases slowly and finally approaches the value of 0.8 at 1000°C . The order parameter value calculated from (110)/(220) pair of reflections shows gradual increase in the value of S for all the three cold

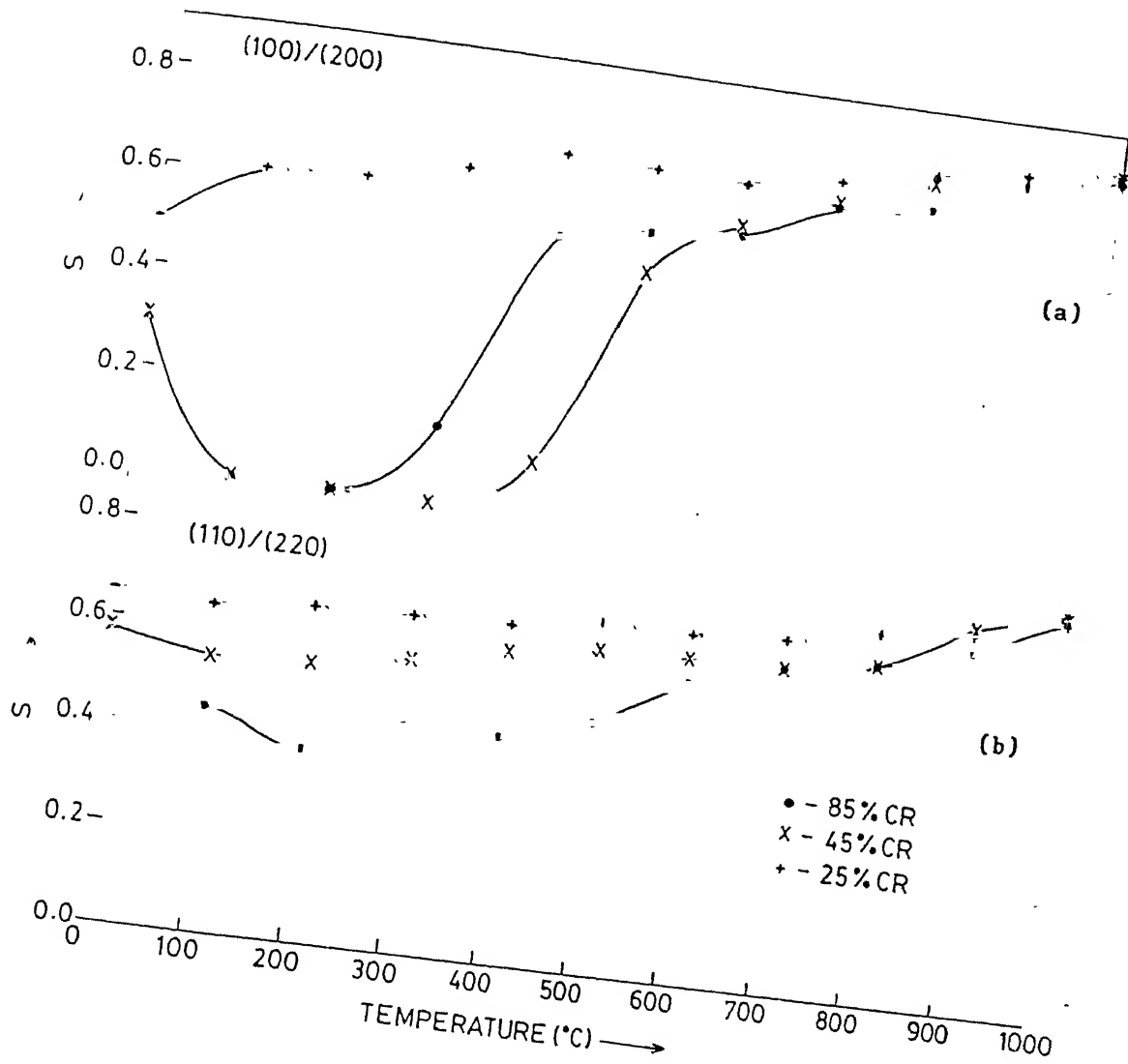


Fig.5.1 : Effect of isochronal annealing on S of cold rolled samples: (a) (100)/(200); (b) (110)/(220) reflections.

rolled samples (Fig.5.1(b)).

The above isochronal annealing curves clearly indicate a major change in order parameter between 200° - 600°C in the cold rolled samples. In order to further investigate changes within this temperature range, isothermal annealings are carried out at 525° and 625°C . The variation of the order parameter during isothermal annealing at 525° and 625°C of the 85% cold rolled sample is shown in Fig.5.2. It shows that after initial increase, the order parameter becomes more or less constant. Thus, the rate of ordering is initially large and decreases with time. Such behaviour is typical for ordering reactions. The changes in the order parameter for isothermal annealing at 850°C are plotted in Fig.5.3. The order parameter $S_{100/200}$ after 1 hour of annealing shoots up to about 0.62 and then gradually increase to the maximum (0.8) after 24 hours. $S_{110/220}$ is also of similar nature. Thus, the behaviour is along the expected lines.

The XRD line profiles for the 85% cold rolled sample in the as rolled condition and after annealing at 850°C for 17 hours and at 950°C for 1 hour are represented in Fig.5.4. These indicate that the DO_{22} structure of 85% cold rolled material reverts back to the initial L1_2 structure after annealing.

5.1.2. Strain Parameter :

The effects of isochronal annealing for 1 hour on the strain parameter, B_r/B_w [B_r is for annealed; B_w is for cold rolled material] of specimens cold rolled by 25%, 45% and 85% are shown in Fig.5.5. The strain parameter decreases continuously in the 25% cold rolled sample. This is consistent with the slow increase in order parameter during the corresponding period. In the 85% cold rolled sample, the strain parameter decreases slowly upto 300°C and then quickly drops down to a low value between 300° - 500°C . This fast relief in strain can be correlated with the increase in order parameter in the same

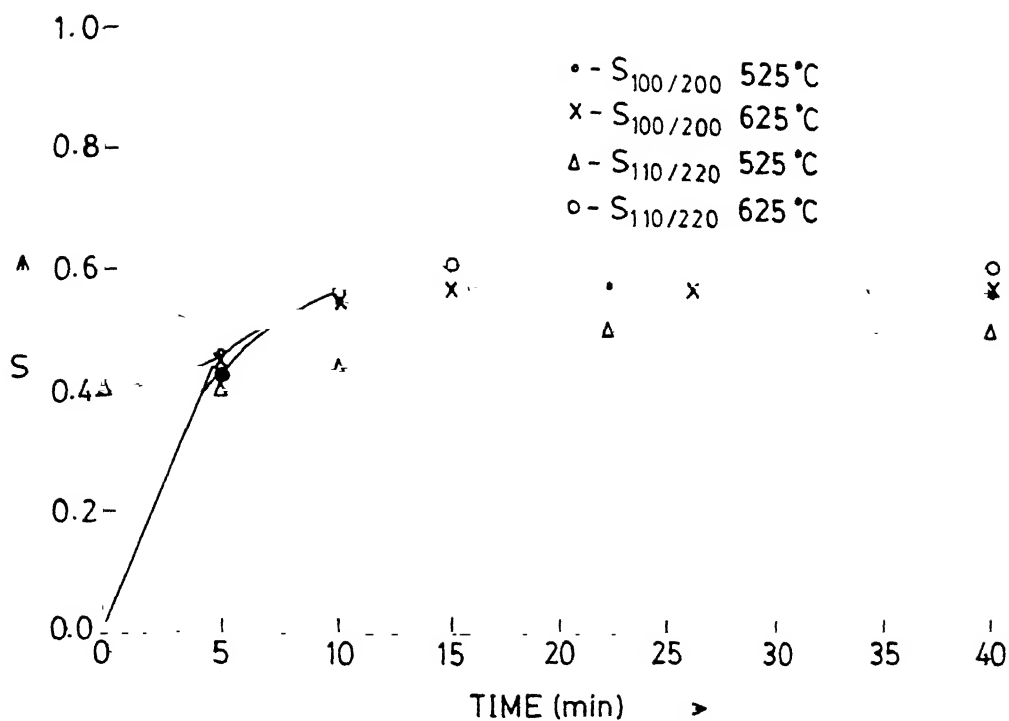


Fig.5.2 : Variation of S with time at 525° and 625°C.

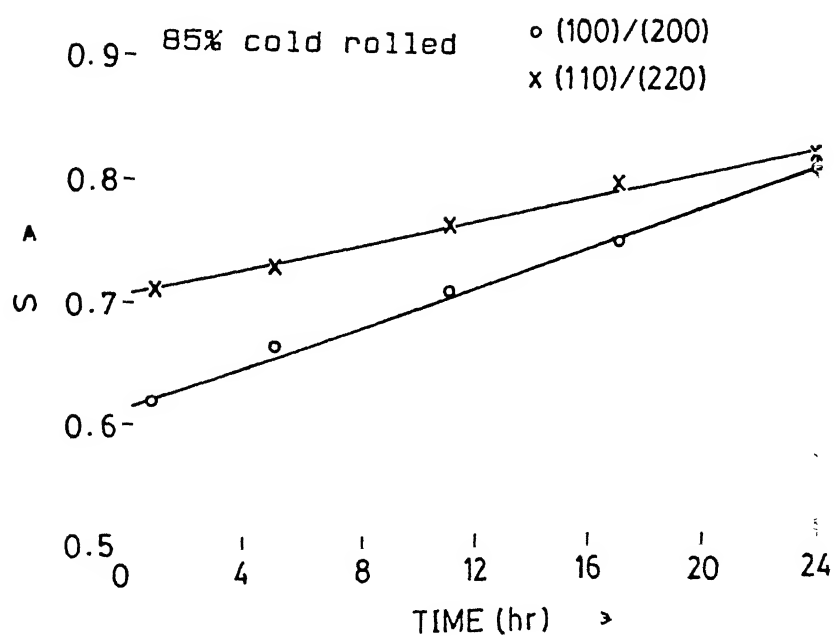


Fig.5.3 : Variation of S with time at 850°C.

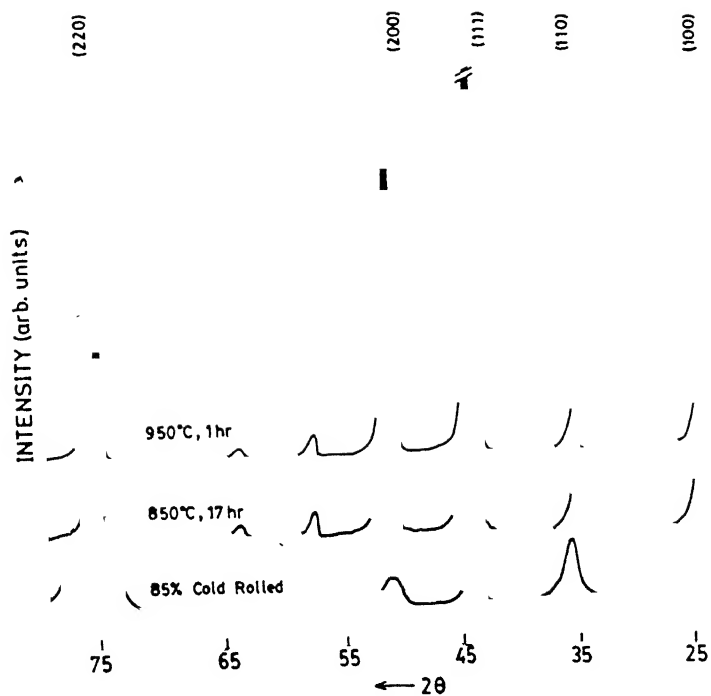


Fig.5.4 : XRD line profiles for annealed samples.

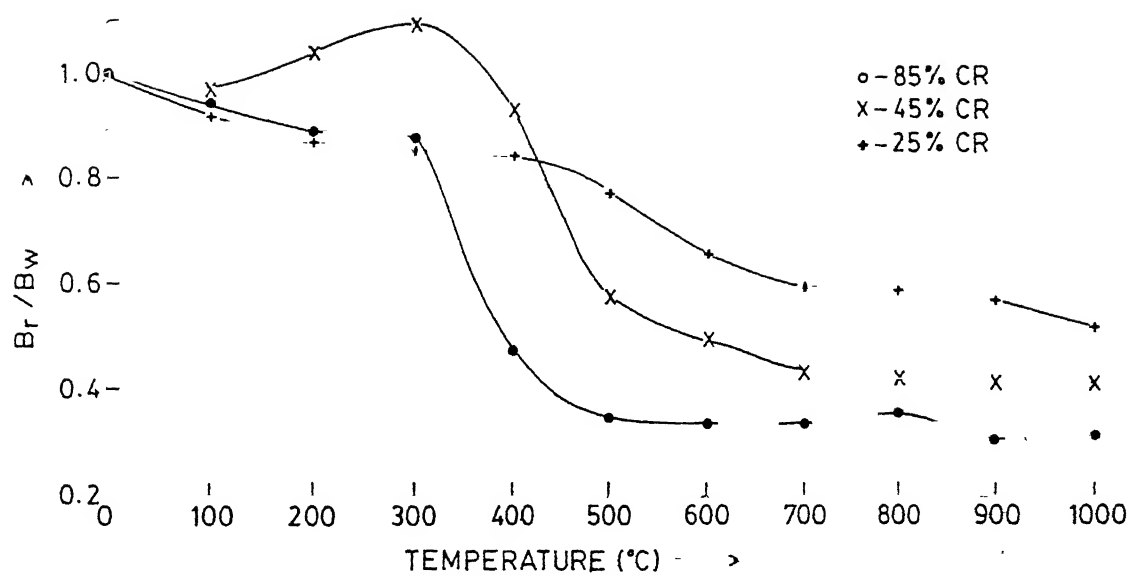


Fig.5.5 : Variation of strain parameter with isochronal annealing temperature.

temperature range. However, in 45% cold rolled sample, the strain parameter increases at around 300°C , beyond which it decreases rather fast with increasing temperature. The 45% cold rolled sample, therefore, behaves in an unusual manner both in the development of order and relief of strain on annealing. There is an initial decrease in order parameter with temperature and this is associated with an increase in the strain parameter. The subsequent increase in S is again associated with a decrease in strain within the same temperature range.

The variation of the strain parameter with time at different isothermal annealing temperatures ($250^{\circ} - 350^{\circ}\text{C}$) for 85% cold rolled samples are shown in Fig.5.6. This is a normal behaviour of strain energy release during recovery of heavily cold rolled material.

5.1.3. Microhardness :

Measurement of microhardness on the 85% cold rolled samples has been done for different periods of annealing at temperatures ranging from 750° to 900°C . The results are presented in Fig.5.7, in which each data point is the average of ten measurements. The scatter in the data is negligible.

The hardness decreases monotonically with annealing time and drops very quickly with increasing temperature. The softening is very fast before recrystallization sets in. This indicates that a large amount of driving force has been expended during recovery itself. To have an insight into this process, the temperature effect on the change in microhardness for a given annealing time (1 hour in this study) was measured and the results are shown in Fig.5.8. The change in hardness has been found to be strongly dependent on the amount of cold work at least at lower temperatures. In case of the 25% cold rolled sample, hardness drop is more or less comparable to that in pure metals and alloys. In case of the 45% cold rolled sample, hardness decreases gradually except for a small hump around 500°C . The sample having 85% cold

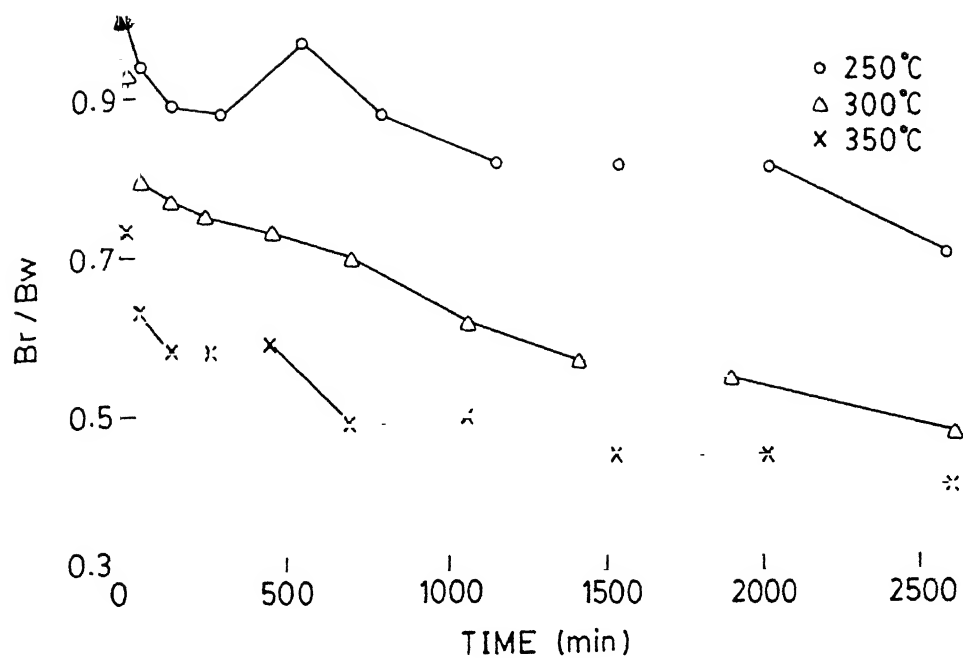


Fig.5.6 : Variation of Strain Parameter with time in the temperature range of 250° - 350°C.

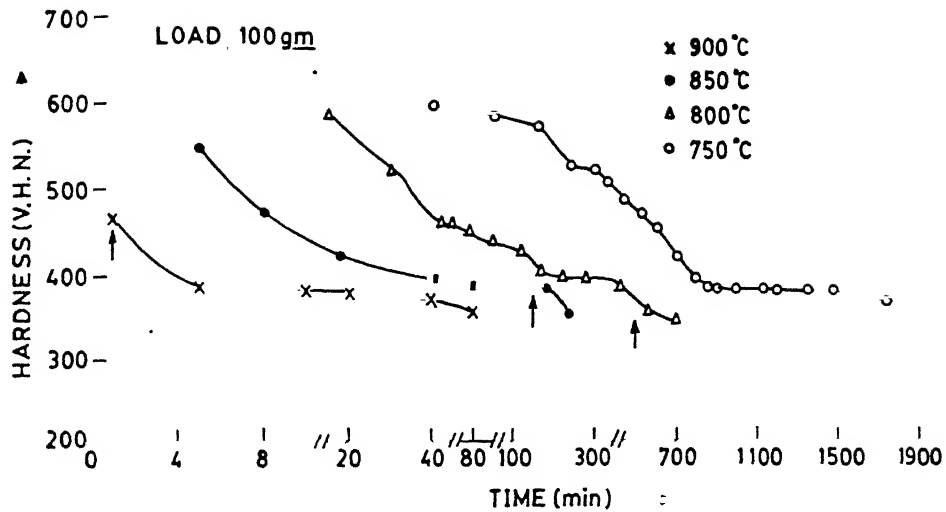


Fig.5.7 : Variation of hardness during isothermal annealing.

↑ denote starting of recrystallization

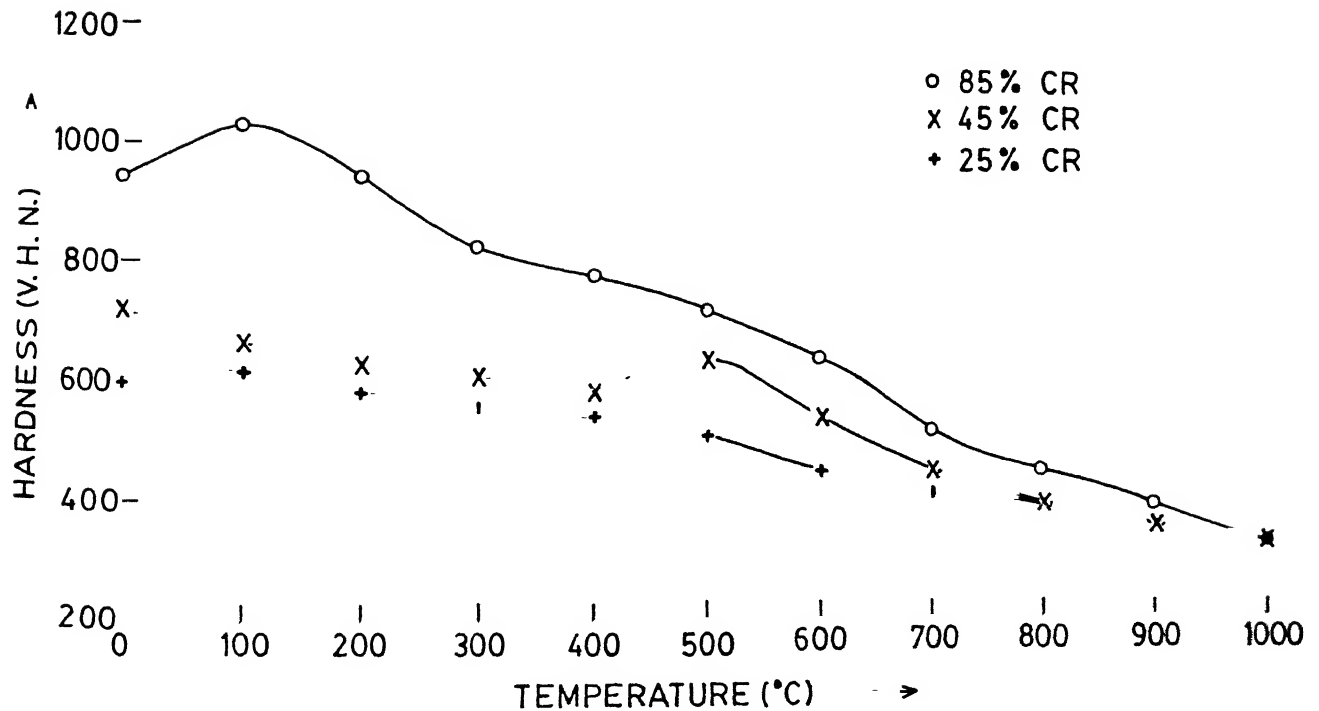


Fig.5.8 : Variation of hardness with isochronal annealing temperature.

work, initially hardens a bit at 100°C , followed by gradual decrease in hardness. To check the phenomena occurring around 500°C , hardness measurements were also made on 85% cold rolled samples annealed isothermally at 525° and 625°C (Fig.5.9). Annealing at 525°C shows increase in hardness within 5 minutes and this is maintained till upto an annealing time of 3 hours. Annealing at 625°C also shows increase in hardness within 5 minutes, but this increase is much less than that in the previous case. Beyond 5 minutes of annealing, however, the microhardness drops and maintains a steady value till about 35 minutes of annealing after which it drops again. The presence of short time hardness maxima at lower temperatures are consistent with the observed increase in the values of S during this period. This indicates that the recovery phenomenon is associated with distinct atomic rearrangement in the unit cell level (reordering).

5.1.4. Microstructure :

It was shown in chapter IV that the heavily cold rolled (85%) microstructure of this alloy was characterized by extensive deformation twinning and clusters of microbands (Fig.4.10(c)).

Low temperature annealing (at 300°C) leads to recovery of the dislocated substructure. Fig.5.10 shows a typical area where dislocation rearrangement prior to subboundary formation can be seen. At a few places, however, the heavily twinned structure of the cold rolled material persists (Fig.5.11). When the temperature of annealing increases to 500°C , some strikingly new features start appearing. Groups of parallel stripes running nearly perpendicular to original grain boundaries are observed (Fig.5.12). Features similar to these stripes were also observed in a Cu_3Pt alloy during disordered to L1_2 transformation [114]. These stripes were identified by those authors as ordered domains of the L1_2 structure. It has already been seen (Sec.5.1.1) that at this temperature, in the present $\text{Ni}_{76}\text{Al}_{24}(\text{B})$ alloy,

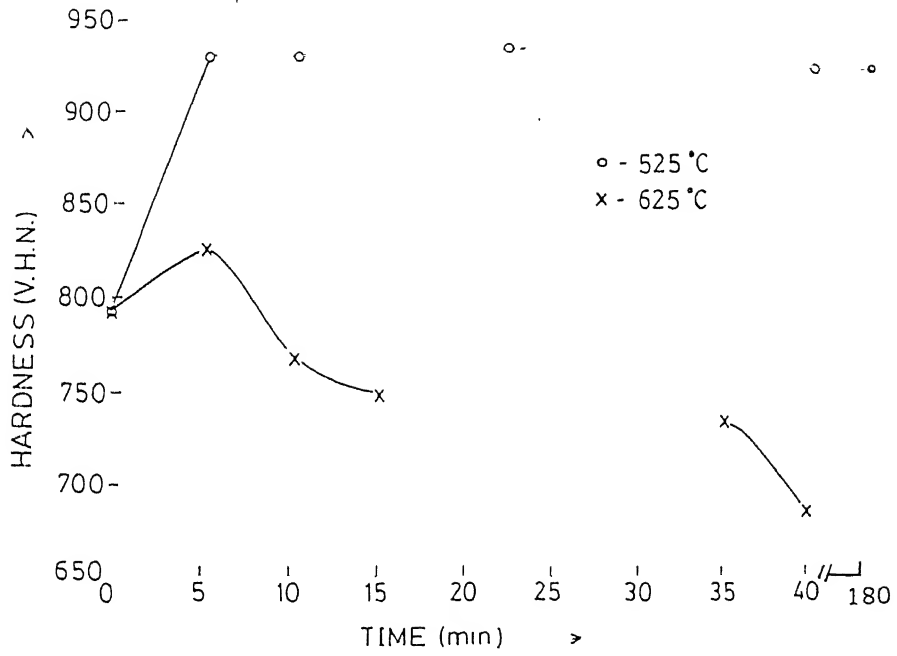


Fig.5.9 : Short range hardness maxima at 525° and 625°C.

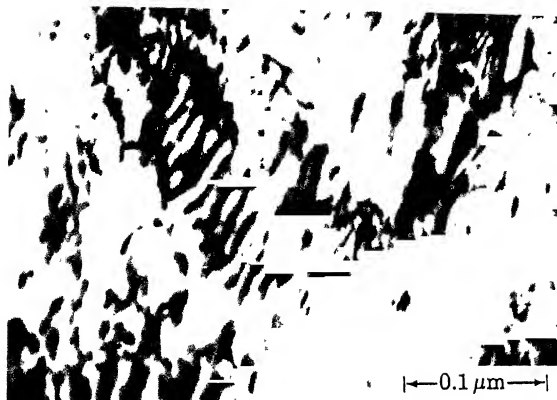


Fig.5.10 : Sub-boundary formation during annealing at 300°C.



Fig.5.11 : Deformed microstructure retained after annealing at 300°C.

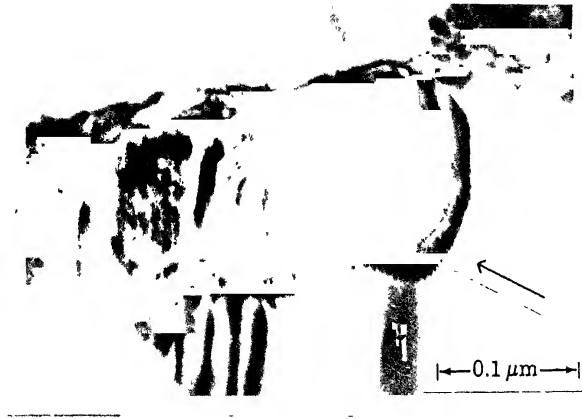


Fig.5.12 : Stripe-like features emanating from the grain boundaries.

a distinct change of structure from DO_{22} to $L1_2$ takes place. The stripe-like features in this case, therefore, can be considered as due to the formation of $L1_2$ structured regions from the DO_{22} . A distinct moiré fringe like feature observed at the grain boundary (shown with an arrow in Fig.5.12) indicates the possible coexistence of two phases of nearly the same lattice parameters. It may be mentioned that although the unit cell of DO_{22} structure is twice that of $L1_2$, the interplaner spacings of $\{hkl\}$ planes are very nearly equal in the two cases.

Fig.5.13 shows an area with a high density of the stripe-like $L1_2$ domains. Sometimes domains emanating from the grain boundaries are arranged in a criss-cross fashion (Fig.5.14).

The samples annealed at 500°C for longer periods of time have also been observed to possess similar features. However, in addition to these, twins are sometimes observed within the grains. The morphology of these twins are different from that in the deformed materials. Fig.5.15(a) shows a typical area which has sufficiently recovered and has a high density of those twins. SAD pattern taken from this area (Fig.5.15(b)) shows the $[011]$ pattern of the $L1_2$ structure but does not show distinct twin spots. The key to the diffraction pattern is given in Fig.5.15(c).

Annealing at higher temperature (at 700°C) leads to copious nucleation of large number of subgrains. A typical micrograph showing a just formed subgrain from the cold rolled matrix is given in Fig.5.16. Formation of large number of subgrains and their competitive growth is shown in Fig.5.17 where the subgrain A is found to advance into the neighbouring subgrains by subboundary migration. There is the possibility of subgrain coalescence also (see subgrains B, C and D in Fig.5.17). The subgrain A, because of its size advantage over the surrounding subgrains will grow fast and can be considered ultimately to act as nucleus for a recrystallized grain. A group of such

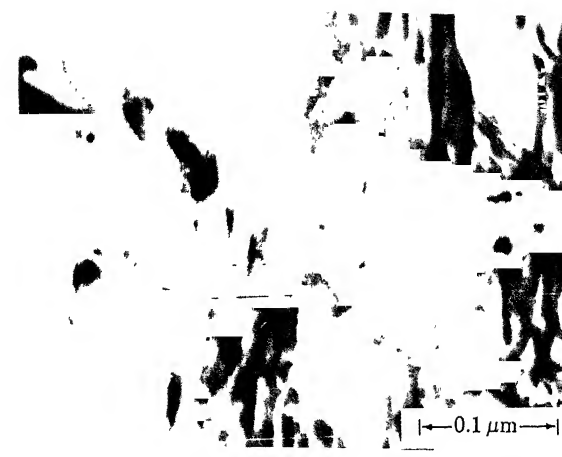


Fig.5.13 : High density of stripe-like $L1_2$ domains near the grain boundaries after annealing at 500°C .

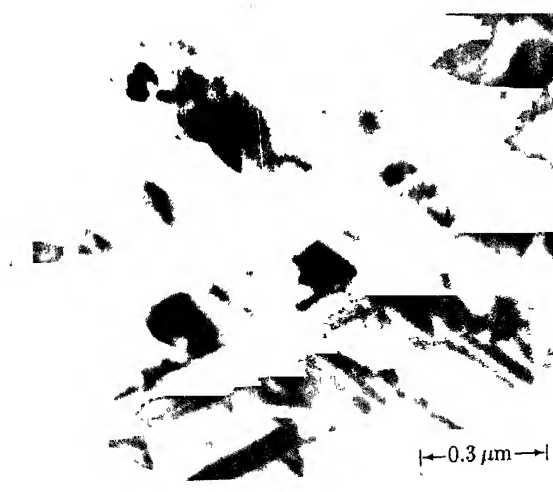


Fig.5.14 : Criss-cross arrangements of $L1_2$ structured domains after annealing at 500°C .

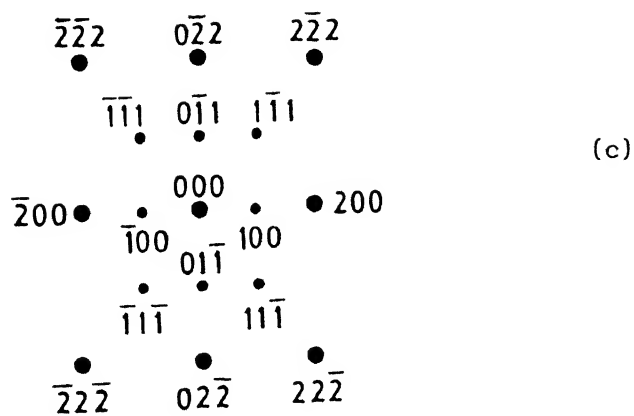
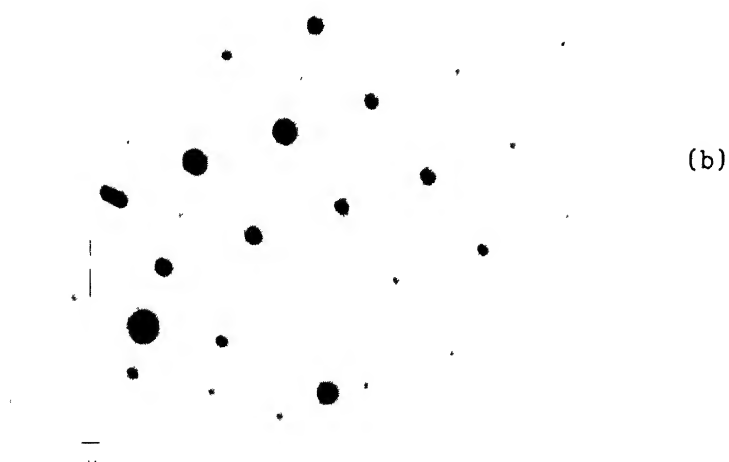
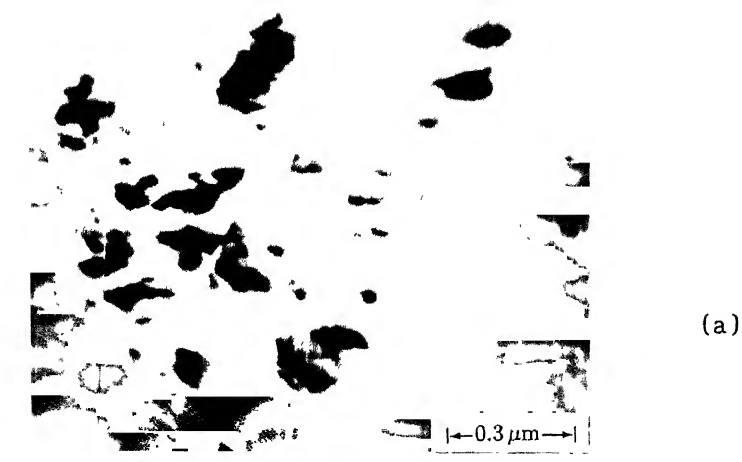


Fig.5.15 : (a) Formation of twins after annealing at 500°C, (b) SAD pattern of that area and (c) its analysis.



Fig.5.16 : Formation of subgrain from a cold rolled matrix after annealing at 700°C.

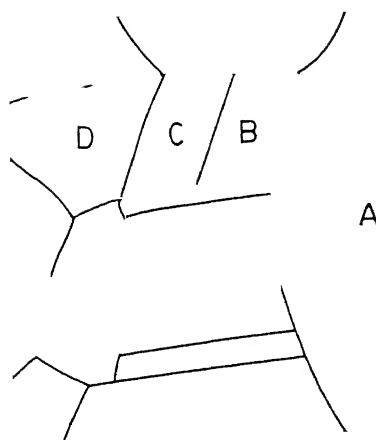


Fig.5.17 : Competitive growth of subgrains after annealing at 700°C.

small subgrains in an area of the 700°C annealed material is shown in Fig.5.18. Fig.5.19(a) again shows a typical partly recrystallized area. The SAD pattern taken from the central recrystallized grain (Fig.5.19(b)) shows a [011] pattern of the $L1_2$ structure.

Finally, recrystallization is found to be essentially complete after annealing for 1 hour at 925°C. Annealing beyond that stage practically leads to the grain growth stage. Fig.5.20 shows a typical optical microstructure of a fully recrystallized $Ni_{76}Al_{24}$ (B) alloy.

5.1.5. Energetics :

5.1.5.1. Analysis of DSC data :

For isolating the heat effects due to reactions occurring in the alloy, two separate DSC runs were carried out under identical conditions. In the first run, high purity platinum was used in both the sample and the reference pans and in the second run the platinum in the sample pan was replaced by the 85% cold rolled $Ni_{76}Al_{24}$ (B) samples. In the first run, the heat flow, \dot{q}_1 , to the reference relative to the sample is

$$\dot{q}_1 = \frac{\phi}{E} [C_{h(R)} - C_{h(S)}] + \frac{\phi}{E} [C_{Pt(R)} - C_{Pt(S)}] \quad \dots\dots 5.1$$

where E is the calibration constant, ϕ is the heating rate, $C_{h(R)}$ and $C_{h(S)}$ are the heat capacities of the reference and the sample pans, respectively; $C_{Pt(R)}$ and $C_{Pt(S)}$ are the heat capacities of Pt in the reference and the sample pans, respectively. Due to the second run, the heat flow, \dot{q}_2 , is

$$\dot{q}_2 = \frac{\phi}{E} [C_{h(R)} - C_{h(S)}] + \frac{\phi}{E} [C_{Pt(R)} - C_{A(S)}] + \frac{\dot{Q}M}{E} \quad \dots\dots 5.2$$

where $C_{A(S)}$ and M are the heat capacity and mass of the cold rolled sample, respectively; \dot{Q} is the rate of heat evolution per unit mass due to reactions in the sample. As the same reference and sample pans were used, subtraction of eqn.5.1 from eqn.5.2 yields

$$(\dot{q}_2 - \dot{q}_1) = \frac{\phi}{E} [C_{Pt(S)} - C_{A(S)}] + \frac{\dot{Q}M}{E} \quad \dots\dots 5.3$$

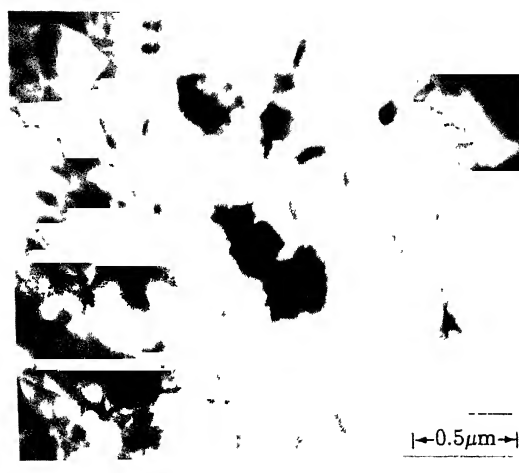
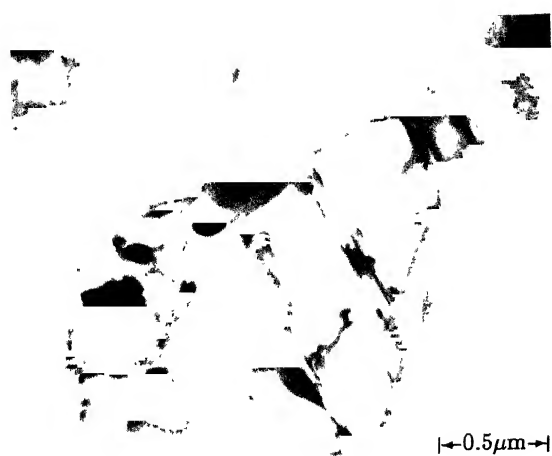
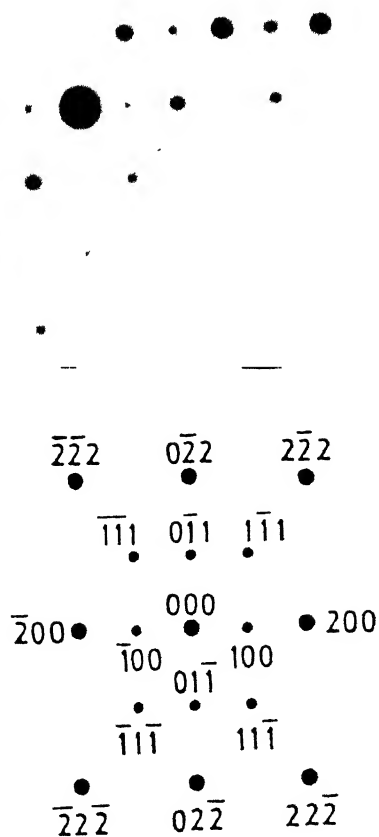


Fig.5.18 : Formation of group of subgrains after annealing at 700°C.



a



b

Fig.5.19 : (a) Partly recrystallized area after annealing at 800°C and (b) its SAD pattern and analysis.

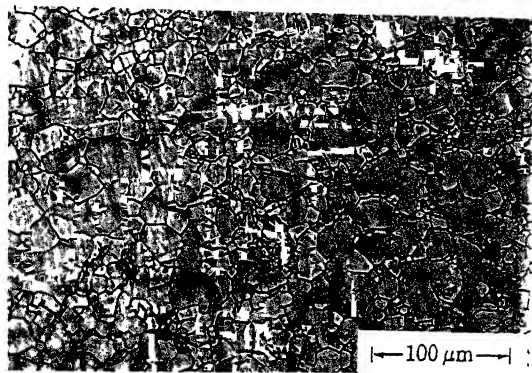


Fig.5.20 : Full recrystallization after annealing at 925°C.

The quantity, $(\phi/E)[C_{Pt(S)} - C_{A(S)}]$ of eqn.5.3 is a small correction term. When there is no reaction in the sample ($\dot{Q}=0$), eqn.5.3 reduces to

$$(\dot{q}_2 - \dot{q}_1)_{\dot{Q}=0} = \frac{\phi}{E} [C_{Pt(S)} - C_{A(S)}] \quad \dots\dots 5.4$$

Substitution of eqn.5.3 from eqn.5.4 yields the correct thermogram.

$$\frac{\dot{Q}}{E} M = (\dot{q}_2 - \dot{q}_1) - (\dot{q}_2 - \dot{q}_1)_{\dot{Q}=0} \quad \dots\dots 5.5$$

This equation is used to obtain the value of $(\dot{Q}M/E)$ as a function of temperature.

The heat effect $Q(T)$ observed in the temperature range T_i to T is obtained by integrating eqn.5.5

$$Q(T) = \frac{E}{M\phi} A(T) \quad \dots\dots 5.6$$

$$\text{where, } A(T) = \int_{T_i}^T (\dot{q}_2 - \dot{q}_1) - (\dot{q}_2 - \dot{q}_1)_{\dot{Q}=0} dT$$

If T_f is the final temperature of the peak,

$$Q(T_f) = \frac{E}{M\phi} A(T_f) \quad \dots\dots 5.7$$

The mole fraction (Y) of the phase which undergoes transformation is related to the heat effects and can be written as

$$Y = \frac{n}{n_e} = \frac{A(T)}{A(T_f)} \quad \dots\dots 5.8$$

where n and n_e are number of moles of transformation product at any temperature and equilibrium number of moles of product phase per gram of the alloy, respectively. The value of n and n_e can be determined in terms of total heat effect up to a given temperature and the heat effect under the peak, respectively, according to eqn.5.8.

5.1.5.2. Identification of peaks :

The principal features of DSC thermograms of 85% cold rolled alloy are two exothermic peaks A and B (Fig.5.21). The peak A shifts to higher temperature side with increase in heating rate (Fig.5.22). The microstructure corresponding to the beginning of the peak A (321°C) is shown in Fig.5.23(a), which indicates that the structure here is the same as the cold rolled structure. The microstructure taken at the temperature corresponding to the end of the peak A (641°C) does not yet show the start of recrystallization (Fig.5.23(b)). The position of the peak B is not so dependent on the heating rate, except that the intensity of that peak decreases with increase in heating rate. It is mentioned in section 5.2 that after annealing at 300°C , the structure remains DO_{22} ; however, after 500°C , the structure changes to L1_2 . The XRD analysis also indicates the restoration of the L1_2 structure at this stage (Fig.5.1). Hence, the peak A can be associated with the recovery process which is associated with the change of order from DO_{22} to L1_2 . The characteristics of peak A are tabulated in Table 5.1. The enthalpy of the reaction calculated from the thermograms is 11.5 kJ/mol . The microstructure at 900°C shows full recrystallization with fine grain size (Fig.5.24). Thus, peak B can be associated with the process of recrystallization after recovery and reordering. The variation of the fraction transformed was analyzed from the peak A and the data have been plotted against temperature in Fig.5.25.

5.1.5.3. Kinetic Analysis :

The Y-T curve (Fig.5.25) is sigmoidal in shape. The curve shifts a little to the right with increase in heating rate. This means that the transformation is kinetically controlled.

Therefore, if the rate is high i.e. temperature is high enough, the rate of heat evolution would be simply proportional to the equilibrium number of moles of L1_2 phase per gram of the sample present at that point. The rate of

DSC 1500
STANTON REDCROFT

SMPL ID : R-pt S-Ni3Al
RUN ID : 15 deg per min
SIZE : 46.500 mg
OPERATOR: Sandip

DATE RUN: Jan/11/1995
GASES : Ar-I-1
SOURCE :
COMMENT : Cold roll 85 %

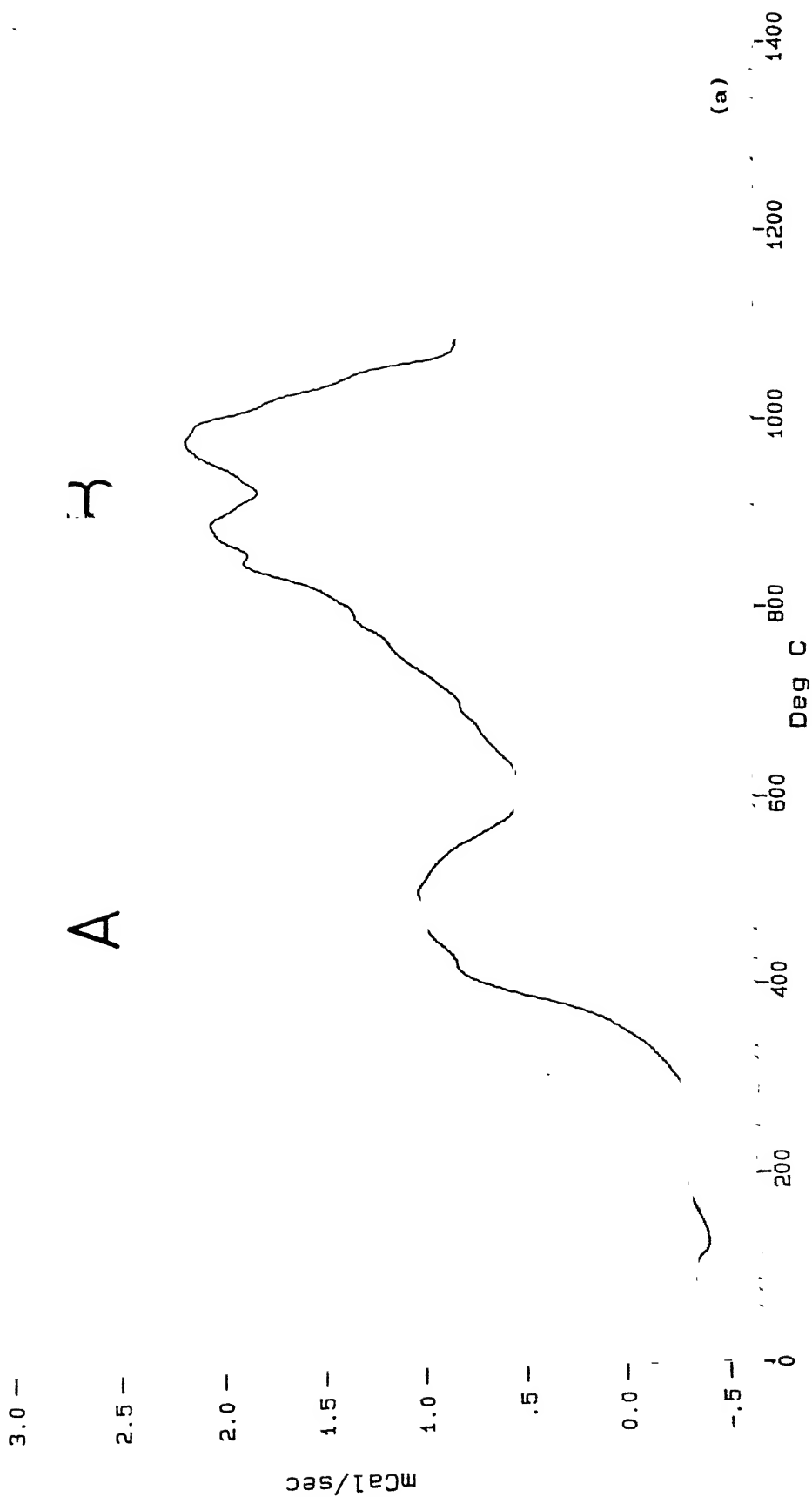


Fig. 5.21

DSC 1500
STANTON REDCROFT

SMPLE ID : R-Pt S-Ni3Al
RUN ID : 20 deg per min
SIZE : 46.800 mg
OPERATOR: sandip

DATE RUN: Mar/15/1995
GASES : Ar-I-1
SOURCE :
COMMENT : 85% cold rolled

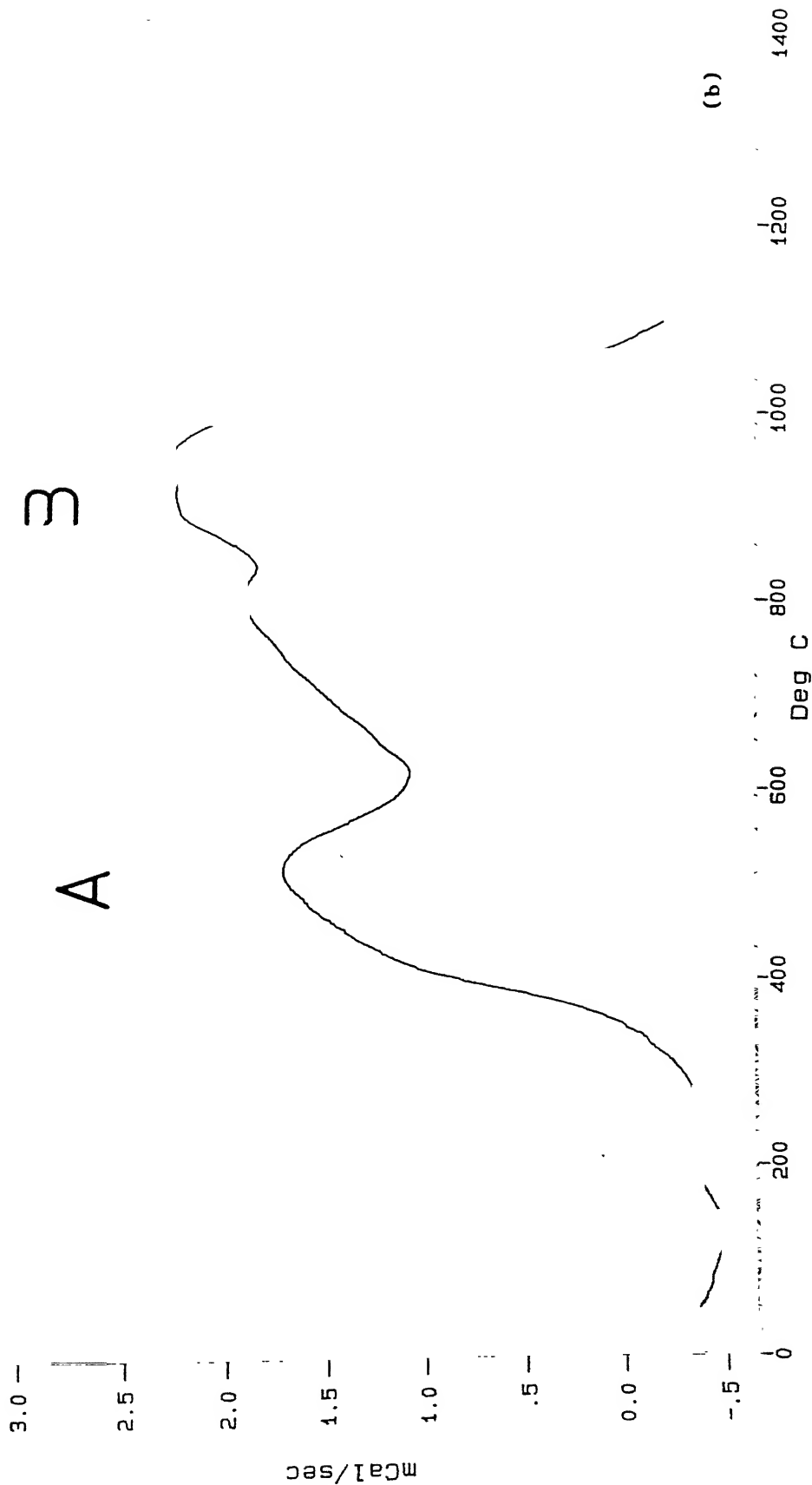


Fig.5.21

DSC 1500
STANTON REDCROFT

SMPL ID : R-Pt S-Ni3Al
RUN ID : 25 deg per min
SIZE : 46.800 mg
OPERATOR: sandip

DATE RUN: Mar/08/1995
GASES : Ar-I-1
SOURCE :
COMMENT : 85% cold rolled

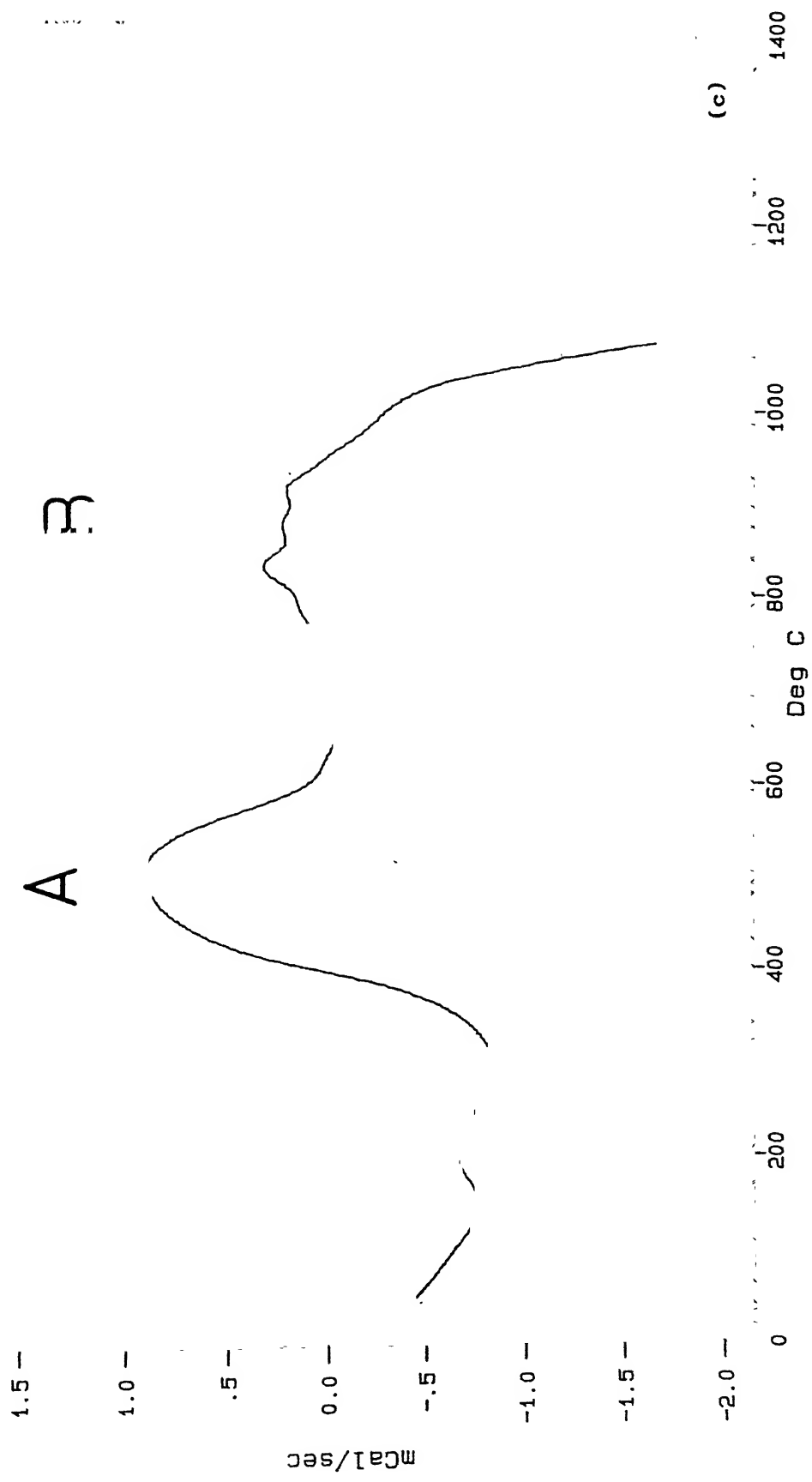


Fig.5.21 : DSC thermograms of 85% cold rolled Ni₇₆Al₂₄ (B) alloy.

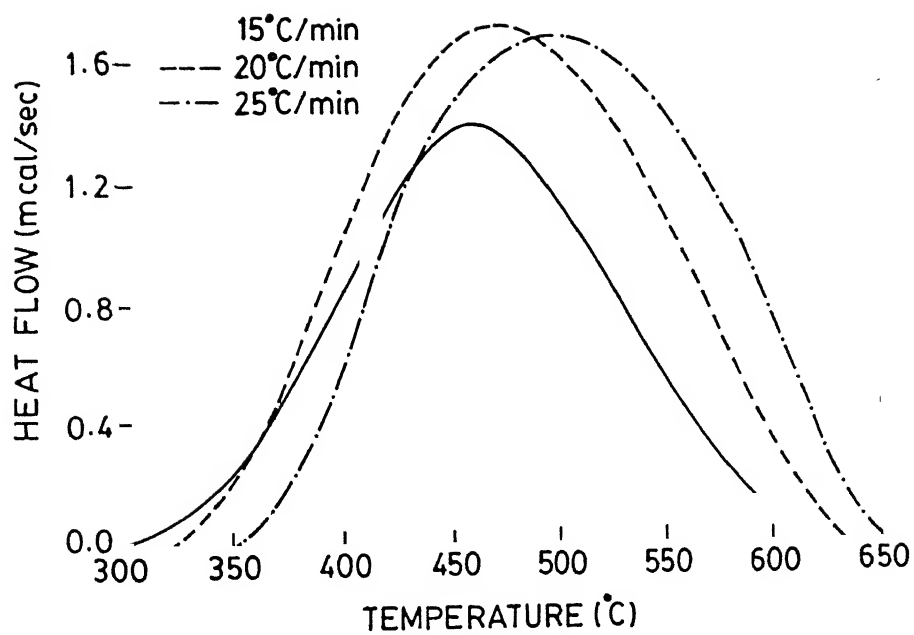
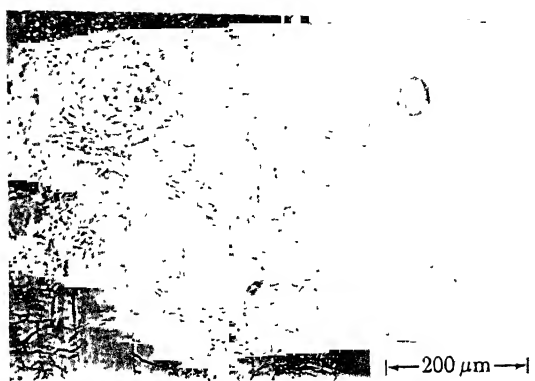
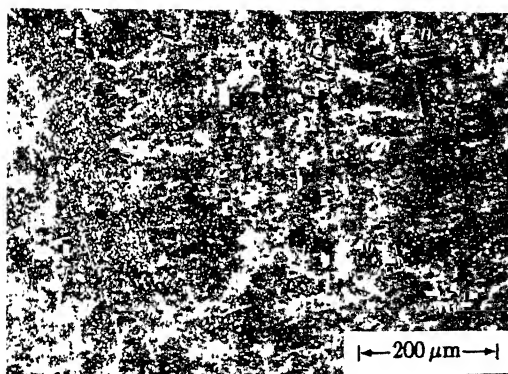


Fig.5.22 : Peak A at different heating rates.



(a)



(b)

Fig.5.23 : (a) Micrograph at the beginning of the peak A;
(b) Micrograph after the peak A.

Table 5.1. : Characteristics of Peak A and total heat effects at different heating rates

Heating Rate (°C/min)	Total heat effect Q (J/gm)	Peak Temperature (°C)		
		Beginning	Maximum	End
15	54.51	302.46	462	621.62
20	58.50	319.95	472	632.35
25	57.30	349.34	501	652.17

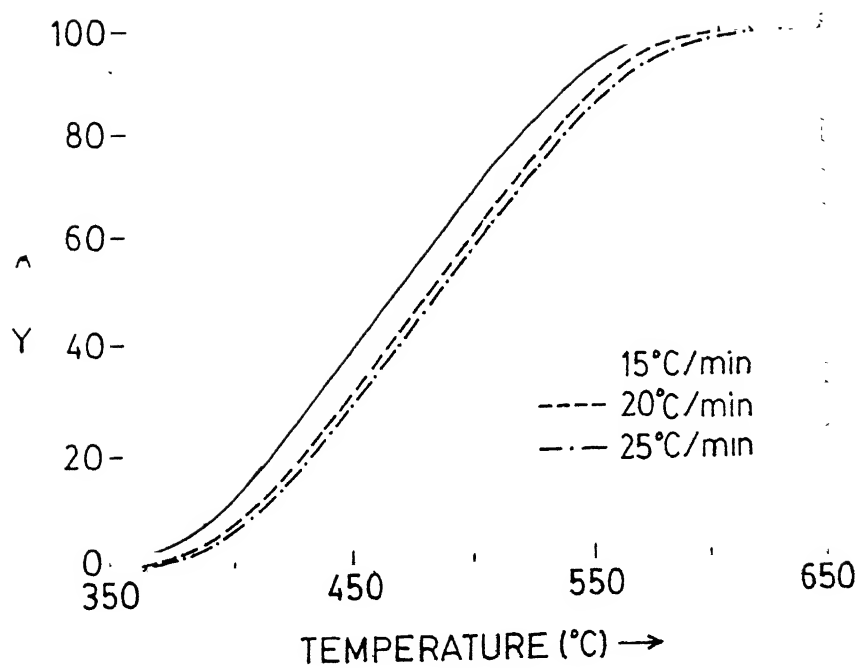


Fig.5.25 : Variation of volume fraction vs T corresponding to peak A.

that reaction can be expressed as

$$\frac{dY}{dt} = f(Y) \cdot k_0 \cdot e^{-Q/RT} \quad \text{.....5.9}$$

where k_0 is the frequency factor, $f(Y)$ is a function of Y only, Q is the activation energy, R is the gas constant and T is the absolute temperature.

The activation energy of this process can be determined by integral technique [115] used for chemical reactions. It follows from the above eqn.5.9 [116]

$$F(Y) = (k_0/\phi) i \quad \text{.....5.10}$$

$$\text{where } F(Y) = \int_0^Y \frac{dY}{f(Y)} \quad \text{and } i = \int_0^T e^{-Q/RT} dT$$

$$\text{Therefore, } \ln [F(Y)/k_0] = \ln i[T, Q] - \ln \phi \quad \text{.....5.11}$$

If at a given heating rate ϕ_j , a given fraction of product Y' is obtained at temperature T_j , then

$$\ln \phi_j - \ln i[T_j, Q] = \ln [F(Y')/k_0] \quad \text{.....5.12}$$

If the temperatures at which the same volume fraction Y' , is obtained at heating rates ϕ_1 and ϕ_2 are T_1 and T_2 , respectively, a function Δ may be defined as

$$\Delta = [\ln \phi_1 - \ln i(T_1, Q)] - [\ln \phi_2 - \ln i(T_2, Q)] \quad \text{.....5.13}$$

where i is a function of T_j and Q . If the rate equations are same for the pair of heating rates, it follows from the eqn.5.13, that $\Delta = 0$.

The values of $\log i$ have been tabulated by Greenhow and Guylai [115] as functions of T and Q . Taking $Y' = 0.5$, Δ was calculated after eqn.5.13 for various values of Q and plotted against Q (Fig.5.26). The value of Q at $\Delta = 0$ is the required activation energy. The average value of Q has been found out to be 130 kJ/mol (31.2 kcal/mol). This value is close to the activation energy for vacancy migration in Ni_3Al as determined by positron annihilation technique [117].

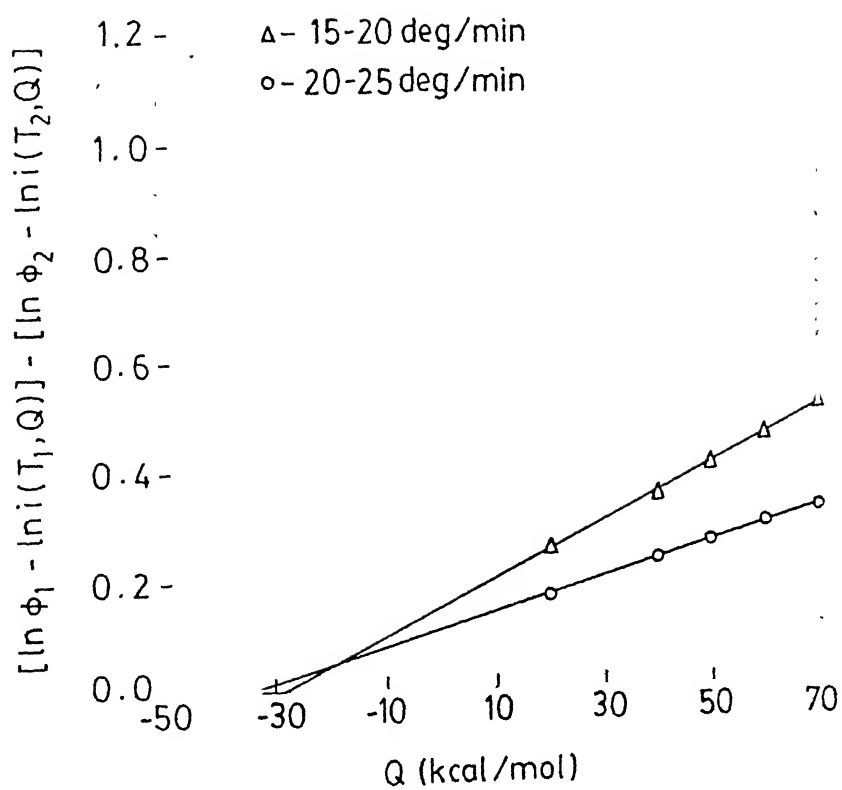


Fig.5.26 : Determination of activation energy by integral technique.

The average enthalpy of the exothermic peak A was measured as 11.5 kJ/mol (56.77 J/gm) which is comparable to the ordering energy of Ni_3Al (50 J/gm), as estimated by Gialanella et al. [118] and within the range of 8 to 14 kJ/mol as estimated by Jang and Koch [17]. The enthalpy value is quite high compared to other intermetallic alloys except $(\text{Fe}_{22}\text{Co}_{78})_3\text{V}$ [118].

The peak A has been associated with change in the structure from DO_{22} to L1_2 . As was noted earlier, the DO_{22} structure can change into L1_2 by simple shuffling of the locations of Al atoms; this essentially means that one kind of order gets replaced by another kind resulting in a change of the structural symmetry. As pointed out earlier, the reordering process starts at around 350°C which corresponds to the beginning of the peak A. Although, at this stage, the ordering is characteristic of the DO_{22} symmetry, with the progress of reaction, order increases and the order parameter S reaches a value of 0.6 at 600°C which means the end of the peak. At this stage, the order corresponds to L1_2 . Because of the cold work, excess vacancies are expected to be present in the matrix; therefore, atomic diffusion involved in the reordering process will be expected to have an activation energy similar to that for vacancy migration, which is 120 kJ/mol in Ni_3Al [117]. This value is close to the activation energy value of 130 kJ/mol, obtained in the present investigation.

5.2. Recrystallization :

5.2.1. Kinetics of Recrystallization :

The recrystallized volume fractions in the 85% cold rolled specimens were measured as a function of time within the temperature range of 800° – 950°C . Fig.5.27 shows the changes in the recrystallization volume fraction, X with recrystallization time (t) at different temperatures. The X vs time curve appears to be a composite of two sigmoidal curves. The sigmoidal shape

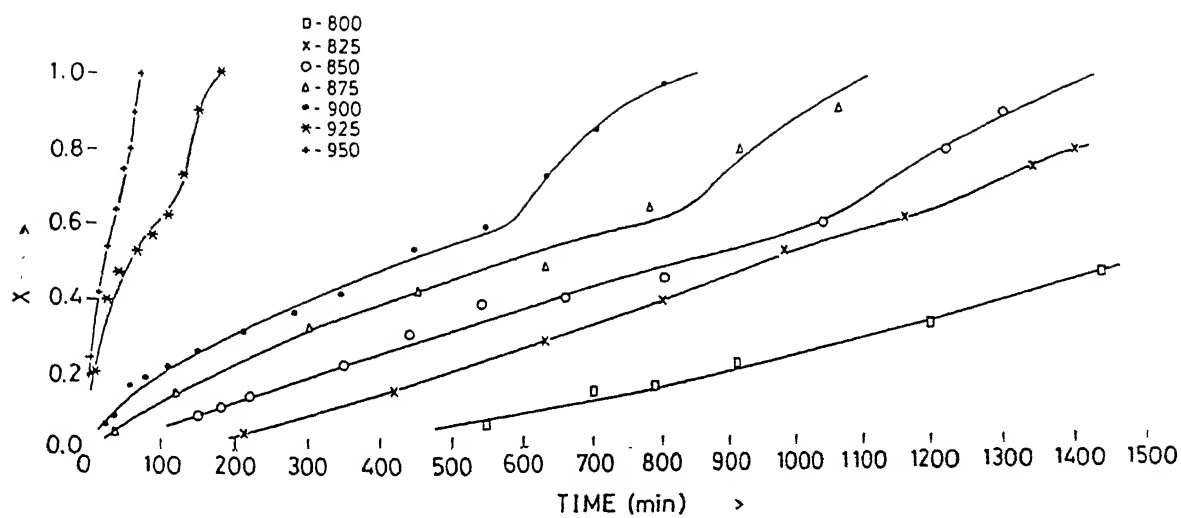


Fig.5.27 : Variation of volume fraction recrystallized with time at various temperatures in $\text{Ni}_{76}\text{Al}_{24}(\text{B})$.

of the curves indicate that the recrystallization process in $\text{Ni}_{76}\text{Al}_{24}(\text{B})$ alloy involves nucleation and growth. As recrystallization is a diffusion controlled phenomenon, the rate of recrystallization increases with increase in temperature. At 825°C , the recrystallization is not complete even after 24 hours of annealing. At temperatures, $825^\circ\text{C} \leq T \leq 900^\circ\text{C}$, recrystallization proceeds at a higher rate and is completed within 24 hours. Above 900°C , the rate is the highest and recrystallization is complete within 3 hours.

The kinetics of recrystallization in a number of materials may be described by the Johnson-Mehl-Avrami equation

$$X = 1 - \exp(-Kt^n) \quad \dots\dots 5.14$$

where X is the fraction recrystallized, K is a temperature dependent constant, t is the time of recrystallization and n is the Avrami exponent. Taking logarithm of both sides in eqn.5.14

$$\ln[\ln \{1/(1-X)\}] = \ln K + n \ln t \quad \dots\dots 5.15$$

$\ln \ln[1/(1-X)]$ has been plotted against $\ln t$ in Fig.5.28. At all the temperatures, a single Avrami exponent describes the data in a satisfactory manner upto $X = 0.6$. However, above $X = 0.6$, another Avrami exponent describes the data satisfactorily. The X vs t curves showing composite sigmoidal behaviour are consistent with the two sets of Avrami exponents. The values of the Avrami exponent are listed in Table 5.2. Below $X = 0.6$, the exponent has the highest value of 2.2 at 800°C but decreases with increase in temperature to 0.71 at 950°C . However, above $X = 0.6$, only a limited number of points have been obtained experimentally at each temperature and these points have been fitted with a straight line having slope of approximately 3. The variation of n with temperature is shown in Fig.5.29 at $X < 0.6$ and $X > 0.6$. Gottstein et al. [70] also investigated the applicability of Johnson-Mehl equation to recrystallization behaviour of 80% cold rolled boron-doped $\text{Ni}_{76}\text{Al}_{24}$ alloy. However, the temperature range studied by them

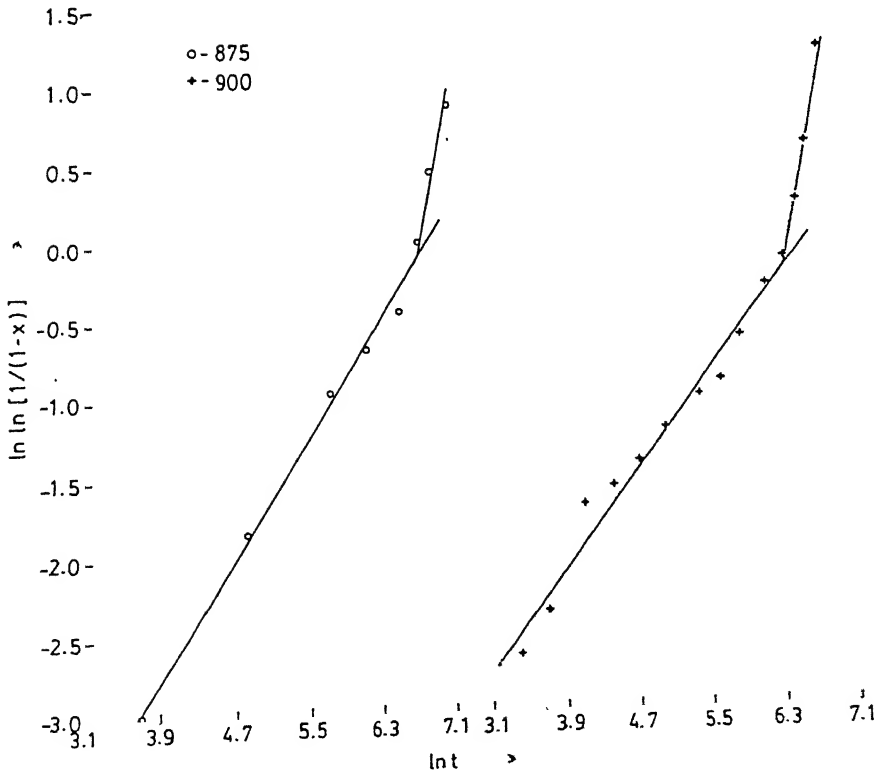
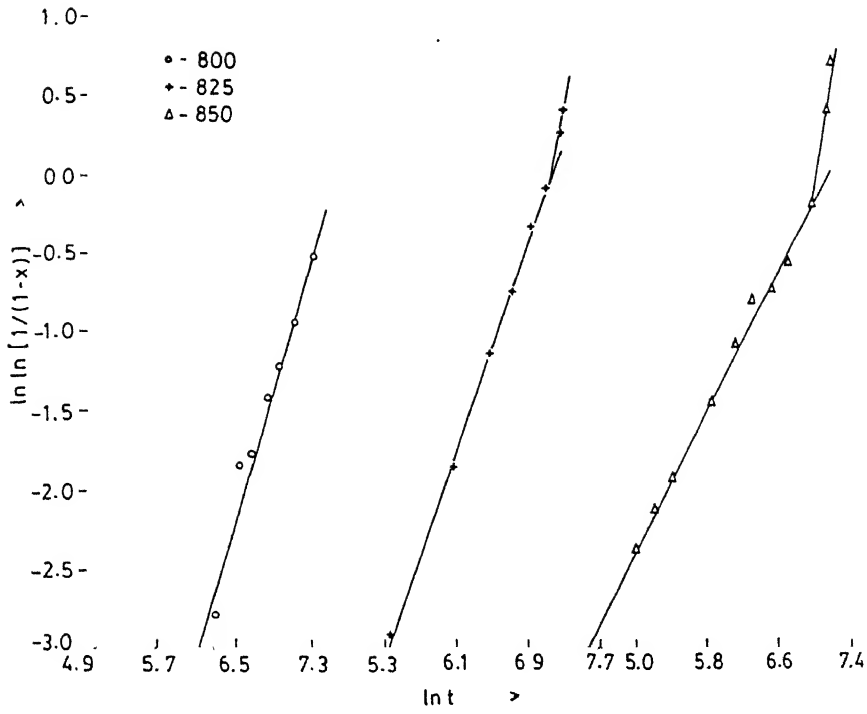


Fig. 5.28

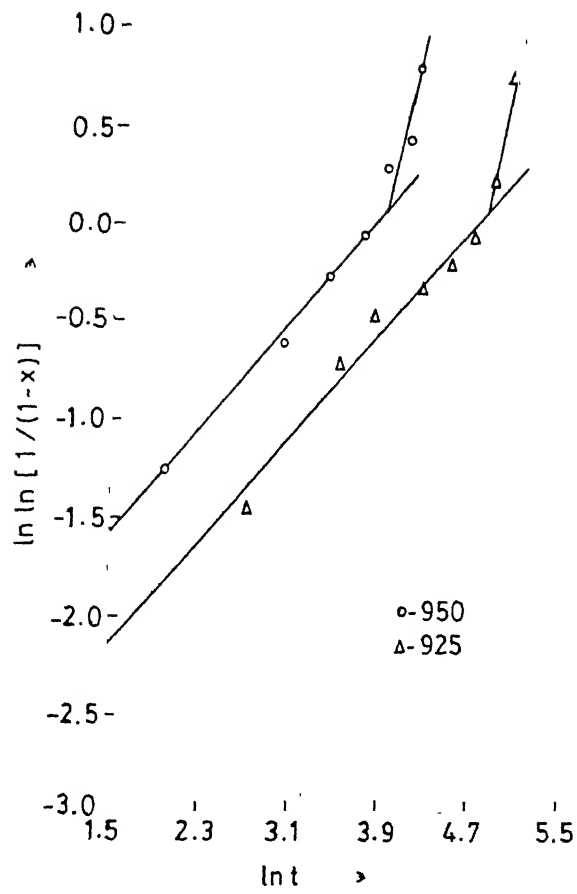


Fig.5.28 : Johnson-Mehl plot for the determination of n and k .

Table 5.2. : Variation of Avrami exponent with temperature and volume fraction

Temperature °C	n volume fraction recrystallized	
	upto 60%	above 60%
800	2.2	
825	1.7	3
850	1.14	3
875	0.96	3
900	0.79	3
925	0.68	3
950	0.71	3

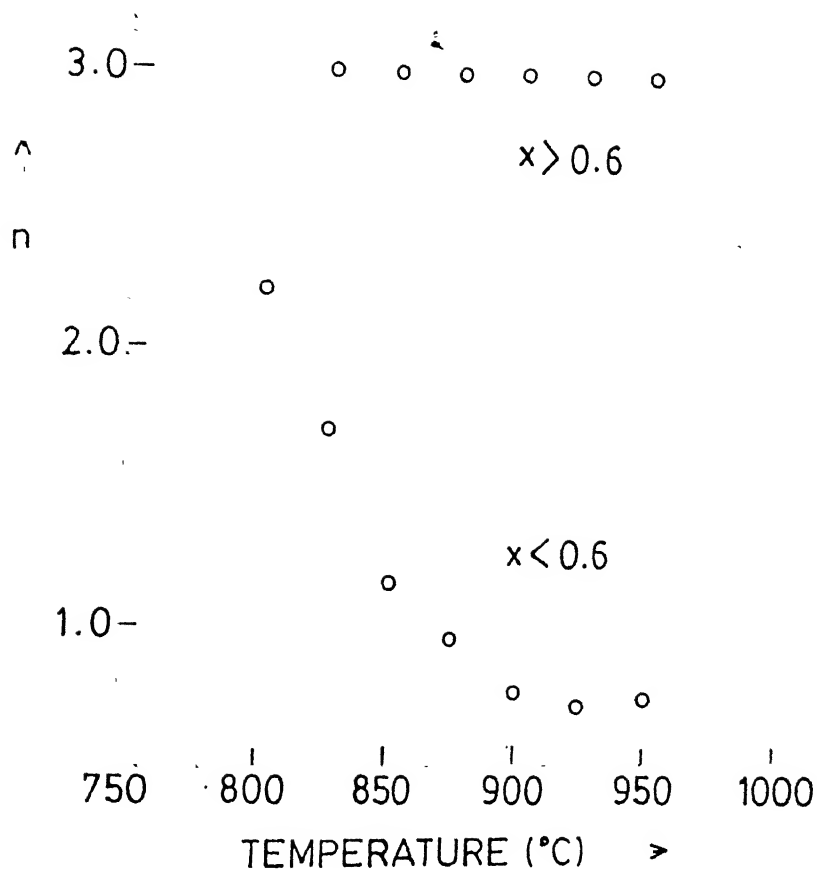


Fig.5.29 : Variation of n with temperature.

was 635° - 675°C. They have reported n value of 2.2 which is also the value obtained for recrystallization at 800°C in the present investigation. Ball and Gottstein [90] have also investigated the recrystallization behaviour of the same alloy in the temperature range of 800° - 1000°C and observed that n decreases from 1.8 to 0.3 with increase in temperature. Thus, the temperature dependence of n has the same trend in this as well as in the present investigation.

The overall rate of transformation can be expressed as

$$\frac{dX}{dt} = f(X) \cdot k_0 \cdot e^{-Q^*/RT} \quad \dots\dots 5.16$$

where $f(X)$ is a function of X only; k_0 is the frequency factor; Q^* is the activation energy; R is the gas constant; and T is the temperature.

The integration of the above equation for a given fraction X_i leads to

$$\ln t_{X_i} = F(X_i) - (Q^*/R)(1/T) \quad \dots\dots 5.17$$

$$\text{where } F(X_i) = \ln k_0 + \ln \int_0^{X_i} \frac{dX}{f(X)} \quad \dots\dots 5.18$$

Thus, a graph of $\ln t_{X_i}$ against $1/T$ should give a value of the activation energy Q^* . Such plots for $X = 0.25, 0.45$ and 0.80 are shown in Fig.5.30. This figure shows that below 900°C, the data points give good least square lines. However, above 900°C, the data points seem to indicate much larger slope. Although the number of data points above 900°C are only two at each value of X , these two points at each X value yield nearly the same slope. The measured activation energies are 450, 440 and 420 kJ/mol at $X = 0.25, 0.45$ and 0.80 , respectively. These three values are very close to each other and yield an average value of 437 kJ/mol. However, the activation energy obtained from the least square lines through data points below 900°C yield values of 200, 145 and 110 kJ/mol at $X = 0.25, 0.45$ and 0.80 , respectively. These values are listed in Table 5.3. The activation energies clearly show that two different

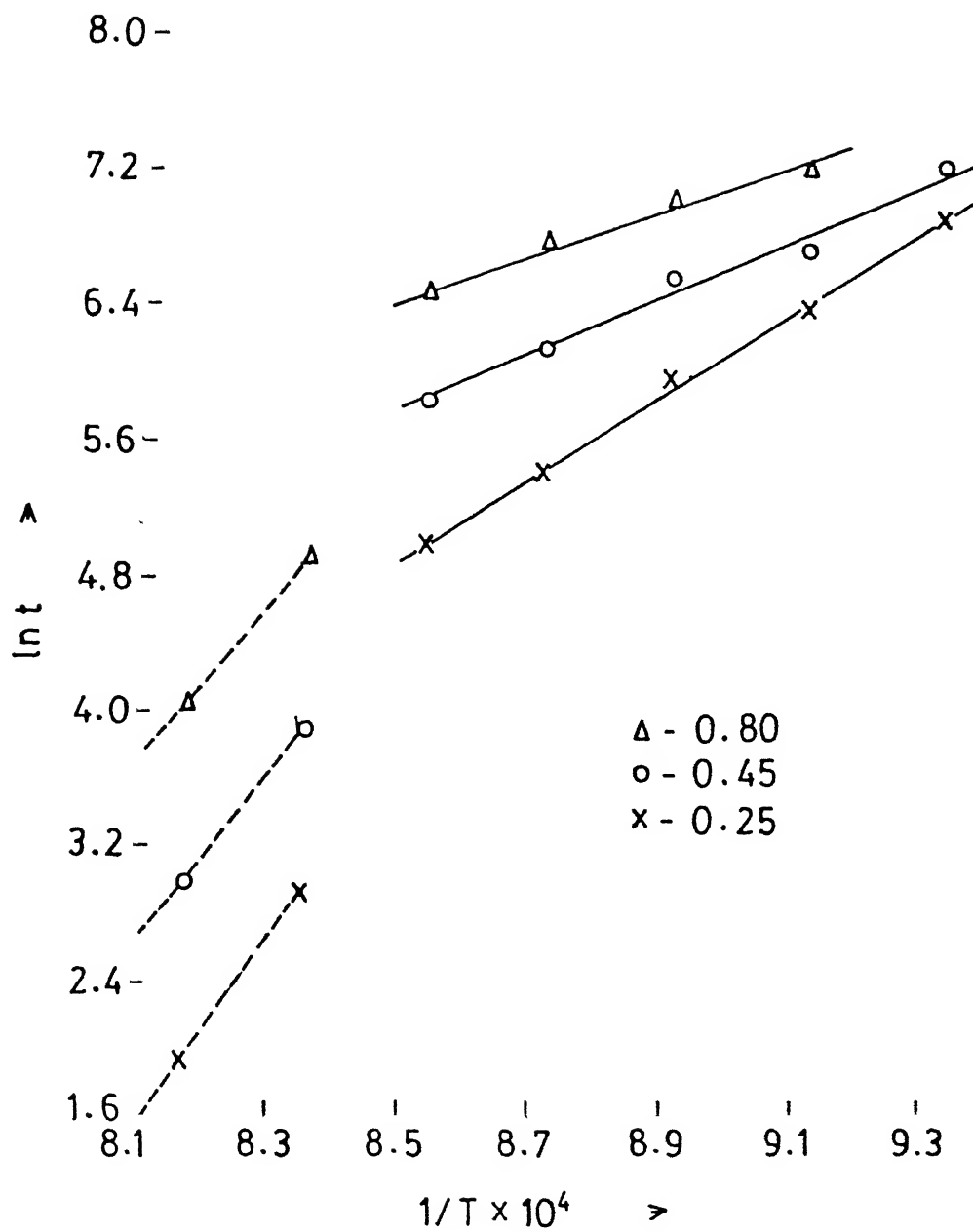


Fig.5.30 : Determination of activation energy by constant fraction technique.

Table 5.3. : Variation of activation energy (Q^*) with volume fraction recrystallized and temperature

Volume fraction recrystallized (X)	Q^* (kJ/mol)	
	below 900 °C	above 925 °C
0.25	200	450
0.45	145	440
0.80	110	420

processes occur during recrystallization. The process having activation energy of about 437 kJ/mol is active at and above 925°C; while, the processes active below 900°C have activation energies which decrease from 200 kJ/mol at $X = 0.25$ to 110 kJ/mol at $X = 0.8$. It is also to be noted that the activation energy plots show discontinuities between 900° and 925°C which is unusual and is normally associated with a phase change. The activation energy for diffusion of Ni in Ni_3Al is known to be 140 kJ/mol below 900°C whereas it becomes more than twice that amount (330 kJ/mol) above 925°C [74]. This is consistent with the present result; since, one of the Q values for recrystallization below 925°C was found to be 145 kJ/mol which is in excellent agreement with that of diffusion of Ni in $\text{Ni}_3\text{Al(B)}$. Similarly, the activation energy of 437 kJ/mol found for the processes above 925°C is also comparable to the activation energy of diffusion of Ni in $\text{Ni}_3\text{Al(B)}$ in that temperature range (more than twice that of low temperature value).

The constant K of eqn. 5.14 may be written as below

$$k = K^{1/n}$$

where k is the rate constant. Therefore,

$$K^{1/n} = k = k_0 \cdot e^{-Q^*/RT}$$

Hence, a plot of $\ln(K^{1/n})$ vs $1/T$ should yield a slope of $(-Q^*/R)$. From the Avrami plot, values of K were taken and $\ln(K^{1/n})$ were plotted against $1/T$ (Fig.5.31). Fig.5.31 shows least square straight lines through the data points. The data points show much higher scatter compared to the data points used in the cross-cut method described earlier. Since, $\ln(K^{1/n})$ vs $1/T$ plots are based on derived data rather than original experimental data, higher scatter in such plots is expected. These yield, below 900°C, values of 151 kJ/mol for $X < 0.6$ and 100 kJ/mol at $X > 0.6$. It may be recalled that the cross-cut technique yielded an average value of 172 kJ/mol for $X < 0.6$ and a value of 100 kJ/mol above $X = 0.6$. Noting that the plots of $\ln(K^{1/n})$ vs $1/T$

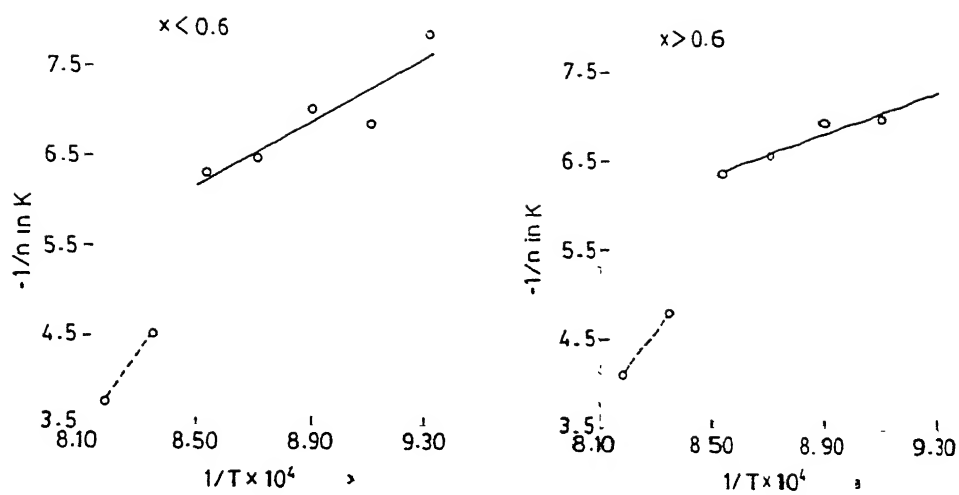


Fig.5.31 : Determination of activation energy by rate constant technique.

yield an average value over the entire mole fraction range and the scatter in these values is expected to be large, the agreement is considered good and they suggest internal consistency of the data.

The literature values of n and Q^* (listed in Table 2.3) indicate that these are likely to be functions of the degree of cold work. However, in the literature, no data is available on the 85% cold rolled material, although Gottstein et al. [70] did some work on 80% cold rolled samples. They reported Q^* value of 120 kJ/mol measured over the temperature range of 635° - 675°C. The n values were measured by them only for two temperatures and the activation energy was determined on the basis of three temperatures i.e. 635°, 650° and 675°C. Therefore, comparison between their data with those of the present investigation can not be straightforward. However, the activation energy of 120 kJ/mol reported by them is close to the value obtained in the present investigation. Similarly, their n value of 2.2, for the temperature range of 650° and 675°C, is close to the value of 2.2 at 800°C in the present case. Other scattered literature data on n and Q^* values, as shown in Table 2.3, although not directly comparable to the conditions of the present investigation, follow the trend which has been observed in the present case.

The activation energy determined in the present case is found to vary with temperature, in fact two sets of Q^* values are obtained over the temperature range investigated.

The average activation energy (Q^*) upto 900°C is found to be 151 kJ/mol. In the literature, the value of Q^* has been measured by a number of workers. The values are 120 kJ/mol at 80% cold rolling within the range of 635° - 675°C [70], 140 kJ/mol at 30% cold rolling within the range of 850° - 925°C [89] and 172.6 kJ/mol at 25% cold rolling within the range 850° - 900°C [89]. These literature values are close to that determined in the present case. None of the previous investigators have examined the variation of X with time closely

enough to notice changes of activation energies. Again, none of them examined the variation of Q^* with volume fraction recrystallized. Similarly, the variation of Q^* with temperature was also not thoroughly examined.

Above 925°C , although Q^* could not be determined accurately, it tends to be more than twice the value at low temperature. Jena et al. [89] reported activation energy of about 230 kJ/mol over the temperature range of 925°C - 975°C for 22% cold rolled material and Zhou et al. [88] have reported a value of 300 kJ/mol for 40% cold rolled material at the temperature range of 850°C to 1000°C . As found in this investigation, these values at temperature above 925°C are much larger than the value reported below 900°C .

Detailed investigations show two sets of n value though Q^* is nearly constant. In the range of $X < 0.6$, n increases with decrease in temperature. The high n value detected at $X > 0.6$ i.e. 3 has not been shown before as literature data on this aspect is scanty. However, decrease in n value with increase in temperature was reported by Gottstein et al. [70]. The n value reported in the literature is within the range of 0.7 - 2.2 and this is similar to the data obtained in the present investigation.

5.2.2. Development of texture :

Texture measurements were undertaken only on the partly and fully recrystallized samples which have been cold rolled by an amount of 85% reduction. The texture after primary recrystallization has been found to be invariably weak (maximum intensity of about $\sim 1.5R$) compared to the texture of the cold rolled material (maximum intensity of $\sim 5R$) which has been reported earlier (Chap.IV). Figs.5.32 and 5.33 show the pole figures as well as the ODFs of fully recrystallized samples, annealed at two different temperatures, namely 850°C and 950°C , respectively. All these figures clearly indicate that the recrystallization texture of this material is very weak, not much above random. Even then some distinct features are discernible in the ODFs. In the

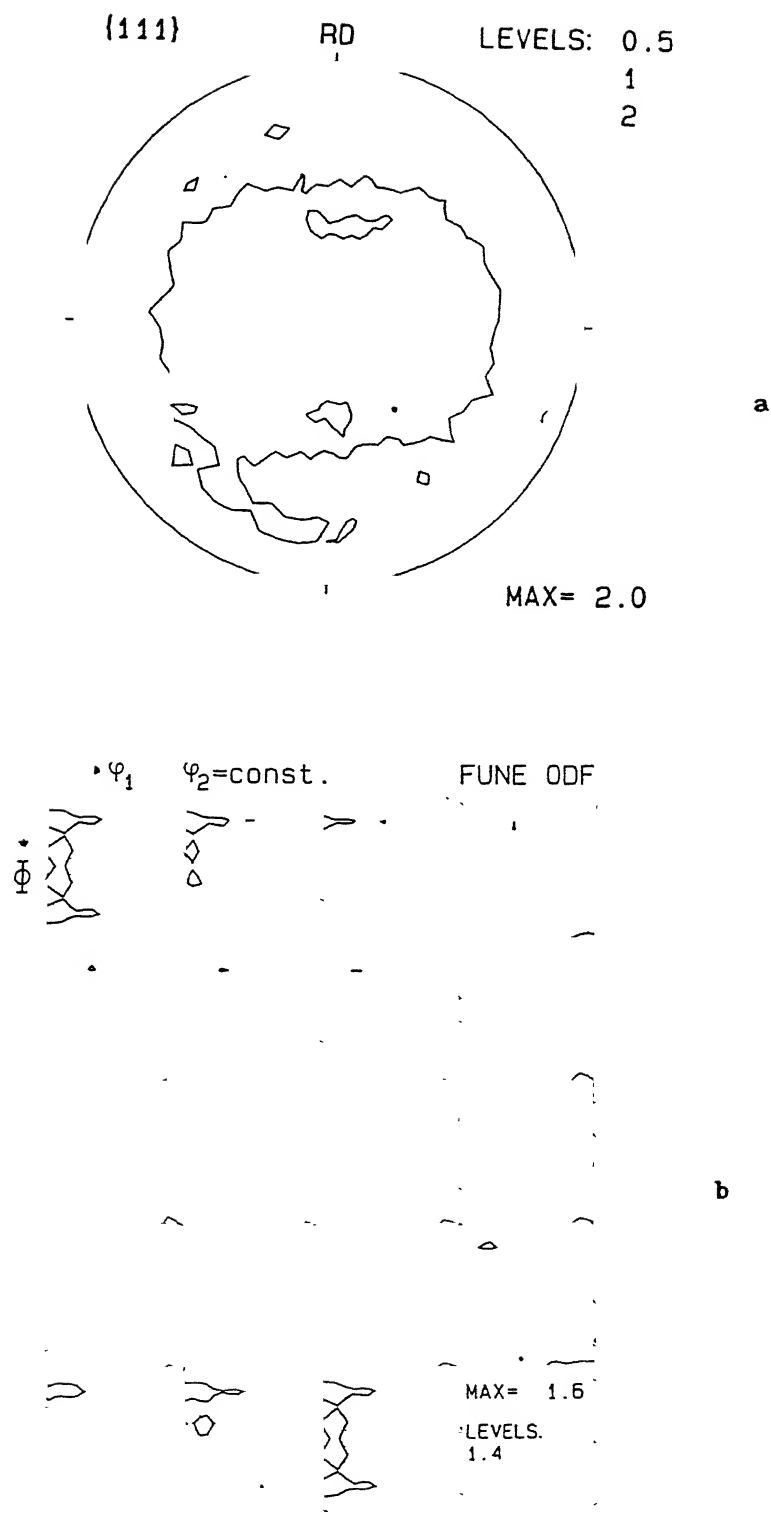


Fig.5.32 : Texture after annealing at 850°C for 17 hr.

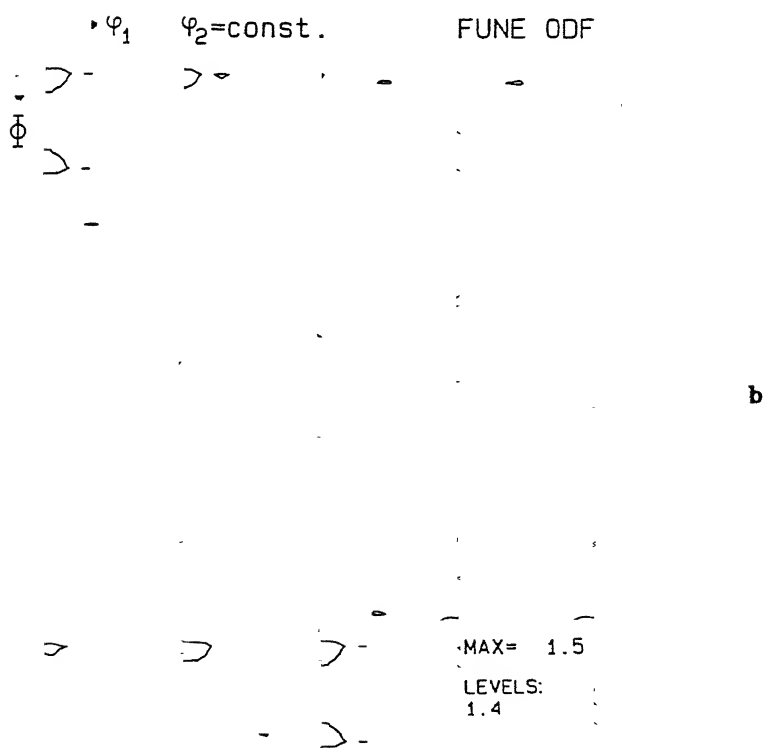
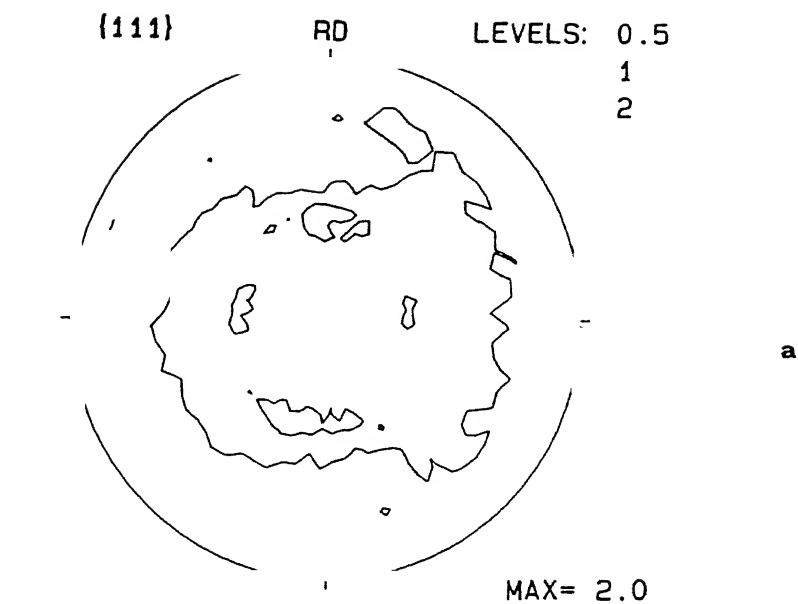


Fig.5.33 : Texture after annealing at 950°C for 1 hr.

ODF of the 850°C annealed material (Fig.5.32), a weak rotated cube {025}<100> component is present along with a weak Goss {011}<100> component. The Goss component {011}<100> seems to have been retained from the rolling texture. The ODF of the sample recrystallized at 950°C, however, shows only the weak rotated cube orientation, but no Goss orientation (Fig.5.33). The Goss orientation develops a bit later in this material, after 48 hours of annealing (Fig.5.34) and there is a considerable amount of scatter around this orientation. The intensity of Goss orientation in this sample is also markedly higher than its intensities in the earlier samples. This clearly indicates that grain growth after primary recrystallization aids in the formation and growth of the Goss oriented regions. The ODF of the alloy, annealed at 1025°C for 1 hour, again shows a Goss component along with rotated cube orientations (Fig.5.35).

The development of recrystallization texture in $\text{Ni}_{76}\text{Al}_{24}(\text{B})$ alloy is very different from that in pure Ni which is known to exhibit a strong cube {100}<001> texture under identical conditions. Both the materials have nearly the same stacking fault energy (SFE) as mentioned in chapter IV. Irrespective of that, the deformation as well as recrystallization textures have been found to be widely different in the two cases. Presumably, factors such as ordering of $\text{Ni}_{76}\text{Al}_{24}(\text{B})$ and the structural changes it undergoes during deformation ($\text{L1}_2 \rightarrow \text{DO}_{22}$) as well as during annealing ($\text{DO}_{22} \rightarrow \text{L1}_2$) far outweigh the effect of SFE in determining the final textures.

In order to understand the effects of the structural change and the change in the order during annealing on texture, a number of 85% cold rolled samples were isothermally annealed at 850°C for 1, 5, 11 and 24 hours. As shown in Fig.5.27 the alloy is yet to start recrystallizing after 1 hour of annealing, only partial recrystallization set in after annealing for 5 and 11 hours, whereas 24 hours of annealing produces slight grain growth beyond

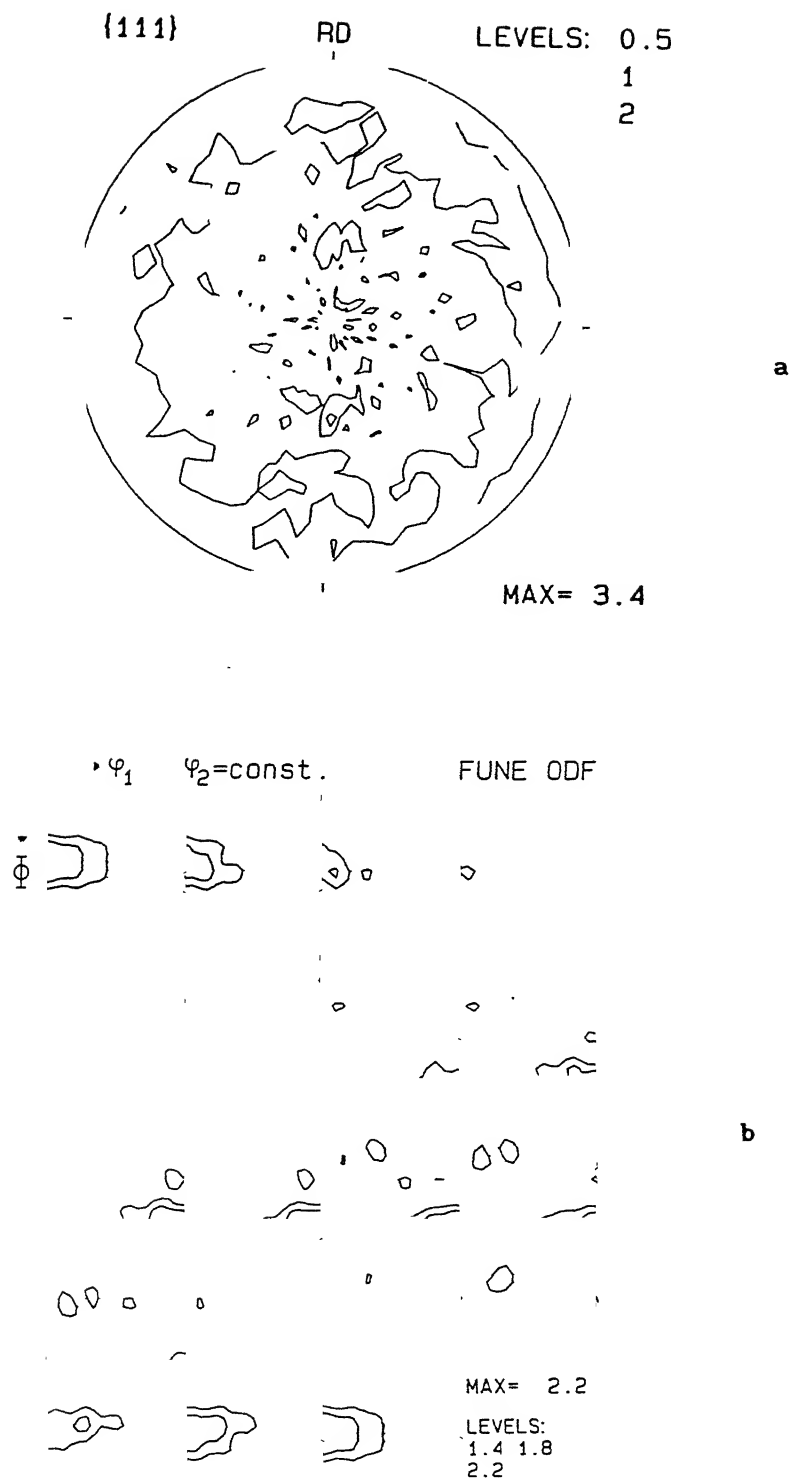


Fig.5.34 : Texture after annealing at 950°C for 48 hrs.

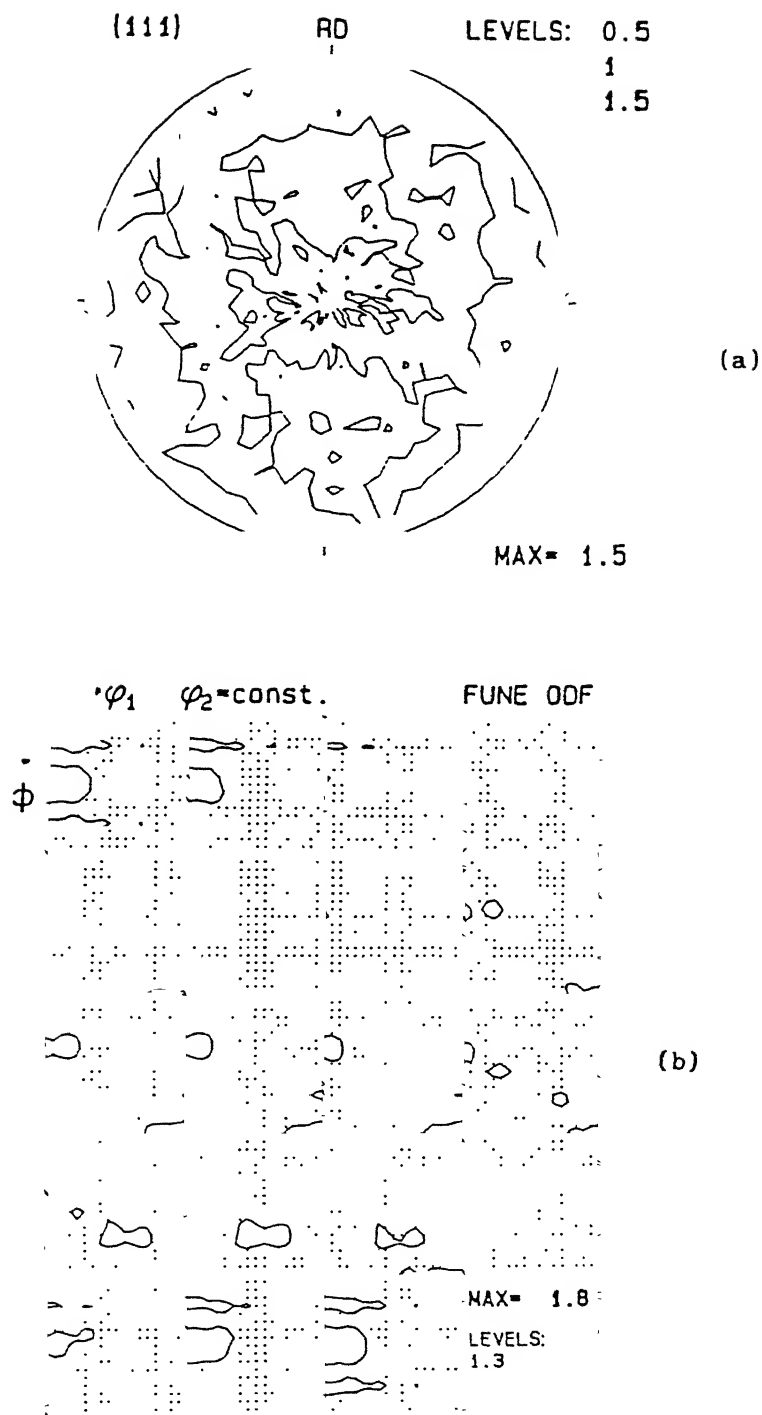


Fig.5.35 : Texture after annealing at 1025°C for 1 hr.

completion of recrystallization.

The ODFs of these four samples annealed for 1, 5, 11 and 24 hours at 850°C are presented in Fig.5.36 (a-d). All these ODFs are found to be essentially similar in the sense that all are very weak, much weaker than the ODF of the 85% cold rolled material (Fig.4.9). The reproducible textural components after 1 hour of annealing are $\{025\}\langle 100\rangle$ and $\{102\}\langle 201\rangle$. After 5 hours, a weak near-Goss component $\{011\}\langle 311\rangle$ is also observed in addition to the above components. After 11 hours of annealing, all the previous components are obtained, but here the near-Goss component $\{011\}\langle 311\rangle$ is found to be the most intense which has the ideal Goss component also in its spread. There is basically no difference between this ODF and the one obtained for the 24 hour annealed material.

The 1 hour annealed sample represents only a recovery stage; however, the S parameter has been found to increase from zero (after 85% cold rolling) to a value of 0.62 at this stage (Fig.5.3). Thus, the observed texture is due not to any reorientation of grains as happens during recrystallization, but to some possible structural reordering. In a sense, this may be termed as a kind of 'transformation' texture produced by structural transformation from DO_{22} (of the highly deformed material) to L1_2 during annealing.

Several aspects need to be considered in order to explain the results of the annealing texture measurements. The first pertains to the fact that a very weak texture is produced from the sharp cold rolling texture during the 'recovery' stage, which does not involve any reorientation of the grains. However, at this stage substantial atomic shuffling is expected to take place which leads to the formation of the parent L1_2 structure from the DO_{22} , the end structure after cold rolling. It is known that the DO_{22} structure can be derived from the L1_2 by the introduction of a $1/2[110]$ APB on every $\{001\}$ plane $[112]$. Similarly, the introduction of an APB on every (001) plane in

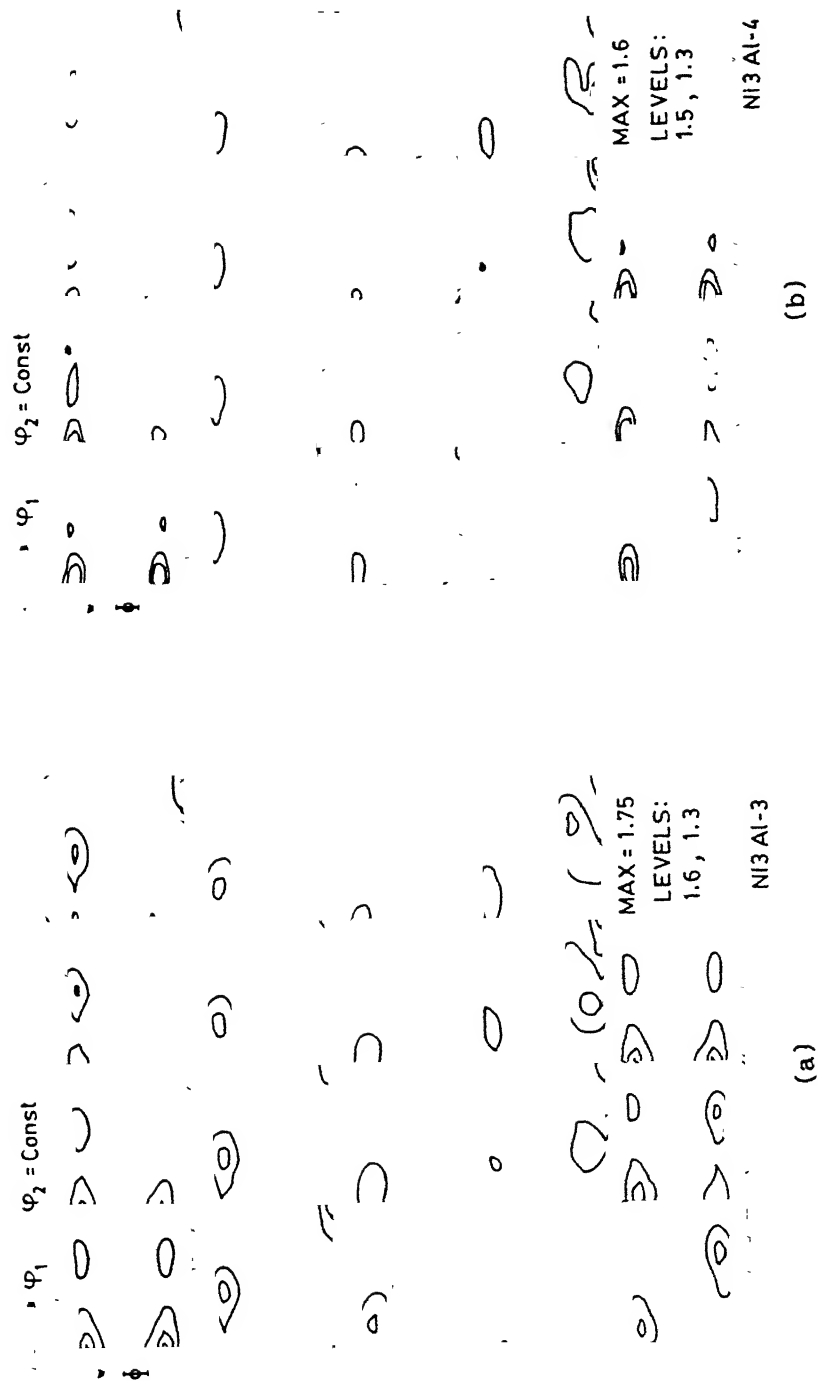


Fig. 5.36

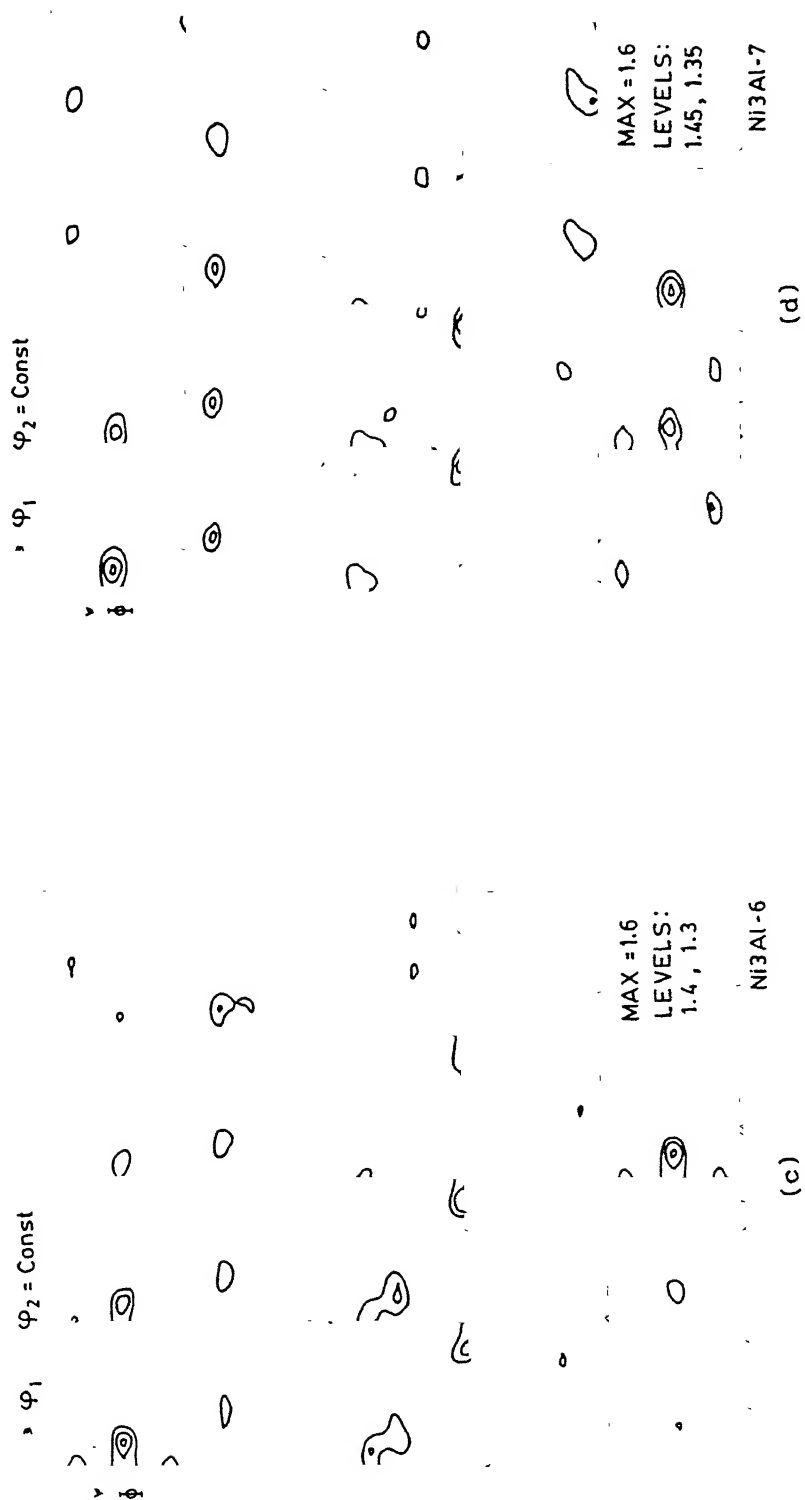


Fig.5.36 : Development of texture at 850°C : (a) 1 hr, (b) 5 hrs, (c) 11 hrs and (d) 24 hrs.

the DO_{22} structure again transforms it back into the $L1_2$ structure [112]. It may be recalled (Fig.4.8) that during cold rolling of the experimental alloy, the pole density maxima in the pole figures increases from a value of 2.7 (at 25% deformation) to a value of 8.6 (at 45% deformation), then decreases to a value of 4.3 (at 65% deformation), finally decreasing to 3.9 (at 85% deformation). The corresponding $f(g)_{\max}$ values read out from the ODFs of the cold rolled alloy are 2.6, 5.5, 4.6 and 4.8, respectively. This behaviour can be explained as follows. When the $L1_2$ structure is cold rolled, the material acquires a deformation texture whose intensity increases with increasing amounts of cold deformation. After a critical amount of cold work ($\sim 65\%$) the $L1_2$ structure appears to change into DO_{22} which will be accompanied by a transformation induced plasticity. The material will appear softer and further cold work will once again increase the texture intensity (Fig.4.23). The drastic weakening of the texture intensity after 1 hour annealing at 850°C [$f(g)_{\max} = 1.7$] from that of the 85% cold rolled alloy [$f(g)_{\max} = 4.8$] can not be related to any reorientation of grains (since no recrystallization takes place at this stage), but, on the other hand, could be related to the $DO_{22} \rightarrow L1_2$ reverse transformation.

It may be recalled that the initial stages of annealing was found to be associated with the presence of a large density of twin like features (Fig.5.15). Tanner and Ashby [119, 120] made a theoretical analysis of the relief of strains associated with certain phase transformations in intermetallic alloys, such as Ni_3V which has a DO_{22} structure at room temperature. According to them, when ordering in a binary alloy involves a change in crystal symmetry, the reaction is invariably accompanied by an accumulation of substantial internal strains. Under certain conditions, these strains can be relieved through twinning of the product phase. Thus, the twin like features obtained in the product phase after annealing in the present

$\text{Ni}_{76}\text{Al}_{24}(\text{B})$ alloy can be assumed to be due to such an effect. It has been shown above (Fig.5.21) that during annealing, the heat evolution before recrystallization is quite substantial (11.5 kJ/mol). A major part of this energy has been attributed to the $\text{DO}_{22} \rightarrow \text{L1}_2$ reverse transformation. This clearly indicates that significant relief of strain is associated with this transformation and it is no wonder, therefore, that a high density of twins accompany this transformation. The incidence of twinning will lead to the fragmentation of the grains, resulting in weakening of the texture.

The weak texture obtained after annealing for 1 hour at 850°C continues as it is, during progressive annealing upto 5, 11, 17 and 24 hours, i.e. during the stages of partial recrystallization to full recrystallization, continuing even upto the grain growth stage. Very weak recrystallization texture in $\text{Ni}_3\text{Al}(\text{B})$ has also been reported by Ball and Gottstein [90]. The almost random recrystallization texture in this alloy has been attributed by them to the high nucleation rate and the low grain boundary mobility, which produces a lack of growth selection during recrystallization. Using this argument it is difficult to reason out why the recrystallization texture should be so very weak compared to the cold rolling texture and at the same time why it should not bear any resemblance at all with the essential features of the cold rolling texture. On the basis of the present investigation, however, it may be suggested that when recrystallization starts during annealing, the sharp cold rolling texture has already been replaced by a weak 'transformation' texture; as a result the recrystallization has been an essentially *in-situ* phenomenon resulting in the formation of a weak texture.

Of all the orientations observed in the ODFs of the alloy during partly or fully recrystallized conditions, the Goss component $\{011\}\langle 100 \rangle$ appears to be the most prominent. It is known that this component usually originates in

deformation/shear bands. In the present alloy, formation of shear bands started from 65% cold rolling onwards and the density of such bands increased significantly after 85% cold work (Fig.4.4). It may be recalled here that a large number of $\{110\}$ oriented regions could be detected in the thin foils made from partly and fully recrystallized material.

5.3. Evolution of texture and structure during annealing :

On the basis of the present investigation, it may be suggested that the annealing process comprises of three different phenomena: (a) recovery of DO_{22} structure; (b) restoration of $L1_2$ structure and (c) recrystallization.

During annealing, initially recovery takes place without any significant change in order. Later on, the DO_{22} structure reverts back to $L1_2$ in two stages : Stage I occurs at lower temperatures (200° – 400° C) where the S value increases at a fast rate and Stage II occurs at higher temperatures (500° – 800° C) where S increases gradually. The formation of the $L1_2$ structure from the DO_{22} matrix requires the local rearrangement of atoms on the existing lattice sites of the DO_{22} phase. The observed weakening of the texture during recovery stage can be attributed to the formation of high density of twins in the product phase ($L1_2$) which will have the effect of fragmenting the grains.

Recrystallization occurs by the nucleation of large number of strain-free grains and sluggish growth of the grain boundaries. The high nucleation rate coupled with limited growth is likely lead to the starting texture before recrystallization to be retained after the process is complete. This explains why a very weak recrystallization texture is obtained in this material.

CHAPTER VI

SUMMARY AND CONCLUSIONS

The material used in the present investigation was a hypostoichiometric polycrystalline boron-doped $\text{Ni}_{76}\text{Al}_{24}$ alloy. The as-received material was annealed at 1050°C for 25 min. to produce an average grain size of 25-30 μm . The alloy was cold rolled and subsequently annealed. Microstructural analysis of homogenized, cold rolled as well as annealed samples were done by optical and transmission electron microscopy. The lattice parameter as well as the order parameter and strain parameter were measured using X-ray diffraction. Texture determination was done by ordinary pole figures as well as by ODF method. The salient conclusions of the present investigation are enumerated below :

1. Progressive cold rolling of $\text{Ni}_{76}\text{Al}_{24}(\text{B})$ decreases the order parameter (S), calculated from (100)/(200) pair of reflections, to zero after 65% deformation. However, the value of S calculated from (110)/(220) pair of reflections first decreases, then attains a value of 0.4 after 65% deformation and remains constant till upto 90% deformation.
2. The above results coupled with the observed changes in hardness, resistivity, strain parameter and microstructure indicate a structural change from L1_2 to DO_{22} . The lattice parameters of the product structure are $a = 3.567\text{\AA}$ and $c = 7.188\text{\AA}$.
3. Due to structural change from L1_2 to DO_{22} (at around 65% deformation), the deformation mode of the alloy changes from normal slip to twinning. As a result, the texture changes from pure metal type to alloy type.
4. The pure metal type texture of the alloy is characterized mainly by the Cu component $\{112\}\langle 111 \rangle$, the B_S component $\{110\}\langle 112 \rangle$ and the S component

{123}<634>. The alloy type texture obtained after 65% deformation is characterized by mainly the B_s component, the Goss component {011}<100> and the rotated Goss component {110}<011>.

5. The change in texture in this alloy with progressive deformation appears to take place due to normal octahedral slip followed by twinning. Part of the B_s component is likely to rotate towards the rotated Goss position due to shear banding.

6. Microstructural observations reveal the presence of nearly straight dislocation lines for lower amount of deformation. After heavy deformation, a high density of twins are observed throughout the material together with microbands and shear bands.

7. During annealing of the heavily cold rolled material, a combination of three phenomena is found to occur, namely, recovery, reversion of DO_{22} structure to $L1_2$ and recrystallization.

8. Restoration of $L1_2$ structure from DO_{22} occurs in two stages, namely, stage I at low temperature ($200^\circ - 400^\circ\text{C}$) where the kinetics is fast and stage II ($500^\circ - 800^\circ\text{C}$) where the kinetics is slow. The activation energy for reversion of DO_{22} structure to $L1_2$ is 130 kJ/mol which is close to the activation energy for vacancy migration in Ni_3Al .

9. The change over from the DO_{22} to $L1_2$ structure appears to be accompanied by the operation of a multiplicity of variants resulting in drastic decrease of the cold rolling texture during the earlier stages of annealing. The weakening of this texture may also be partly due to the occurrence of twins in the product phase caused by the transformation strain.

10. Once the $L1_2$ structure is nearly fully restored, recrystallization takes place which seems to follow the Johnson-Mehl-Avrami equation. The Avrami exponent, n , decreases with temperature from 2.2 at 800°C to 0.71 at 950°C for recrystallized volume fraction (X) < 0.6. Above X > 0.6, the value

of n remains constant at approximately 3.

11. The calculated activation energy values are found to vary with X below 900°C [$Q = 200, 145$ and 110 kJ/mol at $X = 0.25, 0.45$ and 0.80 , respectively]. Above 925°C , the activation energy is found to be more than twice that observed at lower temperatures.

12. The recrystallization texture is found to be almost random and is very similar to the initial annealing texture obtained after recovery and structural change from DO_{22} to L1_2 . A nearly random starting texture, a high nucleation rate and lower migration rate of the boundaries appear to produce the observed weak recrystallization texture. The recrystallization texture components are $\{025\}\langle 100 \rangle$ and $\{011\}\langle 100 \rangle$ out of which the Goss component $\{011\}\langle 100 \rangle$ is the most prominent one. The textural change correlates well with the microstructural observations.

13. The development of nearly random texture during high temperature recrystallization and the microstructural stability of the alloy will enhance its ability to be used as a high temperature structural material.

REFERENCES

1. K.Aoki and O.Izumi, J.Jpn.Inst.Met., 43, 1190 (1977).
2. C.T.Liu, C.L.White and J.A.Horton, Acta Metall., 33, 213 (1985).
3. O.Izumi, Trans JIM, 30, 627 (1989).
4. S.Hanada, T.Ogura, S.Watanabe, O.Izumi and T.Masumoto, Acta Metall., 34, 13 (1986).
5. M.Hansen and K.Anderko, Constitution of Binary Alloys, McGraw Hill Book Company, New York, 118 (1958).
6. R.W.Guard and J.H.Westbrook, Trans. AIME, 215, 871 (1959).
7. C.L.Corey and B.Lisowskey, Trans. AIME, 239, 239 (1967).
8. G.R.Stoeckinger and J.P.Newmann, J.Appl.Cryst., 3, 32 (1970).
9. D.P.Pope and J.L.Garin, J.Appl.Cryst., 10, 14 (1977).
10. N.Masahashi, T.Takasugi and O.Izumi, Acta Metall., 36, 1815 (1988).
11. O.Noguchi, Y.Oya and T.Suzuki, Metall. Trans., 12A, 1647 (1981).
12. R.Ramesh, R.Vasudevan, B.Pathiraj and B.H.Kolster, J.Mater.Sci., 27, 270 (1992).
13. M.Yamaguchi and Y.Umakoshi, Prog.Mater.Sci., 34, 1 (1990).
14. J.A.Horton, I.Baker and M.H.Yoo, Phil.Mag., A63, 319 (1991).
15. C.L.Corey and D.I.Potter, J.Appl.Phys., 38, 3894 (1968).
16. J.P.Clark and G.P.Mohanty, Scripta Metall., 8, 959 (1974).
17. J.S.C.Jang and C.C.Koch, J.Mater.Res., 5, 498 (1990).
18. S .Gialanella, R.W.Cahn, J.Malagelda, S.Surinach and M.D.Baro, Kinetics of Ordering Transformation in Metals, eds. H.Chen and V.K. Vasudevan, 161 (1992).
19. I.Baker, D.V.Viens and E.M.Schulson, J.Mat.Sci., 19, 1799 (1984).
20. J.Ball and G.Gottstein, Intermetallics, 1, 171 (1993).
21. P.Veyssi re and J.Douin, Phil.Mag.Lett., 51, L1 (1985).

22. J.Douin, P.Veyssière and P.Beauchamp, *Phil.Mag.*, A54, 375 (1986).
23. S.M.Foiles and M.S.Daw, *J.Mater.Res.*, 2, 5 (1987).
24. S.P.Chen, A.F.Voter and D.J.Srolovitz, *Scripta Metall.*, 20, 1389 (1986).
25. K.J.Hemker and M.J.Mills, *Phil. Mag.*, A68, 305 (1993).
26. K.J.Hemker and M.J.Mills, *ibid*, cf Fu, Ye and Yoo (1992).
27. A.T.Paxton, *Electron Theory and Alloy Design*, eds. D.Pettifor and A.Cottrell, Oxford Alden Press, 158 (1992).
28. P.Veyssière, J.Douin and P.Beauchamp, *Phil.Mag.*, A51, 469 (1985).
29. I.Baker and E.M.Schulson, *Phys.Stat.Sol.(a)*, 89, 163 (1985).
30. P.Beauchamp, J.Douin and P.Veyssière, *Phil.Mag.*, A55, 565 (1987).
31. I.Baker, E.M.Schulson and J.A.Horton, *Acta Metall.*, 35, 1553 (1987).
32. L.M.Hsiung and N.S.Stoloff, *MRS Symp.Proc.*, 133, 261 (1989).
33. W.Yan, I.P.Zones and R.E.Smallman, *Scripta Metall.*, 21, 1511 (1987).
34. P.Veyssière, M.H.Yoo, J.A.Horton and C.T.Liu, *Phil.Mag.Lett.*, 57, 17 (1988).
35. M.H.Yoo, *J.Mater.Res.*, 4, 50 (1989).
36. P.A.Flinn, *Trans.AIME*, 218, 145 (1960).
37. B.H.Kear and H.G.F.Wilsdorf, *Trans.AIME*, 224, 382 (1962).
38. S.Takeuchi and E.Kuramoto, *Acta Metall.*, 21, 415 (1973).
39. C.Lall, S.Chin and D.P.Pope, *Metall.Trans.*, 10A, 1323 (1979).
40. V.Paider, D.P.Pope and V.Vitek, *Acta Metall.*, 32, 435 (1984).
41. M.H.Yoo, *Acta Metall.*, 35, 1559 (1987).
42. P.Veyssière, *Phil.Mag.*, A50, 189 (1984).
43. E.Kuramoto and D.P.Pope, *Acta Metall.*, 26, 207 (1978).
44. Y.Q.Sun and P.M.Hazzledine, *Phil.mag.*, A58, 603 (1988).
45. D.Caillard, N.Clement, A.Couret, P.Lours and A.Coujou, *Phil. Mag. Lett.*, 58, 263 (1988).

46. M.J.Mills, N.Baluc and H.P.Karntaler, MRS Symp. Proc., 133, 203 (1989).
47. R.G.Davies and N.S.Stoloff, Trans.AIME, 233, 714 (1965).
48. S.S.Ezz, D.P.Pope and V.Paider, Acta Metall., 30, 921 (1982).
49. P.H.Thornton, R.G.Davies and T.L.Johnston, Metall.Trans., 1A, 207 (1970).
50. T.Takasugi and O.Izumi, Acta Metall., 33, 1247 (1985).
51. A.I.Taub and C.L.Briant, MRS Symp.Proc., 81, 343 (1987).
52. A.H.King and M.H.Yoo, Scripta Metall., 21, 1115 (1987).
53. V.Vitek, J.J.Kruisemana and J.Th.M.DeHosson, Interfacial Structure, Property and Design, eds. M.H.Yoo et al., 139 (1988).
54. A.Chiba, S.Hanada and S.Watanabe, Acta Metall., 39, 1799 (1991).
55. O.Izumi and T.Takasugi, J.Mater.Res., 3, 426 (1988).
56. J.J.Kruiseman, V.Vitek and J.Th.M.De Hosson, Acta Metall., 36, 2729 (1988).
57. J.R.Rice, The Effect of Hydrogen on the Behaviour of Metals, AIME, New York, 455 (1976).
58. E.M.Schulson, T.P.Weihs, I.Baker, H.J.Frost and J.A.Horton, Scripta Metall., 19, 1497 (1985).
59. E.M.Schulson, T.P.Weihs, I.Baker, H.J.Frost and J.A.Horton, Acta Metall., 34, 1395 (1986).
60. E.M.Schulson, I.Baker and H.J.Frost, MRS Symp.Proc., 81, 195 (1987).
61. I.Baker and E.M.Schulson, Scripta Metall., 23, 1883 (1989).
62. H.Kung, D.R.Masmussen and S.L.Sass, Scripta Metall. Mater., 25, 1277 (1991).
63. J.Zhu, Z.Y.Cheng and D.X.Zou, Scripta Metall. Mater., 24, 439 (1990).
64. H.R.Pak and O.T.Inal, J.Mater.Sci., 22, 1945 (1987).
65. T.Takasugi, O.Izumi and N.Masahashi, Acta Metall., 33, 1259 (1985).

66. J.Mukhopadhyaya, G.C.Kaschner and A.K.Mukherjee, Superplasticity in Aerospace II, 19-22 February, 1990 (1990).
67. N.S. Stoloff and I.L. Dillamore, Ordered Alloys, Structural Applications and Physical Metallurgy, eds. B.H.Kear, C.T.Sims, N.S. Stoloff and J.H.Westbrook, Claitor Publishing Divison, Baton Range, LA, 525 (1970).
68. E.M.Schulson, COSAM Program Overview, NASA TN-8300006, Washington, DC, 175 (1982).
69. W.B.Hutchinson, F.M.C.Besag and C.V.Honess, Acta Metall., 21, 1685 (1973).
70. G.Gottstein, P.Nagpal and W.Kim, Mater.Sci.& Engg., A108, 165 (1989).
71. G.F.Hancock, Phys.Stat.Sol.(a), 7, 535 (1971).
72. M.B.Bronfin, G.S.Bulatov and I.A.Drugova, Fiz.Met.Metalloved., 40, 363 (1975).
73. K.Aoki and O.Izumi, Phys.Stat.Sol.(a), 32, 657 (1975).
74. K.Hoshino, S.J.Rothman and R.S.Averback, Acta Metall., 36, 1271 (1988).
75. A.Dasgupta, L.C.Smedskjaer, D.C.Legnini and R.W.Siegel, Mater. Lett., 3, 457 (1985).
76. Jian Sun and Dongliang Lin (T.L.Lin), Acta Metall.Mater., 42, 195 (1994).
77. L.N.Larikov, V.V.Geichenko and V.M.Fal'chenko, Diffusion Processes in Ordered Alloys, National Bureau of Standards and National Science Foundation, Armerind Publishing Co., New Delhi, 117 (1981).
78. T.C.Chou and Y.T.Chou, MRS Symp. Proc., 39, 461 (1985).
79. H.Yasuda, H.Nakajima and M.Koiwa, Defect and Diffusion Forum, 95-98, 823 (1993).

80. R.W.Cahn, High Temperature Aluminides and Intermetallics, eds. S.H. Whang, C.T.Liu, D.P.Pope and J.O.Stiegler, TMS, 245 (1990).
81. B.Roessler, D.T.Novick and M.B.Bever, Trans.AIME, 227, 985 (1963).
82. A.L.Ward and D.E.Mikkola, Metall.Trans., 3A, 1479 (1972).
83. M.Feller-Kniepmeier and F.Rückert, Z.Metallkde, 66, 427 (1972).
84. A.E.Vidoz, D.P.Lazarevic and R.W.Cahn, Acta Metall., 11, 17 (1967).
85. T.Takasugi and O.Izumi, Acta Metall., 33, 49 (1985).
86. M.Gagné and E.M.Schulson, Metall.Trans., 7A, 1975 (1976).
87. R.W.Cahn, M.Takeyama, J.A.Horton and C.T.Liu, J.Mater.Res., 6, 57 (1991).
88. B.Zhou, Y.T.Chou and C.T.Liu, Intermetallics, 1, 217 (1993).
89. A.K.Jena, S.S.Sahay and R.P.Mathur, Structural Intermetallics, eds. R.Darolia, J.J.Lewandowski, C.T.Liu, P.L.Martin, D.B.Miracle and M.V.Nathal, TMS, 425 (1993).
90. J.Ball and G.Gottstein, Intermetallics, 1, 191 (1993).
91. B.D.Cullity, Elements of X-ray Diffraction, Addison-Weisely (1978).
92. M.Hatherly and W.B.Hutchinson, An Introduction to Textures in Metals, London, The Institution of Metallurgists, 1979.
93. H.J.Bunge, Z.Metallkde., 56, 872 (1965).
94. R.J.Roe, J.Appl.Phys., 36, 2024, 2069 (1965).
95. H.J.Bunge, Mathematische Methoden der Texturanalyse, Akademie Verlag, Berlin (1969).
96. H.J.Bunge, Texture Analysis in Materials Science, Butterworths, London (1982).
97. K.Lücke, H.J.Perlwitz and W.Pitsch, Phys.Stat.Sol., 7, 737 (1964).
98. J.Hirsch and K.Lücke, Acta Metall., 36, 2863 (1988).
99. G.Dearnaley, J.H.Sreeman, R.S.Nelson and J.Stephen, Ion Implantation, North-Holland Publishing Co., 527 (1973).

100. I.L.Dillamore and H.Katoh, ICOTOM 3, Krakow, 315 (1971).
101. K.Lücke, Proc. sixth Intl.Conf. on Textures of Materials, 1, 14 (1981).
102. R.K.Ray, Acta Metall.Mater. (in press).
103. G.Y.Chin, W.F.Hosford and D.R.Mendorf, Proc.Roy.Soc., A309, 433 (1969).
104. P. vanHoutte, Acta Metall., 26, 591 (1978).
105. G.Wassermann, Z.Metallkde., 54, 61 (1963).
106. I.L.Dillamore and N.S.Stoloff, Textures in research and Practice, eds. J.Grewen and G.Wassermann, Springer-Verlag, 110 (1969).
107. H.Sato and R.S.Toth, Alloying Behaviour and Effects in Concentrated Solid Solution, ed. T.B.Massalski, Gordon and Breach, 295 (1965).
108. H.J.Beattie, Jr., Intermetallic Compounds, ed. J.H.Westbrook, Wiley and Sons Inc., New York, 144 (1967).
109. C.Barrett and T.B.Massalski, Structure of Metals, third revised edition, Pergamon Press, 460 (1980).
110. V.A.Philips and R.B.Jones, Trans. ASM, 53, 775 (1961).
111. M.Y.Huh, J.Hirsch, and K.Lücke, Acta Metall., 34, 1999 (1986).
112. M.Yamaguchi and Y.Umakoshi, Plastic Deformation and Fracture of Solids, eds. R.W.Cahn, P.Hassen and E.J.Kramer, Weinheim, NY; Basel; Cambridge: VCH, 251 (1993).
113. K.H.Virnich, Doctoral Thesis, Institute für Metallkunde, RWTH, Aachen (1979).
114. K.Mitsui, Y.Mishima and T.Suzuki, Phil.Mag., A59, 123 (1989).
115. G.Gulai and E.J.Greenhow, J.Therm.Anal., 6, 279 (1974).
116. A.K.Jena, A.K.Gupta and M.C.Chaturvedi, Acta Metall., 37, 885 (1989).
117. T.Wang, M.Shimotomai and M.Doyama, J.Phys.F, 14, 37 (1984).

A121704

A 121704

Date Slip

This book is to be returned on the
date last stamped.

1

.....

.....

.....

.....

.....

.....

.....

.....

.....

.....

.....

.....

.....

.....

MME- 1995 - D - CHO - STR

A121704